

001  
002  
003  
004  
005  
006  
007  
008  
009  
010  
011  
012  
013  
014  
015  
016  
017  
018  
019  
020  
021  
022  
023  
024  
025  
026  
027  
028  
029  
030  
031  
032  
033  
034  
035  
036  
037  
038  
039  
040  
041  
042  
043  
044  
045  
046

# Microbial symbionts buffer hosts from the demographic costs of environmental stochasticity

Joshua C. Fowler<sup>1,2\*</sup>, Shaun Ziegler<sup>3</sup>, Kenneth D. Whitney<sup>3</sup>,  
Jennifer A. Rudgers<sup>3</sup>, Tom E.X. Miller<sup>1</sup>

<sup>1</sup>\*Department of BioSciences, Rice University, Houston, 77005, TX, USA.

<sup>2</sup>Department of Biology, University of Miami, Miami, 33146, FL, USA.

<sup>3</sup>Department of Biology, University of New Mexico, Albuquerque, 87131, NM, USA.

\*Corresponding author(s). E-mail(s): [jcf221@miami.edu](mailto:jcf221@miami.edu);

Contributing authors: [shaun.ziegler@gmail.com](mailto:shaun.ziegler@gmail.com); [whitneyk@unm.edu](mailto:whitneyk@unm.edu);

[jrudgers@unm.edu](mailto:jrudgers@unm.edu); [tom.miller@rice.edu](mailto:tom.miller@rice.edu);

Phone: 719-359-2960

#### Author Contributions

J.C.F. contributed to data collection, data analysis, and led manuscript drafting. S.Z. contributed to data collection and manuscript revisions. K.D.W. contributed to research conception, data collection, and manuscript revisions. J.A.R. established transplant plots, contributed to research conception, data collection, and manuscript revisions. T.E.X.M. contributed to research conception, data collection, data analysis, and manuscript revisions.

#### Data and Code Accessibility

Data will be made accessible as an Environmental Data Initiative package online  
**DOI:** [updated here when available](#). Code for all analysis is available through  
<https://github.com/joshuacfowler/Grass-Endophyte-Stochastic-Demography>

**Article Type:** Letter

**Running Title:** Symbiont-mediated demographic buffering

**Keywords:** stochastic demography, plant-microbe interactions, environmental variability, symbiosis, mutualism, long-term data, life history, Epichloë, Poaceae

**This file contains:** Abstract ( 150 words), Main Text (5000 words), Figures (1-5); Supporting Information - Supplemental Methods, Supplemental Figures S1-S89, Supplemental Tables S1-S3, References (84)

047  
048  
049  
050  
051  
052  
053  
054  
055  
056  
057  
058  
059  
060  
061  
062  
063  
064  
065  
066  
067  
068  
069  
070  
071  
072  
073  
074  
075  
076  
077  
078  
079  
080  
081  
082  
083  
084  
085  
086  
087  
088  
089  
090  
091  
092

### Abstract

Species' persistence in increasingly variable climates will depend on resilience against the fitness costs of environmental stochasticity. Most organisms host microbiota that shield against stressors. Here, we test the hypothesis that, by limiting exposure to temporally variable stressors, microbial symbionts reduce hosts' demographic variance. We parameterized stochastic population models using data from a 14-year symbiont-removal experiment including seven grass species that host *Epichloë* fungal endophytes. Results provide novel evidence that symbiotic benefits arise not only through improved mean fitness, but also through damped inter-annual variance. Hosts with "fast" life history traits benefited most from symbiont-mediated demographic buffering. Under current climate conditions, contributions of demographic buffering were modest compared to benefits to mean fitness. However, simulations of increased stochasticity amplified benefits of demographic buffering and made it the more important pathway of host-symbiont mutualism. Microbial-mediated variance buffering is likely an important, yet cryptic, mechanism of resilience in an increasingly variable world.

	093
	094
	095
	096
	097
	098
	099
	100
	101
	102
	103
	104
	105
	106
	107
	108
	109
	110
	111
	112
	113
	114
	115
	116
	117
	118
	119
	120
	121
	122
	123
	124
	125
	126
	127
	128
	129
	130
	131
	132
	133
	134
	135
	136
	137
	138

## Introduction

Global climate change involves heterogenous changes in environmental variability, including an increasing frequency of extreme weather events and of “whiplash events” that alternate between climate extremes (Seneviratne et al, 2012; Bathiany et al, 2018; Swain et al, 2018; IPCC, 2021). Yet, the ecological consequences of changing variability are less well understood than those of changing means, such as long-term warming or drying. Incorporating realistic variability into forecasts of population dynamics can improve predictive ability (Clark, 2005).

Classic theory predicts that long-term population growth rates (equivalently, population mean fitness) will decline under increased environmental stochasticity because costs of bad years outweigh benefits of good years – a consequence of nonlinear averaging (Lewontin and Cohen, 1969; Tuljapurkar, 1982). For example, in unstructured populations, the long-term stochastic growth rate in a fluctuating environment ( $\lambda_S$ ) will always be lower than the arithmetic mean of annual growth rates ( $\bar{\lambda}_t$ ) by an amount proportional to the environmental variance ( $\sigma^2$ ):

$$\log(\lambda_S) \approx \log(\bar{\lambda}_t) - \frac{\sigma^2}{2\bar{\lambda}_t} \quad (1)$$

Populations structured by size or stage experience similar costs of temporal variability (Cohen, 1979; Tuljapurkar, 2013). There are accordingly two pathways to increase population viability in variable environments: increase the arithmetic mean growth rate and/or dampen temporal fluctuation in growth rates, also called “demographic buffering”.

Both inherent characteristics of species and their environments can buffer demographic fluctuations. Inherent characteristics include life history traits (Pfister, 1998), trade-offs among vital rates (Compagnoni et al, 2016), and transient shifts in population structure (Ellis and Crone, 2013). For example, theory predicts long-lived species, those on the slow end of the slow-fast life history continuum, to be less sensitive to environmental variability than short-lived species (Murphy, 1968), a pattern with empirical support across plants (Davison et al, 2019; Compagnoni et al, 2021) and animals (Le Coeur et al, 2022; Morris et al, 2008). Demographic variance is also determined by external abiotic factors, such as the magnitude of environmental variability (Rodríguez-Caro et al, 2021) or environmental autocorrelation (Tuljapurkar and Orzack, 1980; Fieberg and Ellner, 2001). The complex interplay of these factors determines populations’ risk of extinction (Menges, 2000) and underlies management strategies promoting ecosystem resilience (Kuparinen et al, 2016). Yet, little is known about how inter-specific interactions contribute to demographic buffering (Hilde et al, 2020).

Most multicellular organisms host symbiotic microbes that affect growth and performance (Rodriguez et al, 2009; McFall-Ngai et al, 2013), many of which are vertically transmitted from maternal hosts to offspring (Funkhouser and Bordenstein, 2013).

139 Vertical transmission links the fitness of hosts and symbionts in a feedback loop that  
140 selects for mutual benefits (Fine, 1975). These mutualistic microbes can protect hosts  
141 from stressful environmental conditions including drought, extreme temperatures, or  
142 natural enemies (Russell and Moran, 2006; Kivlin et al, 2013). Some well studied  
143 examples include bacterial symbionts of insects that provide hosts with thermal toler-  
144 ance through the production of heat-shock proteins (Dunbar et al, 2007), and fungal  
145 symbionts of plants that produce anti-herbivore and drought-protective compounds  
146 (Reyna et al, 2012; Saikonen et al, 2013; Neyaz et al, 2022). However, these diverse  
147 protective symbioses are context-dependent: the magnitude of benefits depends on  
148 environmental conditions (Chamberlain et al, 2014; Catford et al, 2022) and thus  
149 will vary temporally in stochastic environments (Jordano, 1994). We hypothesized  
150 that context-dependent benefits from symbionts may buffer host populations against  
151 variability through strong benefits during harsh periods and neutral or even costly  
152 outcomes during benign periods, reducing the impacts of host exposure to extremes  
153 and dampening inter-annual variance relative to non-symbiotic hosts (Fig. 1A). Vari-  
154 ance buffering is a previously unexplored mechanism by which symbionts may benefit  
155 their hosts instead of or in addition to elevating average fitness (Fig. 1C), the focus  
156 of most previous research.

157 To test the hypothesis that context-dependent benefits of symbiosis dampen inter-  
158 annual variance in host fitness, we used a combination of long-term field experiments  
159 and stochastic demographic modeling. We used cool-season grasses and *Epichloë* fun-  
160 gal endophytes, a tractable experimental model in which non-symbiotic plants can be  
161 derived from naturally symbiotic plants through heat treatment, providing a contrast  
162 of symbiont effects that controls for the confounding influence of host genetic back-  
163 ground. *Epichloë* endophytes are specialized symbionts growing intercellularly in the  
164 aboveground tissue of ~ 30% of *C<sub>3</sub>* grass species (Leuchtmann, 1992). These fungi are  
165 primarily transmitted vertically from maternal plants through seeds (Cheplick et al,  
166 2009). They produce a variety of alkaloids that can protect host plants from natural  
167 enemies (Brem and Leuchtmann, 2001) and drought stress (Decunta et al, 2021).

168 Over 14 years (2007–2021), we collected longitudinal demographic data on the  
169 survival, growth, reproduction, and recruitment of all plants within replicated  
170 endophyte-symbiotic and endophyte-free populations at our field site in southern Indi-  
171 ana, USA. Through taxonomic replication (seven host-symbiont species pairs) we  
172 aimed to understand whether host life history traits could explain inter-specific vari-  
173 ation in the magnitude of demographic buffering through symbiosis. We used this  
174 long-term data to parameterize Bayesian stochastic population projection models.  
175 Specifically, we (1) quantified the effect of symbiosis on the mean and variance of host  
176 vital rates (survival, growth and reproduction) and fitness, (2) evaluated the relation-  
177 ship between host life history traits and the magnitude of symbiont-mediated variance  
178 buffering, (3) determined the relative contributions of symbiont-mediated mean and  
179 variance effects to host fitness, and (4) projected how increased environmental stochas-  
180 ticity (expected under future climates) changes the importance of variance buffering  
181 as a pathway of host-symbiont mutualism.

182  
183  
184

<b>Materials and Methods</b>	185
<b>Study site and species</b>	186
This study was conducted at Indiana University's Lilly-Dickey Woods Research and Teaching Preserve (39.238533, -86.218150) in Brown County, Indiana, USA. This site is part of the Eastern broadleaf forests of southern Indiana, where the ranges of many understory cool-season grass species overlap. We focused on seven of these grasses ( <i>Agrostis perennans</i> , <i>Elymus villosus</i> , <i>Elymus virginicus</i> , <i>Festuca subverticillata</i> , <i>Lolium arundinaceum</i> , <i>Poa alsodes</i> , and <i>Poa sylvestris</i> ), each of which hosts a unique species of <i>Epichloë</i> endophyte (Table S1). All are native to eastern North America except the Eurasian species <i>L. arundinaceum</i> .	187
Seeds from local, naturally symbiotic populations of the seven focal host species were collected during summer-fall 2006. Seeds were disinfected with a heat treatment or left untreated to generate symbiont-free (S-) and symbiotic (S+) plants from the same genetic lineages. In fall of 2007 and spring of 2008, we established 10 3x3 m plots for <i>A. perennans</i> , <i>E. villosus</i> , <i>E. virginicus</i> , <i>F. subverticillata</i> , and <i>L. arundinaceum</i> and 18 plots for <i>P. alsodes</i> and <i>P. sylvestris</i> . Each plot was randomly assigned to be planted with 20 evenly spaced symbiotic (S+) or symbiont-free (S-) plants. Full details of endophyte removal, plant propagation and field set-up are provided in <i>Supporting Information - Supplemental Methods and Table S1</i> .	188
Long-term demographic data collection	197
Each summer (2008–2021) we censused all individuals in each plot for survival, growth and reproduction. Plots contained 13.3 individuals/m <sup>2</sup> on average during the study. Each census year was a sample of inter-annual variation (n = 14 years, comprising 13 demographic transition years). We censused each species during its peak fruiting stage (May: <i>Poa alsodes</i> , <i>Poa sylvestris</i> ; June: <i>Festuca subverticillata</i> ; July: <i>Elymus villosus</i> , <i>Elymus virginicus</i> , <i>Lolium arundinaceum</i> ; September: <i>Agrostis perennans</i> ), such that censuses were pre-breeding and new recruits came from the previous years' seed production (Fig. S1 shows a generalized life cycle diagram). Leaf litter was cleared out of each plot before the census, to aid in locating plants. For each tagged plant, we determined survival, measured size as a count of tillers, and collected reproductive data as counts of reproductive tillers and seed-bearing spikelets on up to three reproductive tillers. We also tagged all unmarked recruits from the previous years' seed production and collected the same demographic data. New recruits typically had one tiller and were non-reproductive. In 2008 through 2010, we took counts of seeds per inflorescence for all reproducing individuals in the plots to relate inflorescence and spikelet counts to seed production. In 2018, we stopped collecting data for <i>L. arundinaceum</i> , which had very high survival and low recruitment, and consequently low variation in population size across years. In total, the dataset included demographic information for 16,789 individual host-plants and 31,216 transition-year observations.	198
	199
	200
	201
	202
	203
	204
	205
	206
	207
	208
	209
	210
	211
	212
	213
	214
	215
	216
	217
	218
	219
	220
	221
	222
	223
	224
	225
	226
	227
	228
	229
	230

231 **Vital rate modeling**

232 Equipped with demographic data, we fit statistical models for adult survival, seedling  
233 survival, adult growth, seedling growth, reproductive status (flowering or vegetative),  
234 fertility of flowering plants (number of inflorescences), production of seed-bearing  
235 spikelets (number per inflorescence), the average number of seeds per spikelet, and  
236 the recruitment of seedlings from the preceding year's seed production. We fit vital  
237 rates as generalized linear mixed models in a hierarchical Bayesian framework using  
238 RStan ([Stan Development Team, 2022](#)) which allowed us to isolate endophyte effects  
239 on vital rate means and variances, borrow strength across species for some variance  
240 components, and propagate uncertainty from individual-level vital rates to popula-  
241 tion projection models ([Elderd and Miller, 2016](#)). All size-structured models included  
242 the same linear predictor, including two key parameters for each species: one which  
243 described the effect of endophyte symbiosis on the mean of that vital rate, and another  
244 which described inter-annual variance in the vital rate for symbiotic and symbiont-  
245 free plants, estimated using random year effects specific to each species and endophyte  
246 status. This species- and endophyte status- specific random year effect allowed us  
247 to quantify effects of endophytes on inter-annual variance for each vital rate. Other  
248 parameters accounted for size structure in the data (defined as the number of tillers)  
249 as well as differences between originally transplanted plants (started in a greenhouse)  
250 and those which recruited naturally into the plots. Each vital rate model included  
251 a random effect for plot variance shared across species. Full statistical analyses are  
252 detailed in *Supporting Information - Supplemental Methods*.  
253

254 **Stochastic population model**

255 We built stochastic matrix projection model for each host species. We parameter-  
256 ized the models using the fitted statistical vital rate models in a manner similar to  
257 continuous IPM models ([Ellner et al, 2016](#)), while accounting for the discrete data rep-  
258 resenting our focal species' growth ([Ellner et al, 2022](#)) Each matrix projection model  
259 included two state variables:  $r_t$  (the number of newly recruited individuals in year  $t$   
260 which we assume to be non-reproductive), and  $\mathbf{n}_t$  (a vector including all non-seedling  
261 individuals of discrete sizes  $x \in \{1, 2, \dots, U\}$  ranging from one to the maximum number  
262 of tillers  $U$ ). We use these two state variables to avoid assuming demographic equiv-  
263 alence between seedling and non-seedling one-tiller plants. We used the same model  
264 structure, corresponding to a pre-breeding census, for each species and endophyte  
265 status (not shown in model notation for readability; Fig. S1).

266 The number of recruits in year  $t + 1$  is given by:

$$267 \quad r_{t+1} = \sum_{x=1}^U P(x; \boldsymbol{\tau}_P) F(x; \boldsymbol{\tau}_F) K(x; \boldsymbol{\tau}_K) D R(\boldsymbol{\tau}_R) n_t^x \quad (2)$$

268 The total number of seeds produced by a maternal plant of size  $x$  is the product of  
269 the size-specific probability of flowering  $P$ , the number of inflorescences conditional  
270 on flowering  $F$ , the number of spikelets per inflorescence  $K$ , and the number of seeds  
271 per spikelet  $D$ . Multiplying by the probability of transitioning from seed to seedling  
272  $R$  gives a per-capita seedling production rate, which is multiplied by the number of  
273

plants of size  $x$  ( $n_t^x$ , the  $x^{\text{th}}$  element of  $n_t$ ) and summed over all sizes. Each function also depends on species- and endophyte-specific year random effects for that vital rate ( $\boldsymbol{\tau}$ , a vector of year-specific values). 277  
278  
279

The number of  $y$ -sized plants in year  $t + 1$  is given by: 280  
281

$$n_{t+1}^y = Z(y; \boldsymbol{\tau}_Z)B(\boldsymbol{\tau}_B)r_t + \sum_{x=1}^U S(x; \boldsymbol{\tau}_S)G(x, y; \boldsymbol{\tau}_G)n_t^x \quad (3)$$

where  $n_{t+1}^y$  is the  $y^{\text{th}}$  element of vector  $\mathbf{n}_{t+1}$ . The first term on the right hand side of Eqn. 3 represents growth ( $Z$ ) and survival ( $B$ ) of seedling recruits. The second term includes survival of previously  $x$ -sized plants and the growth of survivors from size  $x$  to  $y$ , summed over all  $x$ . To avoid predictions of unrealistic growth outside of the observed size distribution, we capped the growth function for plants at the 97.5<sup>th</sup> percentile of observed sizes for each host species (Williams et al., 2012). We analyzed projection models constructed from parameters representing the dynamics of naturally recruited plants. 282  
283  
284  
285  
286  
287  
288  
289  
290  
291  
292  
293  
294  
295  
296  
297  
298  
299  
300  
301  
302  
303  
304  
305  
306  
307  
308  
309  
310  
311  
312  
313  
314  
315  
316  
317  
318  
319  
320  
321  
322

Each vital rate function in Eqns. 2 and 3 has separate intercepts and year random effects for symbiotic and symbiont-free populations, allowing us to calculate the effect of endophyte symbiosis on the mean, variance, and coefficient of variation (CV) of  $\lambda_t$ , the dominant eigenvalue of the year- and endophyte-specific projection matrix. This model treats climate drivers implicitly through year-specific random effects. We also developed a climate-explicit version with additional parameters defining the relationship between either annual or growing season drought index and each vital rate (Supporting Information - Supplemental Methods).

To calculate stochastic population growth rates ( $\lambda_S$ ) for each host species and endophyte status we simulated population dynamics for 1000 years by randomly sampling from the 13 annual transition matrices, discarding the first 100 years to minimize the influence of initial conditions. Sampling observed transition matrices (rather than independently sampling regression coefficients) produces models that realistically capture inter-annual variation by preserving vital rate correlations (Metcalf et al., 2015). We tallied total population size at each time step as  $N_t = r_t + \sum_{x=1}^U n_t^x$  and calculated the stochastic growth rate as  $\log(\lambda_S) = E[\log(\frac{N_t}{N_{t+1}})]$  (Caswell, 2001; Rees and Ellner, 2009). We calculated total effects of endophyte symbiosis as the difference in  $\lambda_S$  between S+ and S- populations. We propagated uncertainty from the vital rates to the calculation of  $\lambda_S$  using 500 draws from model posteriors.

## Life History Analysis

We collected metrics describing each host species' life history to test the relationship between pace of life and variance buffering (Table S2). We recorded seed size as the average lemma length from the Flora of North America (of North America Editorial Committee, 1993). We calculated the 99th percentile of maximum observed age for symbiont-free plants from the census data for each species. Using the Rage package (Jones et al., 2022), we calculated generation time, longevity, net reproductive rate  $R_0$ , Keyfitz entropy (describing survivorship across lifespan), and Demetrius

323 entropy (describing reproduction across lifespan) from the mean transition matrix for  
324 symbiont-free populations. Next, we fit Bayesian phylogenetic mixed-effects models  
325 using the brms package (Bürkner, 2017) to test the relationship between each life his-  
326 tory trait and the effect of symbiosis on the CV of  $\lambda_t$  (a measure of variance buffering)  
327 while controlling for phylogenetic non-independence. We pruned species-level phylo-  
328 genies of plants (Zanne et al, 2014) and *Epichloë* fungi (Leuchtmann et al, 2014) to  
329 include the focal species (or a congener for one host), and defined separate phylo-  
330 genetic covariance matrices from these pruned trees for host and symbiont species. We  
331 propagated uncertainty in the estimated variance buffering effect with a measurement  
332 error model, described in full in the *Supporting Information - Supplemental Methods*.  
333

### 334 Mean-variance decomposition

335 We decomposed total endophyte effects on  $\lambda_S$  into contributions from effects on vital  
336 rate means, and variances. Specifically, we repeated the calculation of S+ and S-  $\lambda_S$   
337 described above for two additional “treatments”: (1) endophyte effects on mean vital  
338 rates only, with inter-annual variances shared between S+ and S- at the S- reference  
339 level for all vital rates, and (2) endophyte effects on vital rate variances only, with  
340 vital rate means shared between S+ and S- at the S- reference level. The combination  
341 of all four  $\lambda_S$  treatments (S+ vital rate means and variances, S- means and variances,  
342 S+ means with S- variances, S- means with S+ variances) allowed us to quantify  
343 the extent that overall effects of symbiosis derive from changes in vital rates means,  
344 variances, and their interaction. The interaction occurs because the variance penalty  
345 to stochastic growth is proportional to the arithmetic mean of annual growth rates  
346 (as in Eq. 1, for example) such that variance is more detrimental for populations with  
347 lower average growth rates. To quantify how mean and variance effects of symbionts  
348 arise through effects on different vital rates, we performed an additional decomposition  
349 described in *Supporting Information Supplemental Methods* that isolates symbiont  
350 effects on growth and survival from effects on fertility and recruitment.  
351

352 We simulated scenarios of increased variance relative to that observed during our  
353 study by sampling subsets of the 13 observed annual transition matrices. We created  
354 two scenarios of increased environmental variance by sampling the transition matrices  
355 associated with the set of either six or two most extreme  $\lambda_t$  values for S- populations.  
356 These extreme  $\lambda_t$  values represent the best and worst years experienced by symbiont-  
357 free populations. By sampling away from an average year in both directions, the six-  
358 and two- years scenarios increased standard deviation of annual host growth rates by  
359 1.3 and 2.1 times, respectively, without changing mean growth rates (< 2.1% difference  
360 in  $\bar{\lambda}_t$  between simulation treatments, Fig. S80). We performed the same mean-variance  
361 decomposition for these scenarios as described above.

362  
363  
364  
365  
366  
367  
368

<b>Results</b>	369
<b>Symbionts buffer host demographic variance</b>	370
Across 14 census years, endophytes reduced inter-annual variance for 66% (37/56) of host species-vital rate combinations (average Cohen's D for effects on vital rate standard deviation: -0.15) (Fig. 2A; Figs. S22 - S29). Endophytes also increased mean vital rates for the majority (36/56) of host species-vital rate combinations (average Cohen's D for effects on vital rate mean: 0.15), and benefits were particularly strong for host survival, plant growth and recruitment (Fig. 2A; Fig. S2 - S11). The magnitude of mean and variance effects differed among hosts and vital rates. Symbiont effects on vital rate variance were as large and even exceeded mean effects for certain species. For example, endophytes modestly increased mean adult survival (Fig. 2C) and strongly reduced variance in survival (Fig. 2D) for <i>Festuca subverticillata</i> , while for <i>Poa alsodes</i> , variance buffering was more apparent in seedling growth and inflorescence production (Fig. 2E). Additionally, some vital rates showed costs of symbiosis. Symbiotic individuals of <i>A. perennans</i> grew larger than symbiont-free hosts (Fig. 2B), yet endophytes also reduced this species' mean recruitment (Fig. 2A). Similarly, endophytes increased variance for certain species' vital rates, including seedling growth for <i>Elymus villosus</i> and <i>Festuca subverticillata</i> (Fig. 2A).	371
Because not all vital rates contribute equally to fitness, we used stochastic matrix models to integrate diverse vital rate effects described above into comprehensive measures for the arithmetic mean and variance of year-to-year fitness ( $\lambda_t$ ). On average across host species, mean fitness of S+ populations increased by more than 10% (> 92% confidence that endophytes increased $\lambda_t$ ) and inter-annual variability in fitness was 26% lower (> 86% confidence that endophytes decreased the coefficient of variation of $\lambda_t$ ) than S- populations (Fig. 3). For some host species, the CV of $\lambda_t$ declined by more than 62% ( <i>P. alsodes</i> , <i>F. subverticillata</i> ), while for others, endophyte effects on variance were substantially smaller (5% lower for <i>E. villosus</i> , 13% lower for <i>A. perennans</i> ), or even positive (37% increase for <i>E. virginicus</i> ). Considering mean and variance effects together, none of the host-symbiont pairings were antagonistic (i.e., with endophytes that both decreased mean fitness and increased variance) (Fig. 3C)	372
<b>Faster life histories predict stronger symbiont-mediated variance buffering</b>	373
Hosts with slow life history trait values experienced weaker variance buffering from endophytes than those with fast life histories (Fig. 4). Variance buffering was stronger for host species with shorter lifespan (Fig. 4A; 67% probability of positive relationship with empirically observed maximum plant age) and smaller seeds (Fig. 4B; 65% probability of positive relationship with seed length). Other life history traits similarly had weak, positive support for the prediction that faster life history traits correlate with stronger variance buffering (Fig. S83-S85). Models indicate moderate phylogenetic signal in the effect of variance buffering (average Pagel's $\lambda$ of 0.22 (90% CI: 0-0.8) and of 0.56 (90% CI: 0-0.9) from models including host and symbiont phylogeny respectively (Table S2)).	374
	375
	376
	377
	378
	379
	380
	381
	382
	383
	384
	385
	386
	387
	388
	389
	390
	391
	392
	393
	394
	395
	396
	397
	398
	399
	400
	401
	402
	403
	404
	405
	406
	407
	408
	409
	410
	411
	412
	413
	414

415 **Contributions from variance buffering are weak relative to  
416 mean effects**

417 To evaluate the relative importance of mean fitness benefits and variance buffering as  
418 alternative pathways of mutualism, we decomposed the overall effect of the symbiosis  
419 on stochastic growth rates  $\lambda_S$  using simulations including either the full symbiosis  
420 effect (both mean and variance effects), mean effects alone, variance effects alone, or  
421 neither mean nor variance effects. Overall, the full effect of symbiosis on  $\lambda_S$ , averaged  
422 across host species, provided strong evidence of grass-endophyte mutualism (99% cer-  
423 tainty of a positive total effect on  $\lambda_S$ ) (Fig. 5; see Fig. S81 for individual host species).  
424 Contributions to this full effect derived from both mean and variance buffering effects,  
425 as well as a slightly negative interaction (i.e., the combined influence of mean and  
426 variance effects was smaller than the sum of their individual effects). Endophytes' con-  
427 tributions to  $\lambda_S$  from mean effects were four times greater, averaged across species,  
428 than contributions from variance buffering (Fig. 5), suggesting that, under the regime  
429 of environmental variability represented by our 14-year study, damped fluctuations  
430 in fitness via variance buffering was a less important element of symbiont benefits than  
431 increased mean fitness. Decomposing this result further into contributions through  
432 different vital rates demonstrated that demographic buffering arose primarily from  
433 symbionts' effects on host survival and growth, rather than from effects on repro-  
434 duction (Fig. S82). Results for individual host species were largely consistent with  
435 cross-species trends (Fig. S81). The full effect of symbiosis on  $\lambda_S$  was positive for  
436 five out of seven host species, with statistical confidence ranging from 78% to > 99%  
437 certainty. The exceptions were *P. sylvestris* and *A. perennans*, for which our analy-  
438 sis indicated effectively neutral symbionts in their overall fitness effect (42% and 57%  
439 posterior probability of positive effects respectively; Fig. S81).

441  
442 **Variance buffering strengthens under increased environmental  
443 variability**

444 To simulate increased variability, we repeated the decomposition of  $\lambda_S$  for two alterna-  
445 tive scenarios, randomly sampling transition matrices that represented either the six or  
446 two most extreme years, subsets of the thirteen transition matrices across the 14-year  
447 study period. Increased variability elicited stronger mutualistic benefits of endophyte  
448 symbiosis than ambient variability (Fig. 5; overall effect of the symbiosis increased by  
449 ~2fold). This increase was driven by increased contributions from variance buffering  
450 (from a 16% contribution in the ambient scenario to a 54% contribution in the most  
451 variable scenario) rather than from greater mean effects. In the most variable scenario,  
452 the relative importance of mean and variance effects reversed, with variance buffering  
453 contributions that were 1.2 times greater than mean contributions, averaged across  
454 species (Fig. 5).

456  
457 **Discussion**

458 Across seven host species, eight vital rates, 14 years, and 16,789 individuals, our anal-  
459 ysis provided the first empirical evidence, to our knowledge, of demographic buffering  
460

conferred by microbial symbionts. Our taxonomically-replicated, long-term field experiments that manipulated the presence/absence of fungal symbionts in plants revealed that heritable microbes can commonly benefit hosts not only through improved mean fitness – the focus of most previous research – but also through buffering against environmental variance (Fig. 1). Benefits to mean fitness dominated the overall fitness advantage of endophyte symbiosis under observed environmental variability. However, the strongest symbiotic benefits derived from the combination of both mean effects and variance buffering (Fig. 1B), and simulation experiments point to an increasing role for demographic buffering under increased temporal environmental stochasticity (Fig. 5; Figs. S81-S82). There is growing interest in demographic buffering as a potential source of resilience against increased stochasticity under global change (Hilde et al, 2020). Our results suggest that biotic interactions, and microbial mutualisms in particular, may be an under-appreciated mechanism of demographic buffering. In fact, any interaction that is subject to context-dependence – where magnitudes of cost or benefit depends on harshness of the environment – holds potential to modify demographic variance across years. However, long-term experimental data required to detect such an influence are rarely available.

Taxonomic replication of host-symbiont pairs enabled us to generalize beyond the focal taxa and facilitated inference about the *types* of species in which demographic buffering may be more or less likely. Because host taxa with “slow” life history traits, such as long lifespan, may be intrinsically buffered from environmental variability (Rees, 1996; Moles and Westoby, 2004; Morris et al, 2008), we predicted that buffering effects of endophyte symbiosis would be stronger in hosts with faster pace of life. Supporting this prediction, we found that shorter-lived and smaller-seeded host species experienced stronger reductions in demographic variance through endophyte symbiosis. Thus, microbial symbiosis may compensate for the lack of intrinsic tolerance of variability conferred by slow life history traits. Future studies may consider fungal life history traits, such as diversity in biologically-active alkaloids, or the production of stromata - fruiting bodies capable of horizontal (contagious) transmission. The host species for which the net mutualism benefit was greatest (*F. subverticillata* and *L. arundinaceum*) (Fig. S79) were among those never observed to produce fungal stromata (Table S2), supporting theoretical expectations that strict vertical transmission drives evolution of strong host-symbiont mutualism (Fine, 1975; Afkhami and Rudgers, 2008). We caution that inferences on trait correlates of demographic buffering were subject to large uncertainties (Fig. S85), reflecting relatively narrow taxonomic breadth (closely related grass species in the sub-family Pooideae and their co-evolving symbionts). Understanding of how life history variation modulates fitness consequences of microbial symbiosis would profit from tests across a wider span of plant and animal groups (Jeschke and Kokko, 2009). We also found relatively consistent, positive effects of endophyte symbiosis on stochastic fitness (Fig. S78-S79), suggesting that variation across host species and vital rates in mean and variance effects (Fig. 3C) may reflect alternative strategies that yield similar net benefits.

While our results highlight symbiont-mediated demographic buffering as a potential source of resilience against increased environmental stochasticity, much work remains to connect symbiont effects on mean and variance to quantitative forecasts of

host-symbiont dynamics under global change. Like most temporally stochastic population projection models, our approach quantified demographic variance across years (and simulated increasing variance) without attributing its cause(s). Realistic forecasts for host-symbiont dynamics under environmental change will require explicit connections between driver variables and demographic responses. Reduced sensitivity to drought, as is common in *Epichloë* symbioses (Reyna et al, 2012; Saikkonen et al, 2013; Neyaz et al, 2022; Decunta et al, 2021), is a candidate mechanism that could generate a signature of variance buffering: drought conditions may be less costly for S+ hosts, dampening the effects of drought years and reducing fluctuations in fitness through time (Fig. 1). Preliminary climate-explicit analyses indicated that symbionts reduced sensitivity to drought indices for five of seven host taxa (Supporting Information; Fig. S88-S89; Table S3). However, we did not find a strong relationship between magnitude of variance buffering and relative drought sensitivities, suggesting that other climatic factors or temporally-varying aspects of the environment may elicit benefits of symbiosis, including documented resistance to herbivory for six of these host taxa (Rudgers and Clay, 2008; Crawford et al, 2010). Identifying the type and timescale of relevant drivers would allow more direct connections between demographic models and outputs from global climate models.

Symbiont-mediated demographic buffering is a potential target of selection for improved holobiont fitness (Vandenkoornhuyse et al, 2015) and carries implications for the evolution of bet-hedging strategies in variable environments. Demographic buffering may be considered a bet-hedging strategy if reduced temporal variance comes at the cost of arithmetic mean fitness (Childs et al, 2010). This may be unlikely in this system, where most host species exhibited both reduced variance and elevated mean fitness through symbiosis (Fig. 3C). However, the context-dependent fitness effects that underlie demographic buffering may favor other forms of evolutionary bet-hedging. Theory suggests that imperfect transmission (the production of S- offspring from S+ parent) may be an adaptive host strategy in spatially or temporally varying environments when fitness effects of symbionts are environment-dependent by extending phenotypic variance of offspring and improving the odds of some having the optimal symbiont status for their environment (Brown and Akçay, 2019; Bruijning et al, 2022; Lange et al, 2023). Imperfect vertical transmission is well-documented in grass-endophyte symbioses (Afkhami and Rudgers, 2008), including our focal taxa (Table S2), and could be incorporated into our model by dynamically linking S+ and S- populations (Yule et al, 2013; Chung et al, 2015). A further step could incorporate diverse symbiont partners (e.g. different strains of *Epichloë* fungi or multiple species within the microbiome) to understand how microbial diversity contributes to host genotypic and phenotypic variance (Henry et al, 2021).

Several limiting features of our study point to new directions and valuable next steps. We focused explicitly on temporal variation and intentionally averaged over spatial heterogeneity. Endophytes may dampen spatial heterogeneity in host fitness in ways that parallel their effects on temporal variance, and this hypothesis could be explored by leveraging the plot replication in our experiment. At larger spatial scales, buffering effects of symbionts may vary across the broad geographic distributions

of these eastern North American grass species, especially since historical and projected trends in climate variability are geographically heterogeneous (Bathiany et al, 2018). Finally, our demographic modeling framework could be further “unpacked” to explore other elements of fitness in stochastic environments. We identified damping variance in survival and growth as the key avenue by which symbionts’ variance effects contributed to host fitness (Fig. S82). Elasticity analyses could explore the selection that drives diverse symbiont effects across host vital rates. Small changes in variance of vital rates that are highly important to population growth (i.e. those with high elasticities) may be more strongly selected for than larger changes in less important vital rates (Doak et al, 2005), and symbionts may even provide an adaptive advantage by increasing temporal variance in certain vital rates (i.e. demographic lability) (Koops et al, 2009). Further, our simulations assumed an independently distributed environmental distribution through time, but environmental auto-correlation can be an important component of stochastic population projections (Tuljapurkar and Haridas, 2006) and might modify the fitness consequences of symbiont-mediated variance buffering. Similarly, correlated responses of multiple vital rates could amplify or dampen demographic variance (Tuljapurkar, 2013; Davison et al, 2013; Compagnoni et al, 2016). Our “matrix sampling” approach accounted for vital rate correlations implicitly (Metcalf et al, 2015) but exploring whether and how endophyte symbiosis alters the correlation structure of host vital rates could add nuance to understanding of symbionts’ contributions to variance buffering.

**Conclusion**

Ecologists increasingly recognize the importance of symbiotic microbes for host organisms and the populations, communities, and ecosystems in which their hosts reside (Afkhami and Strauss, 2016; Smith et al, 2017; Dallas and Warne, 2022; Wu et al, 2022). Despite awareness of these ubiquitous interactions, long-term studies of microbial symbiosis are rare. Our results provide an important advance to improve forecasts of the responses of populations (and symbionts) to increasing environmental stochasticity under global change. We found that, relative to mean fitness benefits, symbiont-mediated variance buffering made weak contributions to host-symbiont mutualism under observed environmental variability. However, demographic buffering is likely to become the dominant benefit that fungal endophytes confer to grass hosts in more variable future environments. Thus, demographic buffering – a cryptic microbial influence that manifests only over long time scales – is poised to become the dominant benefit of symbiosis. This result emerges from the context-dependent nature of grass-endophyte interactions, combined with the observation that environmental stochasticity generates fluctuation in context. These key ingredients, and thus the potential for symbiont-mediated variance buffering, similarly apply to the diverse host-microbe symbioses across the tree of life.

599 **Acknowledgments** We thank Mark Sheehan, Ali Campbell, Kyle Dickens, Blaise  
600 Willis, and Sar Lindner for contributions to field data collection. We also thank Volker  
601 Rudolf, Daniel Kowal, Lydia Beaudrot and Judie Bronstein for helpful comments on  
602 and discussion of this project. This research was supported by the National Science  
603 Foundation (grants 1754468 and 2208857).

604 **Supplementary information** Supplementary information for this paper includes  
605 Supplementary Methods, Figs. S1 to S89, and Tables S1 to S3.  
606

607 **References**  
608

- 609 Afkhami ME, Rutgers JA (2008) Symbiosis lost: imperfect vertical transmission of  
610 fungal endophytes in grasses. *The American Naturalist* 172(3):405–416  
611
- 612 Afkhami ME, Strauss SY (2016) Native fungal endophytes suppress an exotic dom-  
613 inant and increase plant diversity over small and large spatial scales. *Ecology*  
614 97(5):1159–1169  
615
- 616 Bacon CW, White JF (2018) Stains, media, and procedures for analyzing endophytes  
617 pp 47–56  
618
- 619 Bathiany S, Dakos V, Scheffer M, et al (2018) Climate models predict increasing  
620 temperature variability in poor countries. *Science advances* 4(5):eaar5809  
621
- 622 Beguería S, Vicente-Serrano SM (2013) Spei: calculation of the standardised  
623 precipitation-evapotranspiration index. R package version 1(6)  
624
- 625 Brem D, Leuchtmann A (2001) Epichloë grass endophytes increase herbivore resistance  
626 in the woodland grass *brachypodium sylvaticum*. *Oecologia* 126(4):522–530  
627
- 628 Brooks SP, Gelman A (1998) General methods for monitoring convergence of iterative  
629 simulations. *Journal of computational and graphical statistics* 7(4):434–455  
630
- 631 Brown A, Akçay E (2019) Evolution of transmission mode in conditional mutualisms  
632 with spatial variation in symbiont quality. *Evolution* 73(2):128–144  
633
- 634 Bruijning M, Henry LP, Forsberg SK, et al (2022) Natural selection for impre-  
635 cise vertical transmission in host–microbiota systems. *Nature ecology & evolution*  
636 6(1):77–87
- 637 Bultman TL, White Jr JF, Bowdish TI, et al (1995) Mutualistic transfer of epichloë  
638 spermatia by phorbia flies. *Mycologia* 87(2):182–189  
639
- 640 Bürkner PC (2017) brms: An R package for Bayesian multilevel models using Stan.  
641 *Journal of Statistical Software* 80(1):1–28. <https://doi.org/10.18637/jss.v080.i01>  
642
- 643 Caswell H (2001) Matrix population models: Construction, analysis, and interpreta-  
644 tion. 2nd edn sinauer associates. Inc, Sunderland, MA

Catford JA, Wilson JR, Pyšek P, et al (2022) Addressing context dependence in ecology. <i>Trends in Ecology &amp; Evolution</i> 37(2):158–170	645 646 647
Chamberlain S, Hocking D, Anderson B (2022) Package ‘rnoaa’	648
Chamberlain SA, Bronstein JL, Rudgers JA (2014) How context dependent are species interactions? <i>Ecology letters</i> 17(7):881–890	649 650 651
Cheplick GP, Faeth S, Faeth SH (2009) Ecology and evolution of the grass-endophyte symbiosis. OUP USA	652 653 654
Childs DZ, Metcalf C, Rees M (2010) Evolutionary bet-hedging in the real world: empirical evidence and challenges revealed by plants. <i>Proceedings of the Royal Society B: Biological Sciences</i> 277(1697):3055–3064	655 656 657 658
Chung YA, Miller TE, Rudgers JA (2015) Fungal symbionts maintain a rare plant population but demographic advantage drives the dominance of a common host. <i>Journal of Ecology</i> 103(4):967–977	659 660 661 662
Clark JS (2005) Why environmental scientists are becoming bayesians. <i>Ecology letters</i> 8(1):2–14	663 664 665
Cohen JE (1979) Comparative statics and stochastic dynamics of age-structured populations. <i>Theoretical population biology</i> 16(2):159–171	666 667 668
Compagnoni A, Bibian AJ, Ochocki BM, et al (2016) The effect of demographic correlations on the stochastic population dynamics of perennial plants. <i>Ecological Monographs</i> 86(4):480–494	669 670 671
Compagnoni A, Levin S, Childs DZ, et al (2021) Herbaceous perennial plants with short generation time have stronger responses to climate anomalies than those with longer generation time. <i>Nature communications</i> 12(1):1–8	672 673 674 675
Crawford KM, Land JM, Rudgers JA (2010) Fungal endophytes of native grasses decrease insect herbivore preference and performance. <i>Oecologia</i> 164:431–444	676 677 678
Dallas JW, Warne RW (2022) Captivity and animal microbiomes: potential roles of microbiota for influencing animal conservation. <i>Microbial Ecology</i> pp 1–19	679 680 681
Davison R, Nicole F, Jacquemyn H, et al (2013) Contributions of covariance: decomposing the components of stochastic population growth in <i>cypripedium calceolus</i> . <i>The American Naturalist</i> 181(3):410–420	682 683 684 685
Davison R, Stadman M, Jongejans E (2019) Stochastic effects contribute to population fitness differences. <i>Ecological Modelling</i> 408:108760	686 687 688
Decunta FA, Pérez LI, Malinowski DP, et al (2021) A systematic review on the effects of epichloë fungal endophytes on drought tolerance in cool-season grasses. <i>Frontiers</i>	689 690

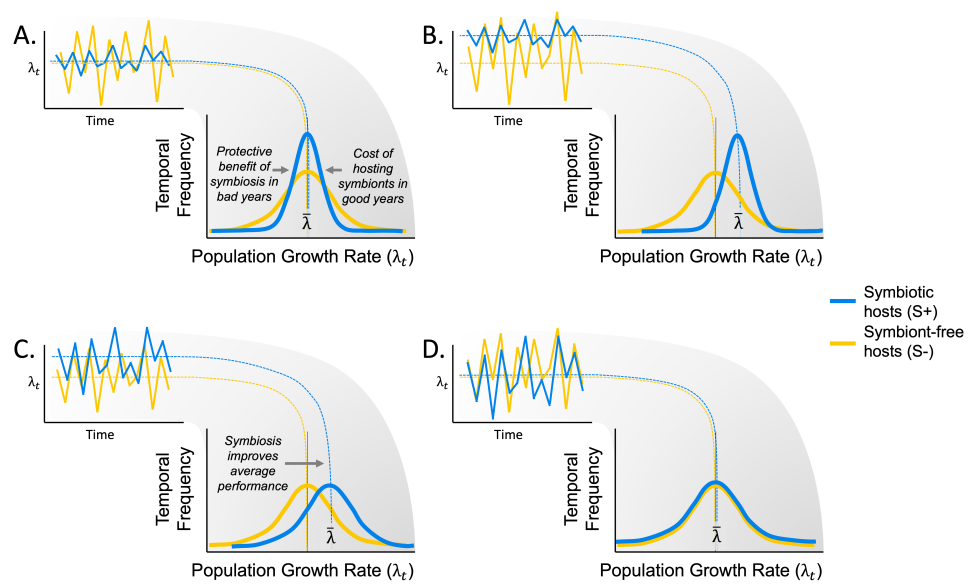
- 691 in plant science 12:644731  
692
- 693 Doak DF, Morris WF, Pfister C, et al (2005) Correctly estimating how environmental  
694 stochasticity influences fitness and population growth. *The American Naturalist*  
695 166(1):E14–E21
- 696 Dunbar HE, Wilson ACC, Ferguson NR, et al (2007) Aphid thermal tolerance is  
697 governed by a point mutation in bacterial symbionts. *PLoS biology* 5(5):e96
- 698
- 699 Ehrlén J, Morris WF (2015) Predicting changes in the distribution and abundance of  
700 species under environmental change. *Ecology letters* 18(3):303–314
- 701
- 702 Elderd BD, Miller TE (2016) Quantifying demographic uncertainty: Bayesian methods  
703 for integral projection models. *Ecological Monographs* 86(1):125–144
- 704
- 705 Ellis MM, Crone EE (2013) The role of transient dynamics in stochastic population  
706 growth for nine perennial plants. *Ecology* 94(8):1681–1686
- 707
- 708 Ellner SP, Childs DZ, Rees M, et al (2016) Data-driven modelling of structured  
709 populations. A practical guide to the Integral Projection Model Cham: Springer
- 710
- 711 Ellner SP, Adler PB, Childs DZ, et al (2022) A critical comparison of integral  
712 projection and matrix projection models for demographic analysis: Comment.  
713 *Ecology*
- 714
- 715 Fieberg J, Ellner SP (2001) Stochastic matrix models for conservation and manage-  
716 ment: a comparative review of methods. *Ecology letters* 4(3):244–266
- 717
- 718 Fine PE (1975) Vectors and vertical transmission: an epidemiologic perspective.  
719 *Annals of the New York Academy of Sciences* 266(1):173–194
- 720
- 721 Funkhouser LJ, Bordenstein SR (2013) Mom knows best: the universality of maternal  
722 microbial transmission. *PLoS biology* 11(8):e1001631
- 723
- 724 Gabry J, Simpson D, Vehtari A, et al (2019) Visualization in bayesian workflow.  
725 *Journal of the Royal Statistical Society Series A: Statistics in Society* 182(2):389–402
- 726
- 727 Gelman A, Hill J (2006) Data analysis using regression and multilevel/hierarchical  
728 models. Cambridge university press
- 729
- 730 Henry LP, Bruijning M, Forsberg SK, et al (2021) The microbiome extends host  
731 evolutionary potential. *Nature communications* 12(1):5141
- 732
- 733 Hilde CH, Gamelon M, Sæther BE, et al (2020) The Demographic Buffering Hypothe-  
734 sis: Evidence and Challenges. *Trends in Ecology & Evolution* 0(0). <https://doi.org/10.1016/j.tree.2020.02.004>, URL [https://www.cell.com/trends/ecology-evolution/abstract/S0169-5347\(20\)30050-1](https://www.cell.com/trends/ecology-evolution/abstract/S0169-5347(20)30050-1), publisher: Elsevier
- 735
- 736

IPCC (2021) Climate change 2021: The physical science basis. URL <a href="https://www.ipcc.ch/report/ar6/wg1/">https://www.ipcc.ch/report/ar6/wg1/</a>	737 738 739
Jeschke JM, Kokko H (2009) The roles of body size and phylogeny in fast and slow life histories. <i>Evolutionary Ecology</i> 23(6):867–878	740 741 742
Jones OR, Barks P, Stott I, et al (2022) Rcompadre and rage—two r packages to facilitate the use of the compadre and comadre databases and calculation of life-history traits from matrix population models. <i>Methods in Ecology and Evolution</i> 13(4):770–781	743 744 745 746
Jordano P (1994) Spatial and temporal variation in the avian-frugivore assemblage of prunus mahaleb: patterns and consequences. <i>Oikos</i> pp 479–491	747 748 749
Kivlin SN, Emery SM, Rudgers JA (2013) Fungal symbionts alter plant responses to global change. <i>American Journal of Botany</i> 100(7):1445–1457	750 751 752
Koops DN, Pavard S, Baudisch A, et al (2009) Is life-history buffering or lability adaptive in stochastic environments? <i>Oikos</i> 118(7):972–980	753 754 755
Kuparinen A, Boit A, Valdovinos FS, et al (2016) Fishing-induced life-history changes degrade and destabilize harvested ecosystems. <i>Scientific reports</i> 6(1):22245	756 757 758
Lange C, Boyer S, Bezemer TM, et al (2023) Impact of intraspecific variation in insect microbiomes on host phenotype and evolution. <i>The ISME journal</i> 17(11):1798–1807	759 760
Le Coeur C, Yoccoz NG, Salguero-Gómez R, et al (2022) Life history adaptations to fluctuating environments: Combined effects of demographic buffering and lability. <i>Ecology Letters</i> 25(10):2107–2119	761 762 763 764
Leuchtmann A (1992) Systematics, distribution, and host specificity of grass endophytes. <i>Natural toxins</i> 1(3):150–162	765 766 767
Leuchtmann A, Bacon CW, Schardl CL, et al (2014) Nomenclatural realignment of neotyphodium species with genus epichloë. <i>Mycologia</i> 106(2):202–215	768 769 770
Lewontin RC, Cohen D (1969) On Population Growth in a Randomly Varying Environment. <i>Proceedings of the National Academy of Sciences</i> 62(4):1056–1060. <a href="https://doi.org/10.1073/pnas.62.4.1056">https://doi.org/10.1073/pnas.62.4.1056</a> , URL <a href="https://www.pnas.org/content/62/4/1056">https://www.pnas.org/content/62/4/1056</a> , publisher: National Academy of Sciences Section: Biological Sciences: Zoology	771 772 773 774 775
McFall-Ngai M, Hadfield MG, Bosch TC, et al (2013) Animals in a bacterial world, a new imperative for the life sciences. <i>Proceedings of the National Academy of Sciences</i> 110(9):3229–3236	776 777 778
Menges ES (2000) Applications of population viability analyses in plant conservation. <i>Ecological Bulletins</i> pp 73–84	779 780 781 782

- 783 Metcalf CJE, Ellner SP, Childs DZ, et al (2015) Statistical modelling of annual vari-  
784     ation for inference on stochastic population dynamics using integral projection  
785     models. *Methods in Ecology and Evolution* 6(9):1007–1017
- 786
- 787 Moles AT, Westoby M (2004) Seedling survival and seed size: a synthesis of the  
788     literature. *Journal of Ecology* 92(3):372–383
- 789
- 790 Morris WF, Pfister CA, Tuljapurkar S, et al (2008) Longevity can buffer plant and  
791     animal populations against changing climatic variability. *Ecology* 89(1):19–25
- 792
- 793 Murphy GI (1968) Pattern in life history and the environment. *The American*  
794     *Naturalist* 102(927):391–403
- 795
- 796 Neyaz M, Gardner DR, Creamer R, et al (2022) Localization of the swainsonine-  
797     producing chaetothyriales symbiont in the seed and shoot apical meristem in its  
798     host *Ipomoea carnea*. *Microorganisms* 10(3):545
- 799
- 800 of North America Editorial Committee F (1993) Poaceae. *Flora of North America*  
801     North of Mexico [Online] 24. URL <http://floranorthamerica.org/Poaceae>
- 802
- 803 Pfister CA (1998) Patterns of variance in stage-structured populations: evolutionary  
804     predictions and ecological implications. *Proceedings of the National Academy of*  
805     *Sciences* 95(1):213–218
- 806
- 807 Rees M (1996) Evolutionary ecology of seed dormancy and seed size. *Philosophical*  
808     *Transactions of the Royal Society of London Series B: Biological Sciences*  
809     351(1345):1299–1308
- 810
- 811 Rees M, Ellner SP (2009) Integral projection models for populations in temporally  
812     varying environments. *Ecological Monographs* 79(4):575–594
- 813
- 814 Reyna R, Cooke P, Grum D, et al (2012) Detection and localization of the endophyte  
815     undifilum oxytropis in locoweed tissues. *Botany* 90(12):1229–1236
- 816
- 817 Rodriguez R, White Jr J, Arnold AE, et al (2009) Fungal endophytes: diversity and  
818     functional roles. *New Phytologist* 182(2):314–330
- 819
- 820 Rodríguez-Caro RC, Capdevila P, Graciá E, et al (2021) The limits of demographic  
821     buffering in coping with environmental variation. *Oikos* 130(8):1346–1358
- 822
- 823 Rudgers JA, Clay K (2008) An invasive plant-fungal mutualism reduces arthropod  
824     diversity. *Ecology Letters* 11(8):831–840
- 825
- 826 Russell JA, Moran NA (2006) Costs and benefits of symbiont infection in aphids: vari-  
827     ation among symbionts and across temperatures. *Proceedings of the Royal Society*  
828     B: *Biological Sciences* 273(1586):603–610

Saikkonen K, Gundel PE, Helander M (2013) Chemical ecology mediated by fungal endophytes in grasses. <i>Journal of chemical ecology</i> 39:962–968	829 830 831
Seneviratne S, Nicholls N, Easterling D, et al (2012) Changes in climate extremes and their impacts on the natural physical environment. Cambridge University Press	832 833 834
Smith E, Vaughan G, Ketchum R, et al (2017) Symbiont community stability through severe coral bleaching in a thermally extreme lagoon. <i>Scientific Reports</i> 7(1):2428	835 836 837
Stan Development Team (2022) RStan: the R interface to Stan. URL <a href="https://mc-stan.org/">https://mc-stan.org/</a> , r package version 2.21.7	838 839 840
Swain DL, Langenbrunner B, Neelin JD, et al (2018) Increasing precipitation volatility in twenty-first-century California. <i>Nature Climate Change</i> 8(5):427–433	841 842 843
Tuljapurkar S (2013) Population dynamics in variable environments, vol 85. Springer Science & Business Media	844 845 846
Tuljapurkar S, Haridas C (2006) Temporal autocorrelation and stochastic population growth. <i>Ecology Letters</i> 9(3):327–337	847 848 849
Tuljapurkar S, Orzack SH (1980) Population dynamics in variable environments i. long-run growth rates and extinction. <i>Theoretical Population Biology</i> 18(3):314–342	850 851 852
Tuljapurkar SD (1982) Population dynamics in variable environments. III. Evolutionary dynamics of r-selection. <i>Theoretical Population Biology</i> 21(1):141–165. <a href="https://doi.org/10.1016/0040-5809(82)90010-7">https://doi.org/10.1016/0040-5809(82)90010-7</a> , URL <a href="http://www.sciencedirect.com/science/article/pii/0040580982900107">http://www.sciencedirect.com/science/article/pii/0040580982900107</a>	853 854 855
Vandenkoornhuyse P, Quaiser A, Duhamel M, et al (2015) The importance of the microbiome of the plant holobiont. <i>New Phytologist</i> 206(4):1196–1206	856 857 858
Vicente-Serrano SM, Beguería S, López-Moreno JI (2010) A multiscale drought index sensitive to global warming: the standardized precipitation evapotranspiration index. <i>Journal of Climate</i> 23(7):1696–1718	859 860 861
Williams JL, Miller TE, Ellner SP (2012) Avoiding unintentional eviction from integral projection models. <i>Ecology</i> 93(9):2008–2014	862 863 864
Wu L, Zhang Y, Guo X, et al (2022) Reduction of microbial diversity in grassland soil is driven by long-term climate warming. <i>Nature Microbiology</i> 7(7):1054–1062	865 866 867
Yule KM, Miller TE, Rudgers JA (2013) Costs, benefits, and loss of vertically transmitted symbionts affect host population dynamics. <i>Oikos</i> 122(10):1512–1520	868 869 870
Zanne AE, Tank DC, Cornwell WK, et al (2014) Three keys to the radiation of angiosperms into freezing environments. <i>Nature</i> 506(7486):89–92	871 872 873
	874

875 **Figures**



897 **Fig. 1:** Hypothesized effects of symbiosis on the mean and variance of annual popula-  
 898 tion growth rates. (A) Context-dependent symbiosis may provide benefits to hosts  
 899 during harsh years while being neutral or costly during benign years. Temporal vari-  
 900 ance in populations growth rates of symbiotic host populations (S+; blue lines) is  
 901 expected to decrease relative to symbiont-free hosts (S-; yellow lines). (B) Symbiosis  
 902 may improve average performance across years in addition to reducing temporal vari-  
 903 ance. (C) Consistent benefits of symbiosis could improve average performance across  
 904 years with no influence on temporal variance. (D) Symbiosis may have an effectively  
 905 neutral effect on population growth rates.

921  
 922  
 923  
 924  
 925  
 926  
 927  
 928  
 929  
 930  
 931  
 932  
 933  
 934  
 935  
 936  
 937  
 938  
 939  
 940  
 941  
 942  
 943  
 944  
 945  
 946  
 947  
 948  
 949  
 950  
 951  
 952  
 953  
 954  
 955  
 956  
 957  
 958  
 959  
 960  
 961  
 962  
 963  
 964  
 965  
 966

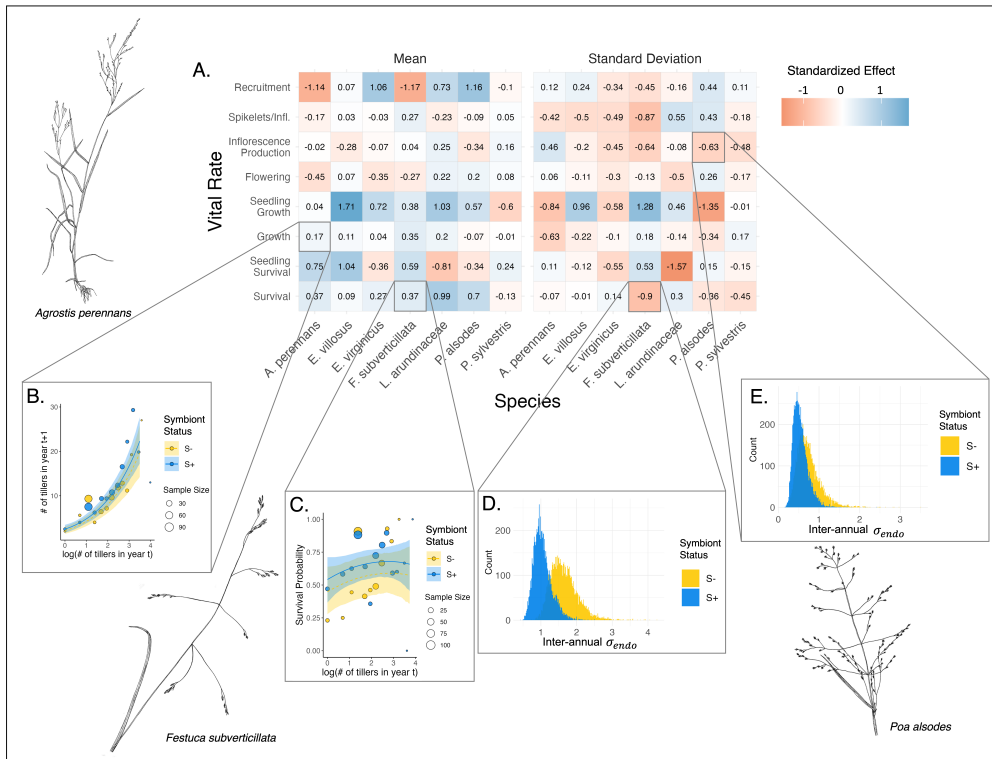
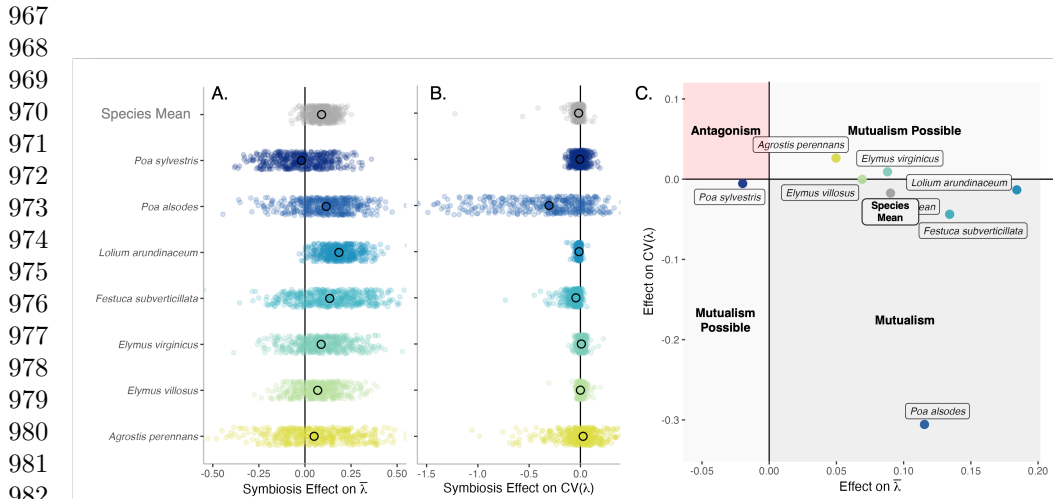
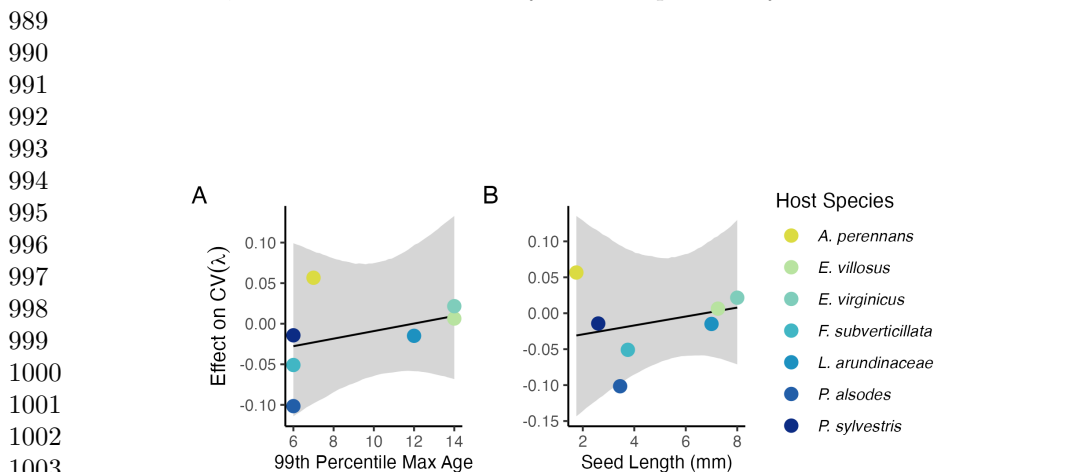


**Fig. 2:** Endophyte symbiosis altered host vital rates.(A) Shading represents the posterior mean standardized effect size (Cohen's D) of endophyte symbiosis on mean or standard deviation of host vital rates (blue indicates that symbiosis increased the mean or standard deviation and red indicates a reduction). Endophytes' diverse vital rate effects include increased (B) mean growth of *A. perennans* and (C) mean survival probability of *F. subverticillata*. Endophyte presence also reduced inter-annual standard deviation in (D) the survival of *F. subverticillata* and (E) the fertility of *P. alsodes*. In panels B-C, expected mean vital rates that average across years and plots are shown with 80% credible intervals along with points representing data binned by size for symbiotic (S+) and symbiont-free (S-) plants. Panels D-E show estimated posterior distributions of endophyte-status specific inter-annual standard deviation ( $\sigma_{\tau_{e,h}}^2$ ) for each vital rate for S+ (blue) and S- (beige) populations. Organism silhouettes modified from "Festuca subverticillata" by Cindy Roché and "Agrostis hyemalis" and "Poa alsodes" by Sandy Long ©Utah State University.



983 **Fig. 3:** Mean and variance-buffering effects on fitness. Black circles indicate the  
984 posterior median effect of endophytes along with 500 posterior draws (smaller colored  
985 circles) on the (A) mean and (B) coefficient of variation in  $\lambda_t$  for each host  
986 species as well as a cross species mean. (C) For all hosts, endophytes either reduce  
987 variance, increase the mean, or both, and consequently when considering stochastic  
988 environments, the interactions are always at least potentially mutualistic.



1004 **Fig. 4:** Host species with faster life history traits experience stronger effects of  
1005 symbiont-mediated variance buffering. Regressions between life history traits describ-  
1006 ing the fast-slow life history continuum ((A) 99th percentile maximum age observed  
1007 during long term censuses in years; (B) Seed size) and the effect of endophyte sym-  
1008 biosis on the coefficient of variation in annual population growth rate ( $\lambda_t$ ). Each panel  
1009 shows the fitted mean relationship (line) along with the 95% credible interval.  
1010  
1011  
1012

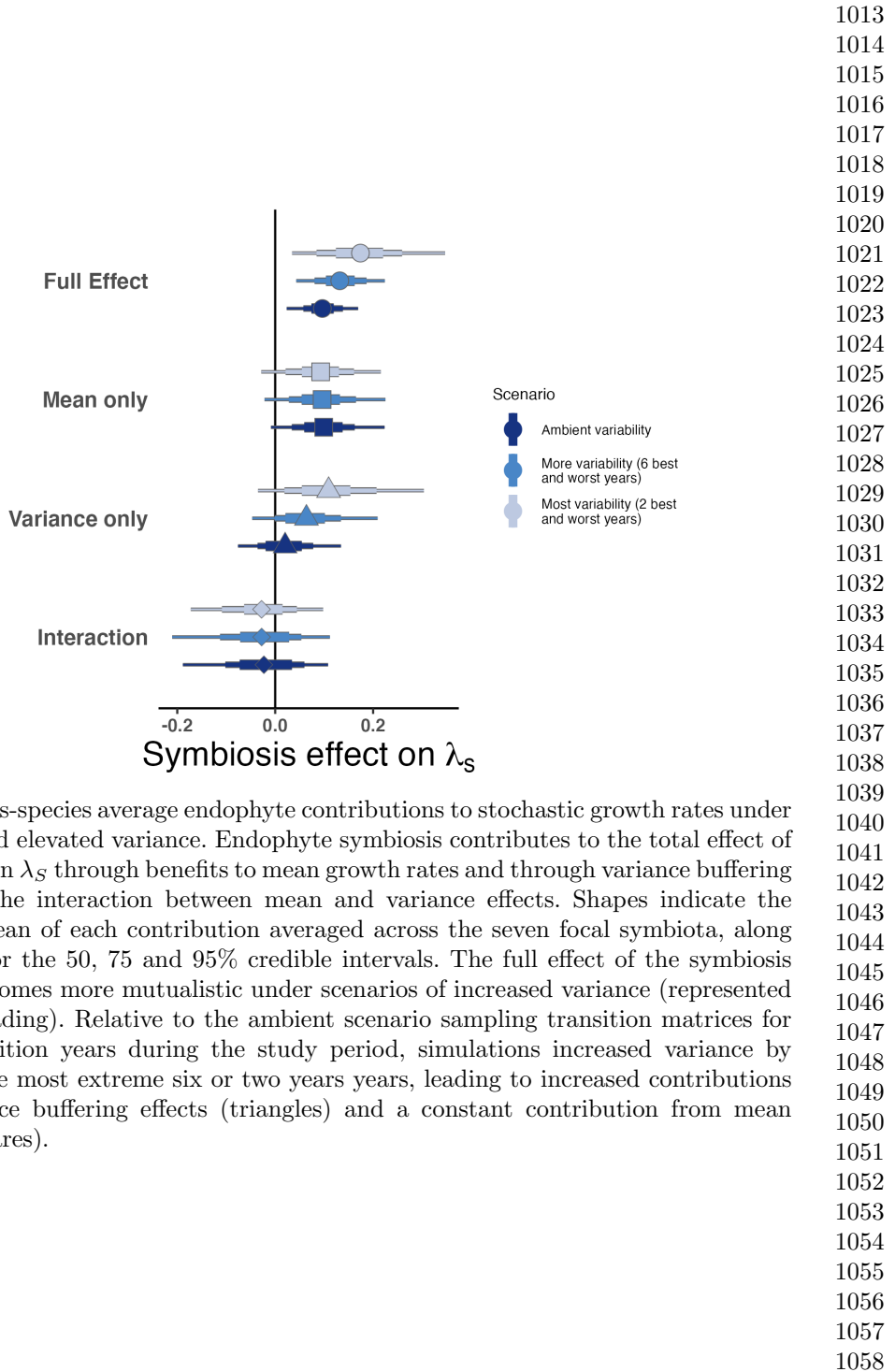


**Fig. 5:** Cross-species average endophyte contributions to stochastic growth rates under observed and elevated variance. Endophyte symbiosis contributes to the total effect of mutualism on  $\lambda_S$  through benefits to mean growth rates and through variance buffering as well as the interaction between mean and variance effects. Shapes indicate the posterior mean of each contribution averaged across the seven focal symbiota, along with bars for the 50, 75 and 95% credible intervals. The full effect of the symbiosis (circles) becomes more mutualistic under scenarios of increased variance (represented by color shading). Relative to the ambient scenario sampling transition matrices for all 13 transition years during the study period, simulations increased variance by sampling the most extreme six or two years years, leading to increased contributions from variance buffering effects (triangles) and a constant contribution from mean effects (squares).

1059 **Supporting Information**  
1060

1061  
1062 **Table of Contents**  
1063

---

1064	<b>Supplemental Methods</b>	<b>29</b>
1065	Endophyte removal, plant propagation, and field set-up . . . . .	29
1066	Detailed vital rate modeling . . . . .	29
1067	Estimating climate drivers of environmental context-dependence . . . . .	31
1068	Detailed statistical analysis of life history traits . . . . .	33
1069	Vital rate mean-variance decomposition . . . . .	33
1070		
1071	<b>Supplemental Figures S1-S89</b>	<b>35</b>
1072		
1073	<b>Supplemental Tables S1-S3</b>	<b>120</b>
1074		

1075  
1076  
1077 **List of Supp. Figures**  
1078

1079	S1 Life cycle diagram depicting the generalized structure of matrix population model . . . . .	34
1080		
1081	S2 Effect of endophyte symbiosis on mean adult survival - Original . . . . .	35
1082	S3 Effect of endophyte symbiosis on mean adult survival - Recruits . . . . .	36
1083	S4 Effect of endophyte symbiosis on mean adult growth - Original . . . . .	37
1084	S5 Effect of endophyte symbiosis on mean adult growth - Recruits . . . . .	38
1085	S6 Effect of endophyte symbiosis on mean flowering - Original . . . . .	39
1086	S7 Effect of endophyte symbiosis on mean flowering - Recruits . . . . .	40
1087	S8 Effect of endophyte symbiosis on mean fertility - Original . . . . .	41
1088	S9 Effect of endophyte symbiosis on mean fertility - Recruits . . . . .	42
1089	S10 Effect of endophyte symbiosis on mean spikelet production - Original . . . . .	43
1090	S11 Effect of endophyte symbiosis on mean spikelet production - Recruits . . . . .	44
1091	S12 Effect of endophyte symbiosis on yearly adult survival - Original . . . . .	45
1092	S13 Effect of endophyte symbiosis on yearly adult survival - Recruits . . . . .	46
1093	S14 Effect of endophyte symbiosis on yearly adult growth - Original . . . . .	47
1094	S15 Effect of endophyte symbiosis on yearly adult growth - Recruits . . . . .	48
1095	S16 Effect of endophyte symbiosis on yearly flowering - Original . . . . .	49
1096	S17 Effect of endophyte symbiosis on yearly flowering - Recruits . . . . .	50
1097	S18 Effect of endophyte symbiosis on yearly fertility - Original . . . . .	51
1098	S19 Effect of endophyte symbiosis on yearly fertility - Recruits . . . . .	52
1099	S20 Effect of endophyte symbiosis on yearly spikelet production - Original . . . . .	53
1100	S21 Effect of endophyte symbiosis on yearly spikelet production - Recruits . . . . .	54
1101	S22 Posterior distributions of the standard deviations of inter-annual year effects for survival . . . . .	55
1102		
1103	S23 Posterior distributions of the standard deviations of inter-annual year effects for seedling survival . . . . .	55
1104		

S24	Posterior distributions of the standard deviations of inter-annual year effects for growth . . . . .	56	1105
S25	Posterior distributions of the standard deviations of inter-annual year effects for seedling growth . . . . .	56	1106
S26	Posterior distributions of the standard deviations of inter-annual year effects for flowering probability . . . . .	57	1107
S27	Posterior distributions of the standard deviations of inter-annual year effects for fertility . . . . .	57	1108
S28	Posterior distributions of the standard deviations of inter-annual year effects for spikelets per inflorescence . . . . .	58	1109
S29	Posterior distributions of the standard deviations of inter-annual year effects for recruitment . . . . .	58	1110
S30	Graphical posterior predictive check for mean and higher moments of <i>A. perennans</i> growth model across size . . . . .	59	1111
S31	Graphical posterior predictive check for mean and higher moments of <i>E. villosus</i> growth model across size . . . . .	60	1112
S32	Graphical posterior predictive check for mean and higher moments of <i>E. virginicus</i> growth model across size . . . . .	61	1113
S33	Graphical posterior predictive check for mean and higher moments of <i>F. subverticillata</i> growth model across size . . . . .	62	1114
S34	Graphical posterior predictive check for mean and higher moments of <i>L. arundinacea</i> growth model across size . . . . .	63	1115
S35	Graphical posterior predictive check for mean and higher moments of <i>P. alsodes</i> growth model across size . . . . .	64	1116
S36	Graphical posterior predictive check for mean and higher moments of <i>P. sylvestris</i> growth model across size . . . . .	65	1117
S37	Graphical posterior predictive check for mean and higher moments of <i>A. perennans</i> survival model across size . . . . .	66	1118
S38	Graphical posterior predictive check for mean and higher moments of <i>E. villosus</i> survival model across size . . . . .	67	1119
S39	Graphical posterior predictive check for mean and higher moments of <i>E. virginicus</i> survival model across size . . . . .	68	1120
S40	Graphical posterior predictive check for mean and higher moments of <i>F. subverticillata</i> survival model across size . . . . .	69	1121
S41	Graphical posterior predictive check for mean and higher moments of <i>L. arundinacea</i> survival model across size . . . . .	70	1122
S42	Graphical posterior predictive check for mean and higher moments of <i>P. alsodes</i> survival model across size . . . . .	71	1123
S43	Graphical posterior predictive check for mean and higher moments of <i>P. sylvestris</i> survival model across size . . . . .	72	1124
S44	Graphical posterior predictive check for mean and higher moments of <i>A. perennans</i> inflorescence production model across size . . . . .	73	1125
S45	Graphical posterior predictive check for mean and higher moments of <i>E. villosus</i> inflorescence production model across size . . . . .	74	1126

1151	S46 Graphical posterior predictive check for mean and higher moments of <i>E. virginicus</i> inflorescence production model across size . . . . .	75
1152		
1153	S47 Graphical posterior predictive check for mean and higher moments of <i>F. subverticillata</i> inflorescence production model across size . . . . .	76
1154		
1155	S48 Graphical posterior predictive check for mean and higher moments of <i>L. arundinacea</i> inflorescence production model across size . . . . .	77
1156		
1157	S49 Graphical posterior predictive check for mean and higher moments of <i>P. alsodes</i> inflorescence production model across size . . . . .	78
1158		
1159	S50 Graphical posterior predictive check for mean and higher moments of <i>P. sylvestris</i> inflorescence production model across size . . . . .	79
1160		
1161	S51 Graphical posterior predictive check for mean and higher moments of <i>A. perennans</i> spikelet model across size . . . . .	80
1162		
1163	S52 Graphical posterior predictive check for mean and higher moments of <i>E. villosus</i> spikelet model across size . . . . .	81
1164		
1165	S53 Graphical posterior predictive check for mean and higher moments of <i>E. virginicus</i> spikelet model across size . . . . .	82
1166		
1167	S54 Graphical posterior predictive check for mean and higher moments of <i>F. subverticillata</i> spikelet model across size . . . . .	83
1168		
1169	S55 Graphical posterior predictive check for mean and higher moments of <i>L. arundinacea</i> spikelet model across size . . . . .	84
1170		
1171	S56 Graphical posterior predictive check for mean and higher moments of <i>P. alsodes</i> spikelet model across size . . . . .	85
1172		
1173	S57 Graphical posterior predictive check for mean and higher moments of <i>P. sylvestris</i> spikelet model across size . . . . .	86
1174		
1175	S58 Graphical posterior predictive check for mean and higher moments of <i>A. perennans</i> flowering model across size. . . . .	87
1176		
1177	S59 Graphical posterior predictive check for mean and higher moments of <i>E. villosus</i> flowering model across size . . . . .	88
1178		
1179	S60 Graphical posterior predictive check for mean and higher moments of <i>E. virginicus</i> flowering model across size . . . . .	89
1180		
1181	S61 Graphical posterior predictive check for mean and higher moments of <i>F. subverticillata</i> flowering model across size . . . . .	90
1182		
1183	S62 Graphical posterior predictive check for mean and higher moments of <i>L. arundinacea</i> flowering model across size . . . . .	91
1184		
1185	S63 Graphical posterior predictive check for mean and higher moments of <i>P. alsodes</i> flowering model across size . . . . .	92
1186		
1187	S64 Graphical posterior predictive check for mean and higher moments of <i>P. sylvestris</i> flowering model across size . . . . .	93
1188		
1189	S65 Graphical posterior predictive check for statistical model of Seedling Survival . . . . .	94
1190		
1191	S66 Graphical posterior predictive check for statistical model of Seedling Growth . . . . .	95
1192		
1193	S67 Graphical posterior predictive check for statistical model of Mean Seeds/Spikelet . . . . .	96
1194		
1195	S68 Graphical posterior predictive check for statistical model of Recruitment	97
1196		

S69	Posterior distributions of the vital rate regressions for Adult Survival . . . . .	98	1197
S70	Posterior distributions of the vital rate regressions for Seedling Survival . . . . .	99	1198
S71	Posterior distributions of the vital rate regressions for Adult Growth . . . . .	100	1199
S72	Posterior distributions of the vital rate regressions for Seedling Growth . . . . .	101	1200
S73	Posterior distributions of the vital rate regressions for Flowering Probability . . . . .	102	1201
S74	Posterior distributions of the vital rate regressions for Inflorescence Production . . . . .	103	1203
S75	Posterior distributions of the vital rate regressions for Spikelets/Inflorescence . . . . .	104	1205
S76	Posterior distributions of the vital rate regressions for Seeds/Spikelet . . . . .	105	1207
S77	Posterior distributions of the vital rate regressions for Recruitment . . . . .	106	1208
S78	Annual growth rate values ( $\lambda_t$ ) over thirteen years . . . . .	107	1209
S79	Stochastic population growth rates ( $\lambda_S$ ) for symbiotic and symbiont-free populations . . . . .	108	1210
S80	Mean and standard deviation of annual growth rate values during simulation scenarios . . . . .	109	1211
S81	Endophyte contributions to stochastic growth rates under observed and elevated variance across species . . . . .	110	1212
S82	Vital rate decomposition of endophyte contributions to stochastic growth rates under observed and elevated variance across species . . . . .	111	1213
S83	Relationship between variance buffering and life history traits describing the fast-slow life history continuum accounting for phylogenetic covariance between <i>Epichloë</i> symbionts . . . . .	112	1214
S84	Relationship between variance buffering and life history traits describing the fast-slow life history continuum accounting for phylogenetic covariance between <i>Epichloë</i> symbionts . . . . .	113	1215
S85	Posterior estimates of life history trait effects on variance buffering . . . . .	114	1216
S86	Posterior distributions of the life history trait regressions . . . . .	115	1217
S87	Faithfulness of experimental plots to assigned endophyte status . . . . .	116	1218
S88	Weather station time-series for Bloomington, IN . . . . .	117	1219
S89	Predicted population growth rates across drought indices . . . . .	118	1220
			1221
	<b>List of Supp. Tables</b>		1222
S1	Summary of host-endophyte prorogation and transplant methods . . . . .	120	1223
S2	Summary of focal life history traits . . . . .	121	1224
S3	Summary of host-endophyte drought sensitivities . . . . .	122	1225
			1226
			1227
			1228
			1229
			1230
			1231
			1232
			1233
			1234
			1235
			1236
			1237
			1238
			1239
			1240
			1241
			1242

1243 **Supplemental Methods**

1244

1245 **Endophyte removal, plant propagation, and field set-up**

1246 Seeds from naturally symbiotic populations of the seven focal host species were col-  
1247 lected during summer-fall 2006 from Lilly-Dickey Woods and the nearby Bayles Road  
1248 Teaching and Research Preserve (39.220167, -86.542683). To generate symbiotic (S+)  
1249 and symbiont-free (S-) plants from the same genetic lineages, seeds from each species  
1250 were disinfected with a heat treatment described in Table S1 or left untreated. The  
1251 heat treatment created symbiont-free plants by warming seeds to temperatures at  
1252 which the fungus becomes inviable but the host seeds can still germinate.

1253 Both heat-treated and untreated seeds were surface sterilized with bleach to remove  
1254 epiphyllous microbes, cold stratified for up to 4 weeks, then germinated in a growth  
1255 chamber before transfer to the greenhouse at Indiana University where they grew for  
1256 ~ 8 weeks. We confirmed endophyte status by staining thin sections of inner leaf  
1257 sheath with aniline blue and examining tissue for fungal hyphae at 200X magnification  
1258 ([Bacon and White, 2018](#)). We established experimental populations with vegetatively  
1259 propagated clones of similar sizes (ranging from one to six tillers).

1260 During the fall of 2007 and spring of 2008, we established 10 3x3 m plots for *A.*  
1261 *perennans*, *E. villosus*, *E. virginicus*, *F. subverticillata*, and *L. arundinaceum* and 18  
1262 plots for *P. alsodes* and *P. sylvestris*. Half of the plots were randomly assigned to be  
1263 planted with either symbiotic (S+) or symbiont-free (S-) plants, and initiated with  
1264 20 evenly spaced individuals labeled with aluminum tags. In spring 2008, we placed  
1265 plastic deer net fencing around each plot to limit deer herbivory and disturbance;  
1266 damaged fences were regularly replaced.

1267 We expected plots to maintain their endophyte status (S+ or S-) because these  
1268 fungal symbionts are almost exclusively vertically transmitted, and plots were spaced  
1269 a minimum of 5 m apart, limiting seed dispersal or horizontal transmission of the  
1270 symbiont between plots. We regularly confirmed endophyte treatment throughout the  
1271 lifetime of the experiment by opportunistically taking subsets of seeds from reproduc-  
1272 tive individuals and scoring them for their endophyte status with microscopy as above.  
1273 Overall, these scores reflected 98% faithfulness of recruits to their expected endophyte  
1274 status across species and plots (Fig. S87; Supplement data). Additionally, we have  
1275 rarely observed fungal stromata, the fruiting bodies by which *Epichloë* are poten-  
1276 tially transmitted horizontally, provided the fly vector is also present ([Bultman et al,](#)  
1277 [1995](#)). For *A. perennans*, *F. subverticillata*, *L. arundinaceum*, and *P. alsodes*, we never  
1278 observed stromata. We observed stromata only infrequently for *E. villosus*, and even  
1279 more rarely for *E. virginicus* and *P. sylvestris* (Table S2). For these species, stromata  
1280 have only been observed irregularly across years on 35, 4, and 6 plants respectively,  
1281 making up < 0.3% of all censused plants.

1282

1283 **Detailed vital rate modeling**

1284

1285 We fit vital rates models in a Bayesian hierarchical framework. Statistical models for  
1286 adult survival, seedling survival, adult growth, seedling growth, flowering (yes or no),  
1287 fertility of flowering plants (number of flowering tillers), production of seed-bearing  
1288

spikelets (number per inflorescence), the average number of seeds per spikelet, and the recruitment of seedlings from the preceding year's seed production, were constructed as follows:

*Survival* - We modeled survival as a Bernoulli process, where the survival ( $S$ ) of an individual  $i$  in plot  $p$  and census year  $t$  was predicted by the plot-level endophyte status ( $e$ ), host species ( $h$ ), size in the preceding census, and the plant's origin status ( $o$ ; whether it was initially transplanted or naturally recruited into the plot).

$$S_{i,p,e,h,t} \sim Bernoulli(\hat{S}_{i,p,e,h,t}) \quad (S4a)$$

$$\text{logit}(\hat{S}_{i,p,e,h,t}) = \beta_{0_{h,o}} + \beta_{1_h} * \text{endo}_e \quad (S4b)$$

$$+ \beta_{2_{h,o}} * \text{size}_{i,t-1} + \beta_{3_{h,o}} * \text{size}_{i,t-1}^2 + \tau_{e,h,t} + \rho_p \quad (S4c)$$

$$\tau_{e,h,t} \sim \text{Normal}(0, \sigma_{\tau_{e,h}}^2) \quad (S4d)$$

$$\rho_p \sim \text{Normal}(0, \sigma_\rho^2) \quad (S4e)$$

Here,  $\hat{S}$  is the survival probability,  $\beta_{0_{h,o}}$  is an intercept specific to each host species and recruitment origin,  $\beta_{1_h}$  is the endophyte effect,  $\beta_{2_{h,o}}$  is the effect of plant size specific to each species and recruitment origin,  $\beta_{3_{h,o}}$  is a quadratic plant size effect specific to each species and recruitment origin,  $\tau_{e,h,t}$  is a normally distributed year effect for each species and endophyte status with variance  $\sigma_{\tau_{e,h}}^2$ , and  $\rho_p$  is a normally distributed plot effect with variance  $\sigma_\rho^2$  ( $p(e)$  indicates that plot identity is uniquely associated with an endophyte status). We assume that the plot-to-plot variance  $\sigma_\rho^2$  was shared across host species, allowing us to "borrow strength" across the multi-species dataset; other model parameters are unique to host species. We separately modeled the survival of newly recruited seedlings with a similar model but omitting previous size dependence and origin status.

*Growth* - We modeled plant size in census year  $t$  ( $G$ ) with the same linear predictor for the mean as described for survival. Because we measured size as positive integer-valued counts of tillers, we modeled it with a zero-truncated Poisson-inverse Gaussian distribution. This distribution includes a shape parameter  $\lambda_G$  to account for overdispersion in the data. We additionally modeled the growth of newly recruited seedlings separately with a Poisson-inverse Gaussian model omitting size structure and the plants' origin status as with seedling survival.

*Flowering* - We modeled whether or not a plant was flowering during the census ( $P$ ) as a Bernoulli process, with the same linear predictor for the mean as described above for survival except that size dependence for reproductive vital rates was determined by the individual's size during the same census year as opposed to its size during the previous year.

*Fertility* - For a plant that was flowering during the census, its fertility was the number of reproductive tillers produced ( $F$ ), which we modeled as a function of size in the same census period with a zero-truncated Poisson-Inverse Gaussian distribution, with the same linear predictor for the mean as described above.

1335     *Spikelets per Inflorescence* - Spikelet production ( $K$ ) was recorded as integer counts  
1336 on up to three inflorescences per reproducing plant. We modeled these data with a neg-  
1337 ative binomial distribution, with the same linear predictor for the mean as described  
1338 above.

1339     *Seed Production per Spikelet* - For individuals with recorded counts of seed pro-  
1340 duction, we calculated the number of seeds per spikelet from our counts of seeds and  
1341 spikelets per inflorescence, and then modeled seeds per spikelet ( $D$ ) as means of a  
1342 Gaussian distribution for each species and endophyte status. Because we had less  
1343 detailed data across years and plants for seed production than for other reproductive  
1344 vital rates, we omitted both plot and year random effects.

1345     *Seedling Recruitment* - We used a binomial distribution to model the recruitment of  
1346 new seedlings ( $R$ ) into the plots from seeds produced in the preceding year, assuming  
1347 no long-lived seed bank. We included an intercept specific to each host and endophyte  
1348 status and the same random effects structure as in other models. We estimated the  
1349 number of seeds per plot in the preceding year by multiplying the total number of  
1350 reproductive tillers per plant by the mean number of spikelets per inflorescence and  
1351 mean number of seeds per spikelet ( $D$ ). For plants with missing fertility or spikelet  
1352 data, we used the expected number of reproductive tillers ( $F$ ) or of spikelets per  
1353 inflorescence from ( $K$ ), drawing from the full posteriors of our models. We rounded  
1354 this value to get the estimated seed production for each individual, and finally summed  
1355 across all reproductive plants in each year and plot to get the total number of seeds  
1356 produced.

### 1357     **Model assessment**

1358 All parameters were given vague priors (Gabry et al, 2019). We ran each vital rate  
1359 model for 2500 warm-up and 2500 MCMC sampling iterations with three chains. We  
1360 assessed model convergence with trace plots of posterior chains and checked for  $\hat{R}$   
1361 values less than 1.01, indicating low within- and between-chain variation (Brooks and  
1362 Gelman, 1998; Gelman and Hill, 2006). For those models that showed poor conver-  
1363 gence, we extended the MCMC sampling to include 5000 warm-up and 5000 sampling  
1364 iterations, which was only necessary for seedling growth. We visualized the interactions  
1365 between plant size, origin status, and endophyte status for both the interannual mean  
1366 expected value for each vital rate (averaging over year and plot variance) (Fig. S2 -  
1367 S11) and for the expected vital rate values specific to each year (averaging over plot  
1368 variance) (Fig. S12 -S21). We graphically checked vital rate model fit with posterior  
1369 predictive checks comparing simulated and observed data (Fig. S30-S68). Initial anal-  
1370 yses including only linear effects of size produced estimates of endophytes' effects on  
1371 vital rate means and inter-annual variances that were similar to those from the more  
1372 flexible quadratic models, but provided worse fit to size-structure in the data in some  
1373 cases. We therefore proceeded with the more flexible quadratic models. Results from  
1374 subsequent matrix model analyses were qualitatively similar regardless of this choice.  
1375

### 1376     **Estimating climate drivers of environmental**

#### 1377     **context-dependence**

1378

1379 To connect the variance buffering effects of endophytes with inter-annual variability  
1380 in climate, we built climate-explicit stochastic matrix population models from the

vital rate data in addition to the climate-implicit model described in the main text. 1381  
Identifying the potentially complex relationships between vital rates and environmental 1382  
drivers remains a key challenge for accurate forecasts of the ecological impacts of 1383  
environmental stochasticity (Ehrlén and Morris, 2015). We first downloaded temperature 1384  
and precipitation data from a weather station in Bloomington, IN, approx. 27 1385  
km from our study site, using the rnoaa package (Chamberlain et al, 2022). Compared 1386  
to other weather stations in the area, the measurements from Bloomington contain 1387  
the most complete climate record across the study period and are correlated with 1388  
more local measurements from Nashville, IN for years in which local data are available 1389  
(total daily precipitation:  $R^2 = .76$ ; mean daily temperature:  $R^2 = .94$ ). The 1390  
mean annual temperature across the study period was  $11.9\text{ }C^\circ$  (SD:  $1.05\text{ }C^\circ$ ) and the 1391  
average annual precipitation was 1237.9 mm/year (SD: 204.89 mm/year) (Fig. S88). 1392  
Given the known role of endophytes in promoting host drought tolerance, we calculated 1393  
the Standardised Precipitation-Evapotranspiration Index (SPEI) for 3 and 12 1394  
months preceding each annual censuses, reflecting drought during the growing season 1395  
and across the year (Vicente-Serrano et al, 2010). To calculate SPEI, we used the 1396  
Thornthwaite equation to model potential evapotranspiration as implemented in the 1397  
SPEI R package (Beguería and Vicente-Serrano, 2013) 1398

We repeated the process of fitting statistical models for each vital rate as described 1399  
above with the inclusion of a parameter describing the influence of SPEI. We fit 1400  
separate vital rate models incorporating either the growing season or annual drought 1401  
index for each vital rate, except for the model describing the mean number of seeds 1402  
per inflorescence. This model was fit without climate effects because the data came 1403  
from only a few years. Initial analyses indicated similar fits for models including only a 1404  
linear term and those with both linear and quadratic terms describing the relationship 1405  
between the climate driver and the vital rate response, and so we proceeded with 1406  
models including only the linear term. We expected that including climate predictors 1407  
into the models would explain some inter-annual variance in vital rates, shrinking the 1408  
variance associated with the fitted year random effects. We assessed model fit with 1409  
graphic posterior predictive checks and convergence diagnostics as described for the 1410  
climate-implicit analysis. Finally, we next built matrix projection models incorporating 1411  
the climate-dependent vital rate functions to assess the response of symbiotic (S+) vs 1412  
symbiont-free (S-) populations to drought. The model is as described in **Materials** 1413  
and **Methods** with the inclusion of parameters describing the slope of the relationship 1414  
with SPEI. We compared the sensitivity of  $\lambda$  to either annual or seasonal SPEI of S+ 1415  
populations ( $\frac{\Delta\lambda^+}{\Delta\text{SPEI}}$ ) with those of S- populations ( $\frac{\Delta\lambda^-}{\Delta\text{SPEI}}$ ) (Fig. S89; Table S). 1416

Most species were slightly more responsive to growing season rather than annual 1417  
drought conditions, and for most species symbiotic populations were less sensitive to 1418  
SPEI than symbiont-free populations (Fig. S89; Table S3). However, these drought 1419  
indices did not explain the full extent of inter-annual variability in demographic vital 1420  
rates. For example, flowering in *A. perennans* had one of the strongest climate signals 1421  
(82% probability of a positive relationship with SPEI), yet the estimated inter-annual 1422  
variance  $\sigma_{\tau_{e,h}}^2$  for symbiont-free plants shrank from 6.7 to 6.1 after including 3-month 1423  
SPEI as a covariate, suggesting that other factors contribute to inter-annual variability. 1424

1425  
1426

1427 **Detailed statistical analysis of life history traits**

1428 We fit Bayesian phylogenetic mixed-effects models using the brms package (Bürkner,  
 1429 2017) to test the relationship between each life history trait and the effect of symbiosis  
 1430 on the CV of  $\lambda_t$  (a measure of variance buffering) while controlling for phylogenetic  
 1431 non-independence. We pruned species-level phylogenies of plants (Zanne et al, 2014)  
 1432 and *Epichloë* fungi (Leuchtmann et al, 2014) to include the focal species. *Agrostis*  
 1433 *perennans* was not included in the published tree, and so we used the congener *A.*  
 1434 *hyemalis*. We defined separate phylogenetic covariance matrices for the pruned tree  
 1435 for host and symbiont species.

1436 We propagated uncertainty in the estimated variance buffering effect  $V$  with a  
 1437 measurement error model:

1439

$$1440 \quad V_{MEAN,h} \sim Normal(V_{EST,h}, V_{SD,h}) \quad (S5a)$$

$$1442 \quad V_{EST,h} \sim Normal(\mu_h, \sigma) \quad (S5b)$$

$$1443 \quad \mu = \alpha + \beta * trait + \pi_j \quad (S5c)$$

$$1444 \quad \alpha \sim Normal(0, .1) \quad (S5d)$$

$$1445 \quad \beta \sim Normal(0, .1) \quad (S5e)$$

$$1447 \quad \sigma \sim Half-Normal(.05, .01) \quad (S5f)$$

$$1448 \quad \pi_h \sim MVN(0, \sigma_\pi \mathbf{A}) \quad (S5g)$$

$$1449 \quad \sigma_\pi \sim Half-Normal(0, .1) \quad (S5h)$$

1450

1451 Here,  $V_{EST}$  is the variance buffering effect for host species  $h$ , estimated from the  
 1452 posterior mean ( $V_{MEAN}$ ) and standard deviation ( $V_{SD}$ ), propagating uncertainty asso-  
 1453 ciated with the effect of symbiosis. The model includes an intercept ( $\alpha$ ) and slope ( $\beta$ )  
 1454 defining the relationship between variance buffering effect and the life history trait.  
 1455 The residual standard deviation is given by ( $\sigma$ ). We used weakly informative priors  
 1456 to aid model convergence. Each prior was centered at zero, except for the residual  
 1457 standard deviation, which we centered at the standard deviation of the estimated  
 1458 variance buffering effect, .05. The phylogenetic random effect ( $\pi$ ), modeled as a multi-  
 1459 variate normal distribution, has a between-species standard deviation ( $\sigma_\pi$ ) structured  
 1460 by the phylogenetic covariance matrix  $\mathbf{A}$ . We ran each MCMC sampling chain for  
 1461 8000 warmup iterations and 2000 sampling iterations. We assessed model convergence  
 1462 as described above for the vital rate models.

1463

1464 **Vital rate mean-variance decomposition**

1465

1466 We performed a mean-variance decomposition to quantify the extent that mean and  
 1467 variance effects on stochastic population growth rates arise through different vital  
 1468 rates. Specifically, we repeated the calculation of  $\lambda_S$  as described in the main text  
 1469 for symbiotic populations as well as symbiont-free populations, as well as for four  
 1470 additional “treatments”. These treatments differentiate between mortality and growth  
 1471 related vital rates (adult survival, adult growth, seedling survival, and seedling growth)  
 1472 and reproductive vital rates (probability of flowering, inflorescence production, spikelet

production, seed production, and recruitment). Each treatment set vital rate mean  
 and interannual variances according to the symbiont-free parameter values across vital  
 rates while introducing (1) endophyte effects on the vital rate means for survival and  
 growth vital rates only, (2) endophyte effects on the vital rate variances for survival and  
 growth vital rates only, (3) endophyte effects on the vital rate means for reproductive  
 vital rates only, and (4) endophyte effects on the vital rate variances for reproductive  
 vital rates only. 1473  
 1474  
 1475  
 1476  
 1477  
 1478  
 1479  
 1480  
 1481  
 1482  
 1483  
 1484  
 1485  
 1486  
 1487  
 1488  
 1489  
 1490  
 1491  
 1492  
 1493  
 1494  
 1495  
 1496  
 1497  
 1498  
 1499  
 1500  
 1501  
 1502  
 1503  
 1504  
 1505  
 1506  
 1507  
 1508  
 1509  
 1510  
 1511  
 1512  
 1513  
 1514  
 1515  
 1516  
 1517  
 1518

1519 **Supplemental Figures S1-S89**

1520

1521

1522

1523 *Census t*

1524

1525  $n_t^x$

1526

1527

1528

1529

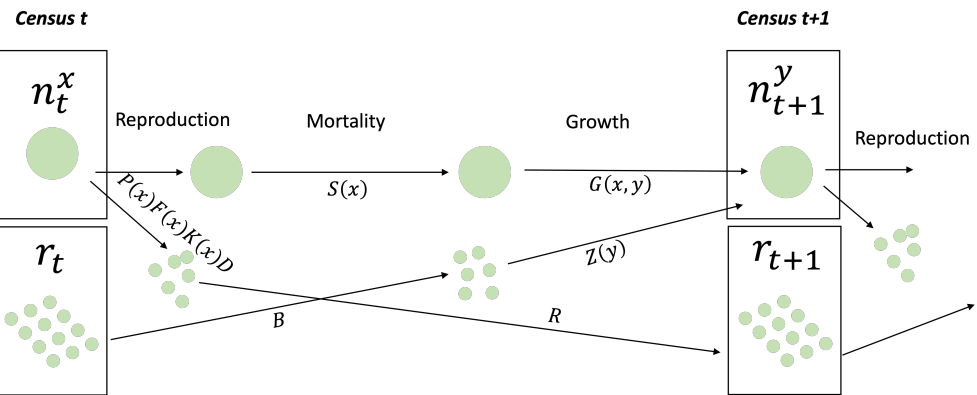
1530

1531

1532

1533

1534



1535 Figure S1: Life cycle diagram depicting the generalized structure of matrix population  
 1536 model. The population consists of different life stages at each census  $t$  or census  $t+1$ .  
 1537 Individuals transition from size  $x$  to size  $y$ .  $n$  is a vector of discrete sizes representing  
 1538 number of tillers, according to their likelihood of survival ( $S$ ) and growth ( $G$ ). Repro-  
 1539 duction generates new recruits (small circles) through four steps, the probability of  
 1540 flowering ( $P$ ), the number of flowering tillers produced ( $F$ ), the number of spikelets  
 1541 per inflorescence produced ( $K$ ), and the number of seeds per spikelet ( $D$ ). The proba-  
 1542 bility of successful recruitment ( $R$ ) determines the success of these offspring, and any  
 1543 new recruits ( $r$ ) are incorporated into the census. These non-reproductive, typically  
 1544 one-tiller recruits transition into the population of mature individuals with survival  
 1545 ( $B$ ) and growth ( $Z$ ) probability. Symbiotic and symbiont-free populations have the  
 1546 same model structure with species-specific and symbiont status-specific transition  
 1547 probabilities used to construct matrices.

1548

1549

1550

1551

1552

1553

1554

1555

1556

1557

1558

1559

1560

1561

1562

1563

1564

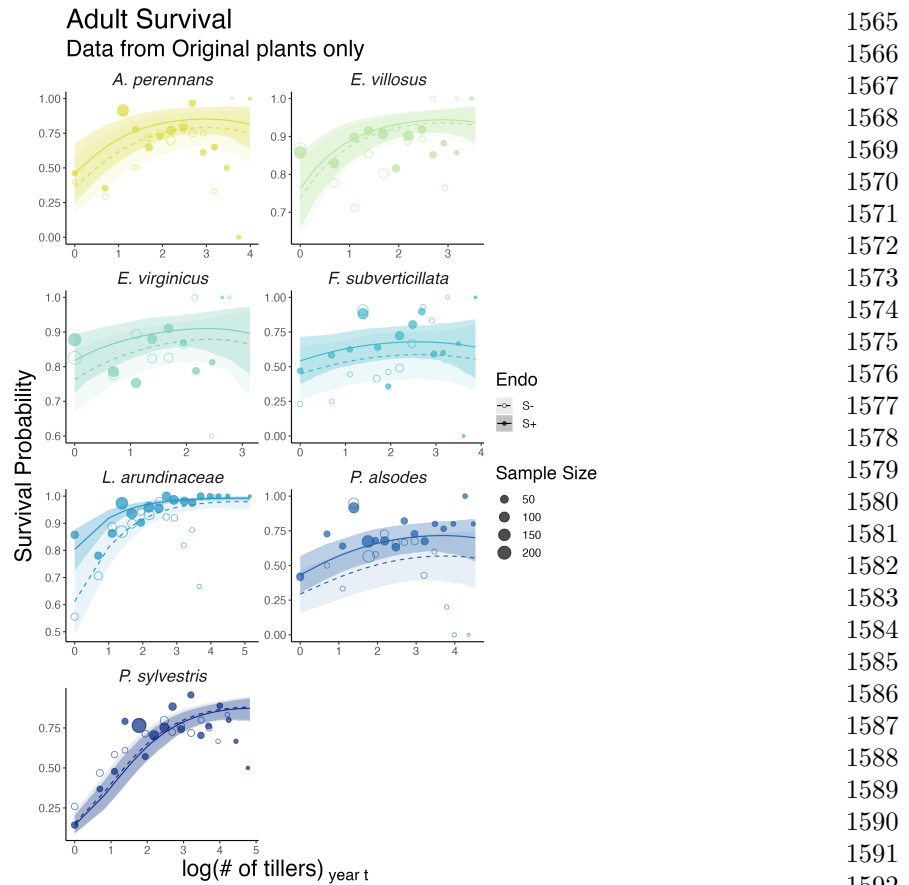
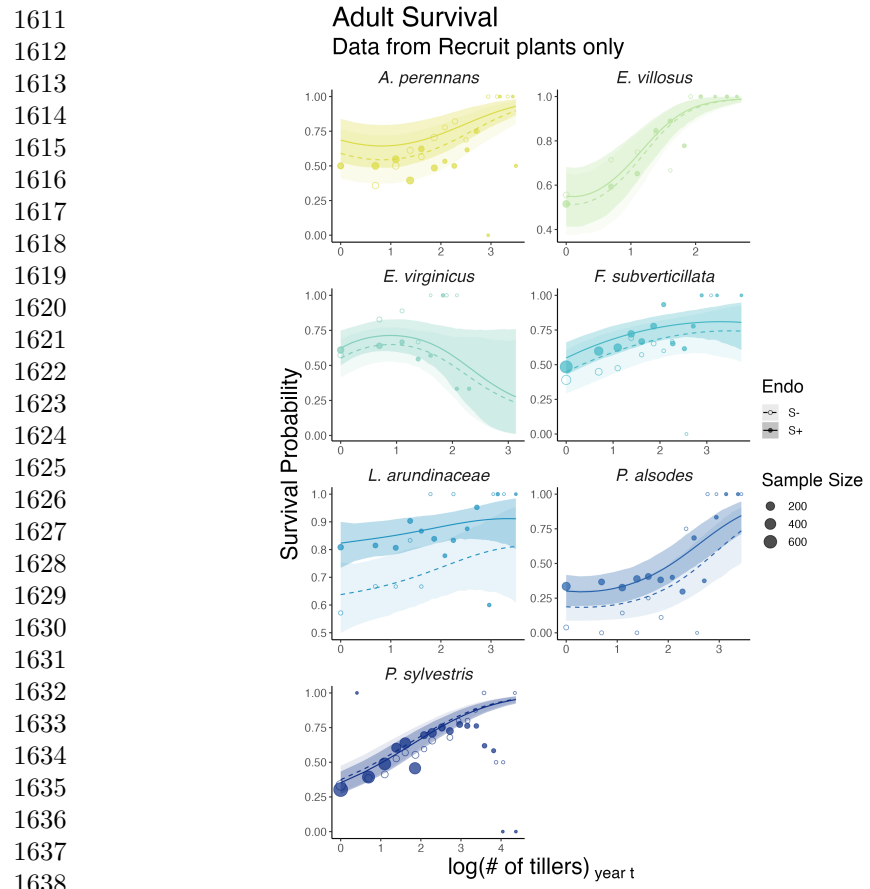


Figure S2: Effect of endophyte symbiosis on mean adult survival. Fitted curves represent the size-specific mean survival probability for originally transplanted plants along with data binned by size and averaged over many individuals, years, and plots shown as open circles with a dashed line for symbiont-free (S-) plants, while the solid line and filled circles represent symbiotic (S+) plants. 80% credible intervals are shown with dark shading for S+, or light shading for S-.



1639 Figure S3: Effect of endophyte symbiosis on mean adult survival. Fitted curves rep-  
1640 resent the size-specific mean survival probability for recruited plants along with data  
1641 binned by size and averaged over many individuals, years, and plots shown as open  
1642 circles with a dashed line for symbiont-free (S-) plants, while the solid line and filled  
1643 circles represent symbiotic (S+) plants. 80% credible intervals are shown with dark  
1644 shading for S+, or light shading for S-.

1645  
1646  
1647  
1648  
1649  
1650  
1651  
1652  
1653  
1654  
1655  
1656

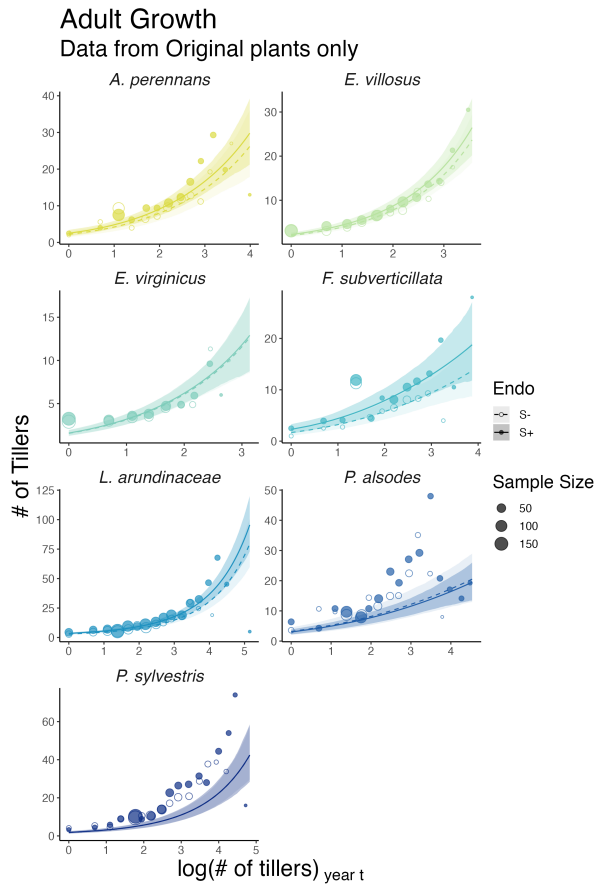
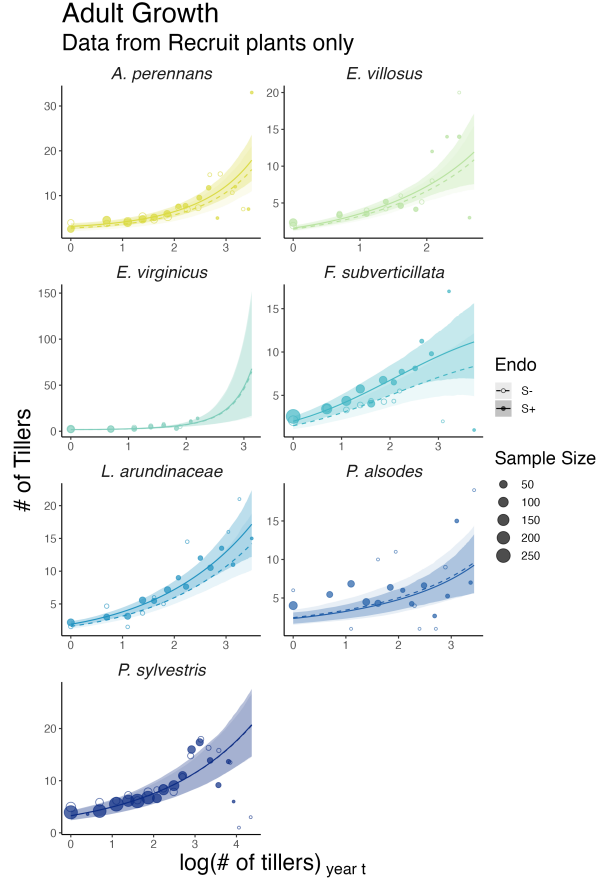


Figure S4: Effect of endophyte symbiosis on mean adult growth. Fitted curves represent the size-specific mean expected plant size for originally transplanted plants along with data binned by size and averaged over many individuals, years, and plots shown as open circles with a dashed line for symbiont-free (S-) plants, while the solid line and filled circles represent symbiotic (S+) plants. 80% credible intervals are shown with dark shading for S+, or light shading for S-.

1657  
1658  
1659  
1660  
1661  
1662  
1663  
1664  
1665  
1666  
1667  
1668  
1669  
1670  
1671  
1672  
1673  
1674  
1675  
1676  
1677  
1678  
1679  
1680  
1681  
1682  
1683  
1684  
1685  
1686  
1687  
1688  
1689  
1690  
1691  
1692  
1693  
1694  
1695  
1696  
1697  
1698  
1699  
1700  
1701  
1702

1703  
1704  
1705  
1706  
1707  
1708  
1709  
1710  
1711  
1712  
1713  
1714  
1715  
1716  
1717  
1718  
1719  
1720  
1721  
1722  
1723  
1724  
1725  
1726  
1727  
1728  
1729  
1730



1731 Figure S5: Effect of endophyte symbiosis on mean adult growth. Fitted curves represent  
1732 the size-specific mean expected plant size for recruited plants along with data binned  
1733 by size and averaged over many individuals, years, and plots shown as open circles  
1734 with a dashed line for symbiont-free (S-) plants, while the solid line and filled circles  
1735 represent symbiotic (S+) plants. 80% credible intervals are shown with dark shading  
1736 for S+, or light shading for S-.

1737  
1738  
1739  
1740  
1741  
1742  
1743  
1744  
1745  
1746  
1747  
1748

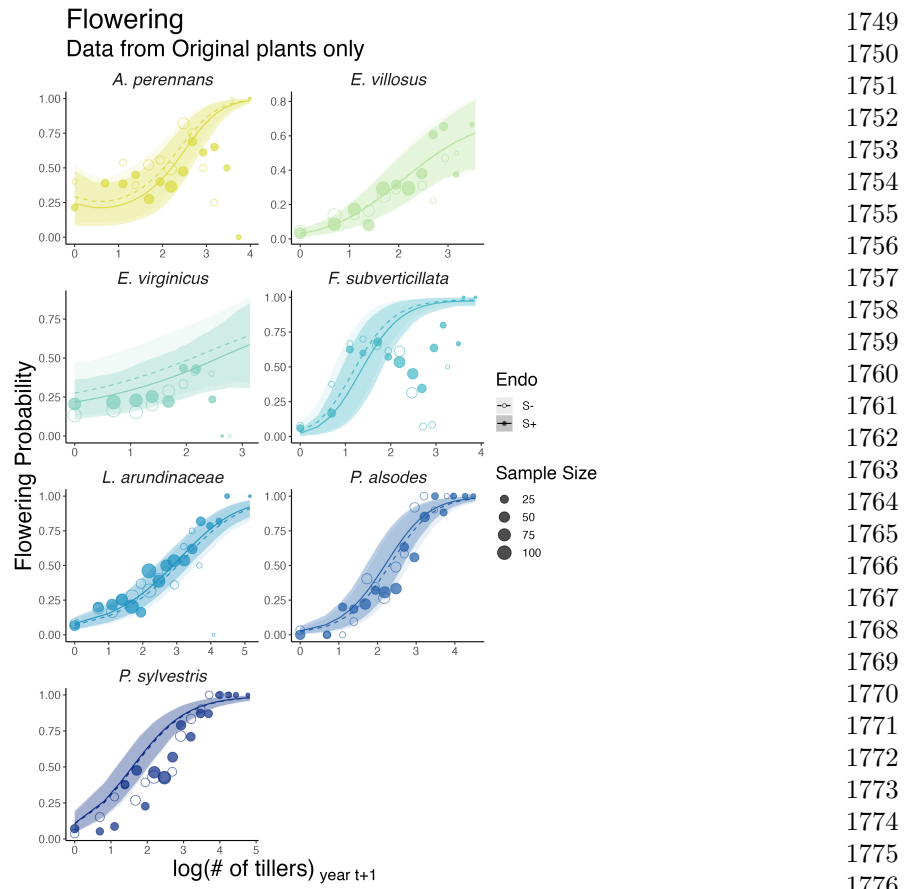
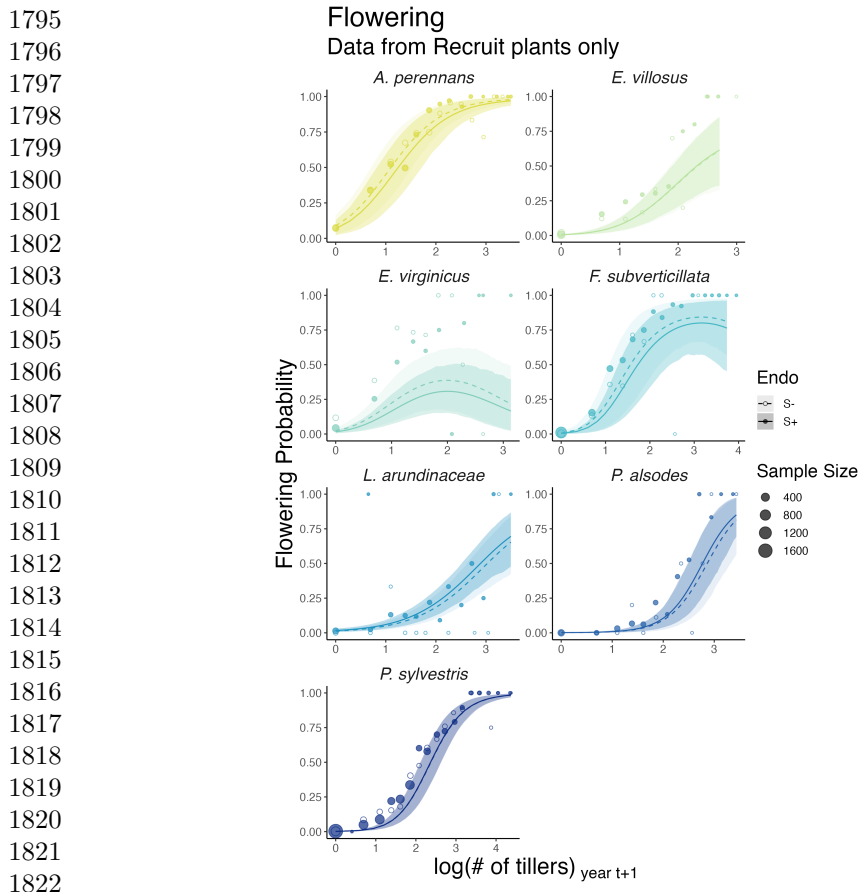


Figure S6: Effect of endophyte symbiosis on mean flowering. Fitted curves represent the size-specific mean flowering probability for originally transplanted plants along with data binned by size and averaged over many individuals, years, and plots shown as open circles with a dashed line for symbiont-free (S-) plants, while the solid line and filled circles represent symbiotic (S+) plants. 80% credible intervals are shown with dark shading for S+, or light shading for S-.



1823 Figure S7: Effect of endophyte symbiosis on mean flowering. Fitted curves represent  
 1824 the size-specific mean flowering probability for recruited plants along with data binned  
 1825 by size and averaged over many individuals, years, and plots shown as open circles  
 1826 with a dashed line for symbiont-free (S-) plants, while the solid line and filled circles  
 1827 represent symbiotic (S+) plants. 80% credible intervals are shown with dark shading  
 1828 for S+, or light shading for S-.

1829  
1830  
1831  
1832  
1833  
1834  
1835  
1836  
1837  
1838  
1839  
1840

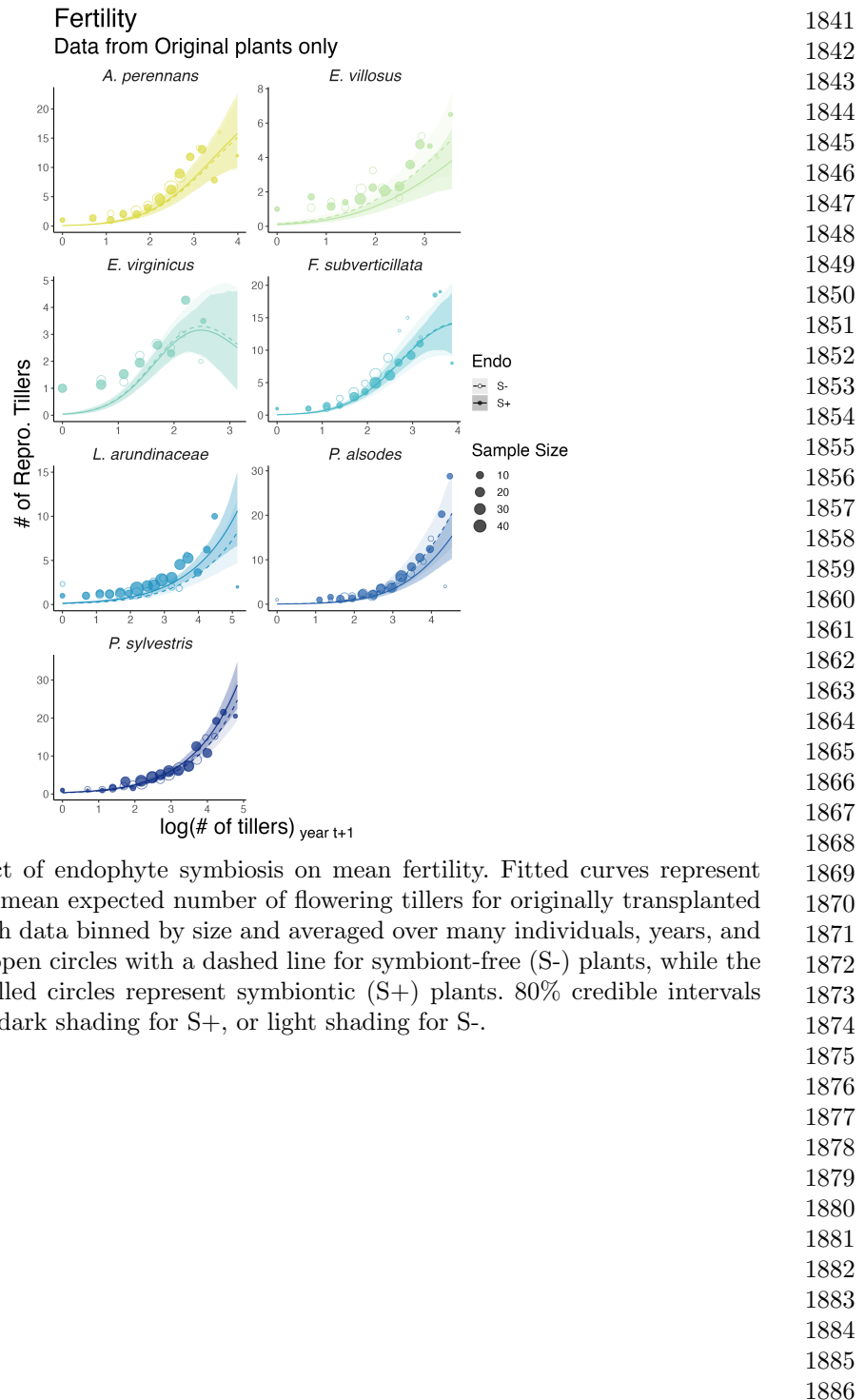


Figure S8: Effect of endophyte symbiosis on mean fertility. Fitted curves represent the size-specific mean expected number of flowering tillers for originally transplanted plants along with data binned by size and averaged over many individuals, years, and plots shown as open circles with a dashed line for symbiont-free (S-) plants, while the solid line and filled circles represent symbiotic (S+) plants. 80% credible intervals are shown with dark shading for S+, or light shading for S-.

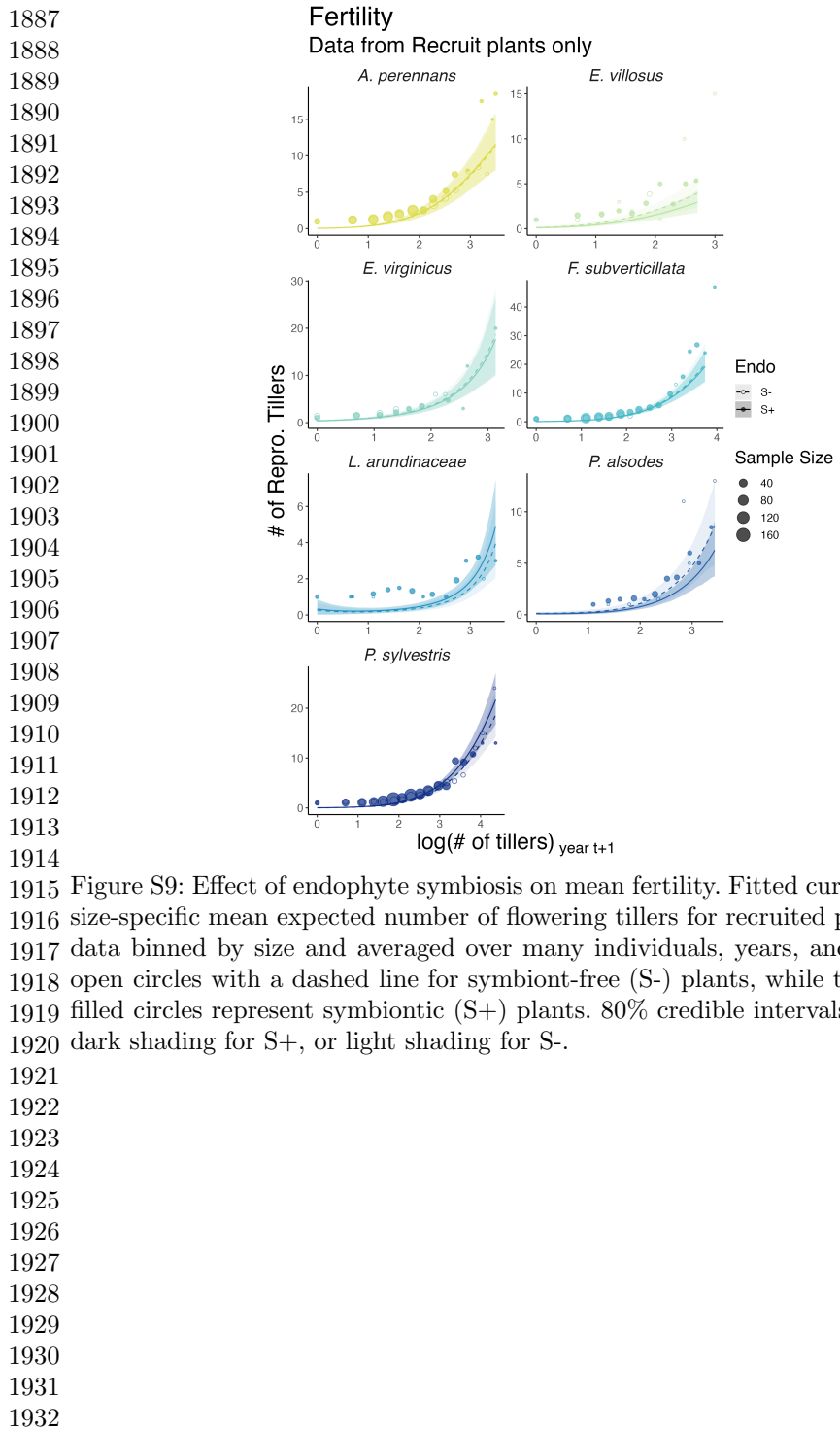


Figure S9: Effect of endophyte symbiosis on mean fertility. Fitted curves represent the size-specific mean expected number of flowering tillers for recruited plants along with data binned by size and averaged over many individuals, years, and plots shown as open circles with a dashed line for symbiont-free (S-) plants, while the solid line and filled circles represent symbiotic (S+) plants. 80% credible intervals are shown with dark shading for S+, or light shading for S-.

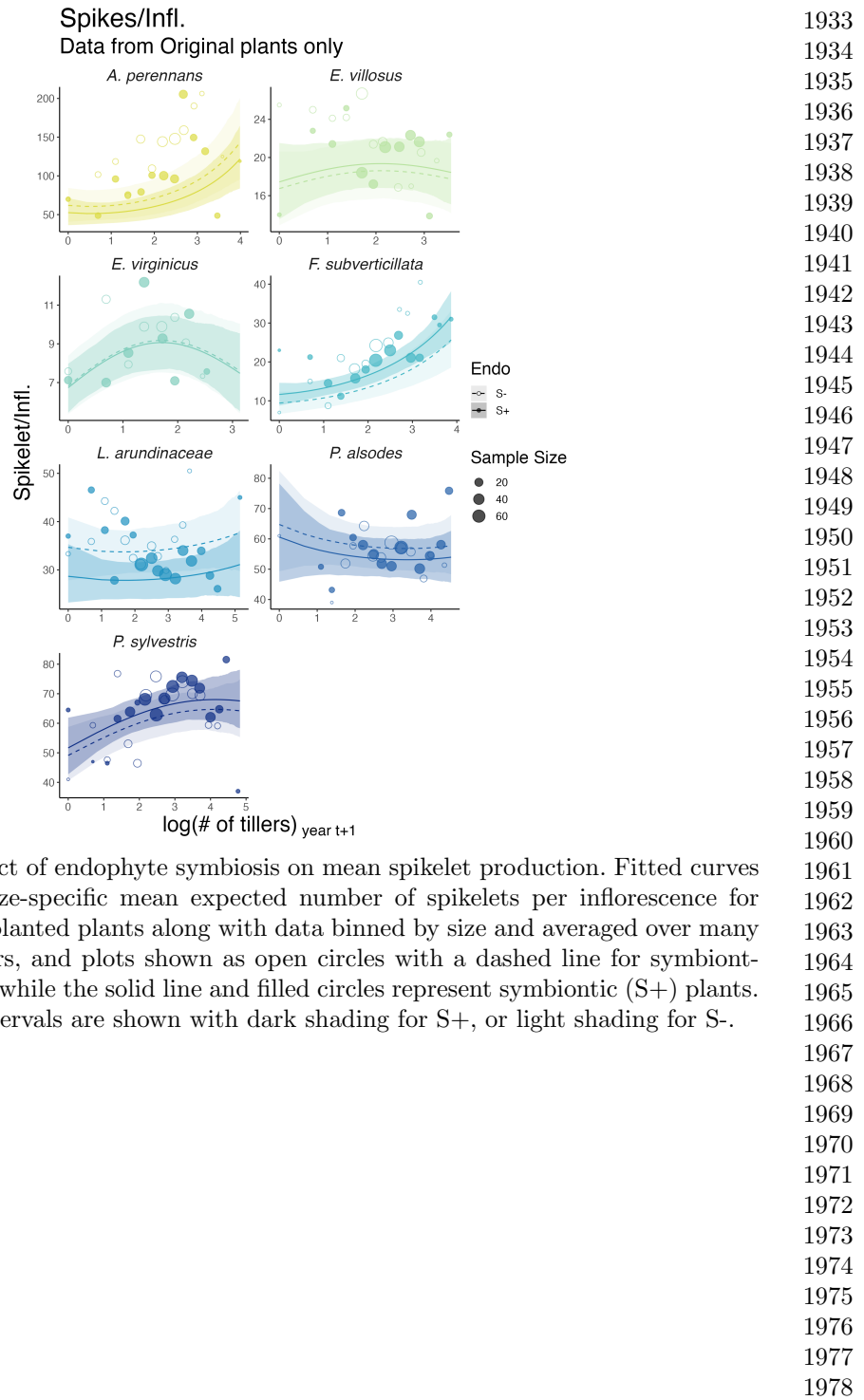
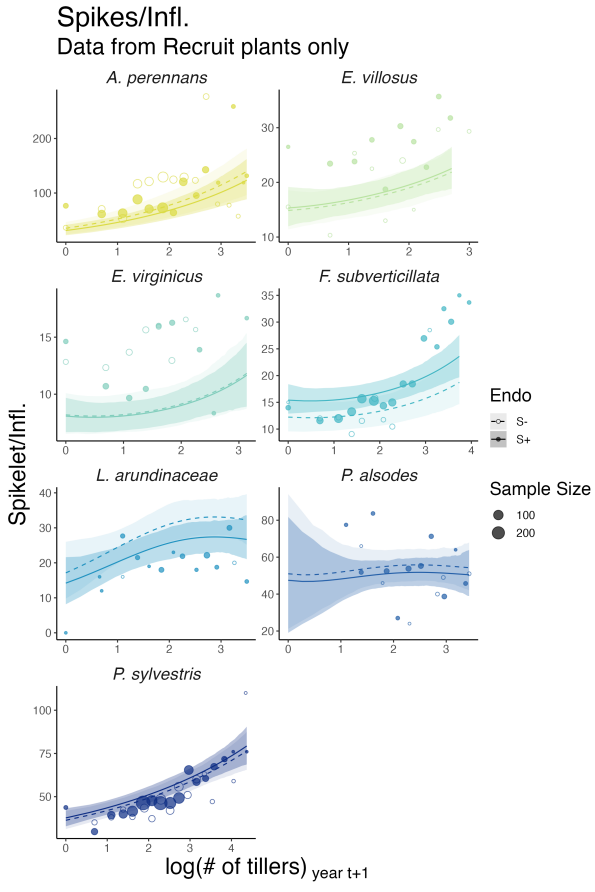


Figure S10: Effect of endophyte symbiosis on mean spikelet production. Fitted curves represent the size-specific mean expected number of spikelets per inflorescence for originally transplanted plants along with data binned by size and averaged over many individuals, years, and plots shown as open circles with a dashed line for symbiont-free (S-) plants, while the solid line and filled circles represent symbiotic (S+) plants. 80% credible intervals are shown with dark shading for S+, or light shading for S-.

1979  
 1980  
 1981  
 1982  
 1983  
 1984  
 1985  
 1986  
 1987  
 1988  
 1989  
 1990  
 1991  
 1992  
 1993  
 1994  
 1995  
 1996  
 1997  
 1998  
 1999  
 2000  
 2001  
 2002  
 2003  
 2004  
 2005  
 2006  
 2007  
 2008  
 2009  
 2010  
 2011  
 2012  
 2013  
 2014  
 2015  
 2016  
 2017  
 2018  
 2019  
 2020  
 2021  
 2022  
 2023  
 2024



2007 Figure S11: Effect of endophyte symbiosis on mean spikelet production. Fitted curves  
 2008 represent the size-specific mean expected number of spikelets per inflorescence for  
 2009 recruited plants along with data binned by size and averaged over many individuals,  
 2010 years, and plots shown as open circles with a dashed line for symbiont-free (S-) plants,  
 2011 while the solid line and filled circles represent symbiotic (S+) plants. 80% credible  
 2012 intervals are shown with dark shading for S+, or light shading for S-.

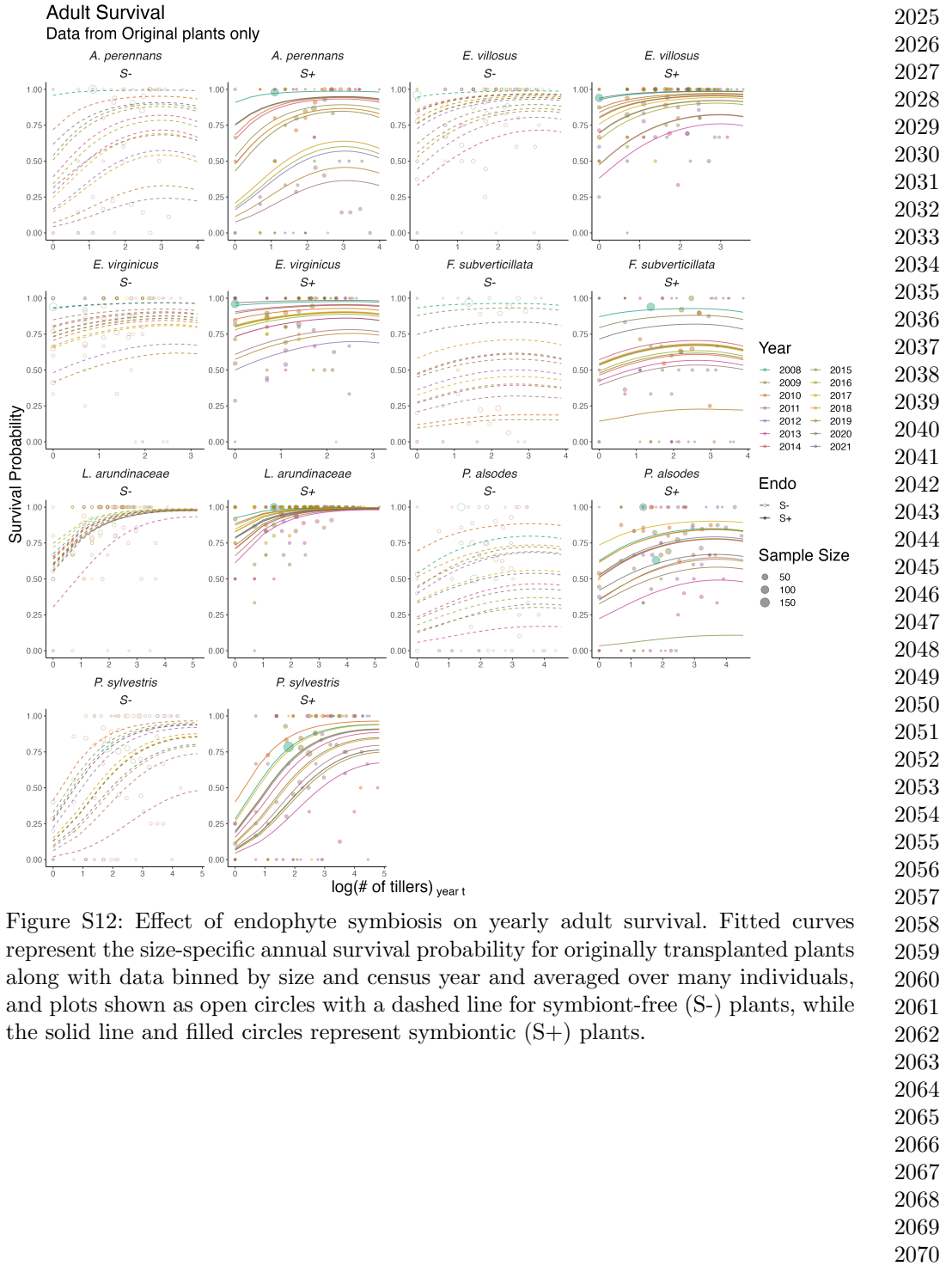
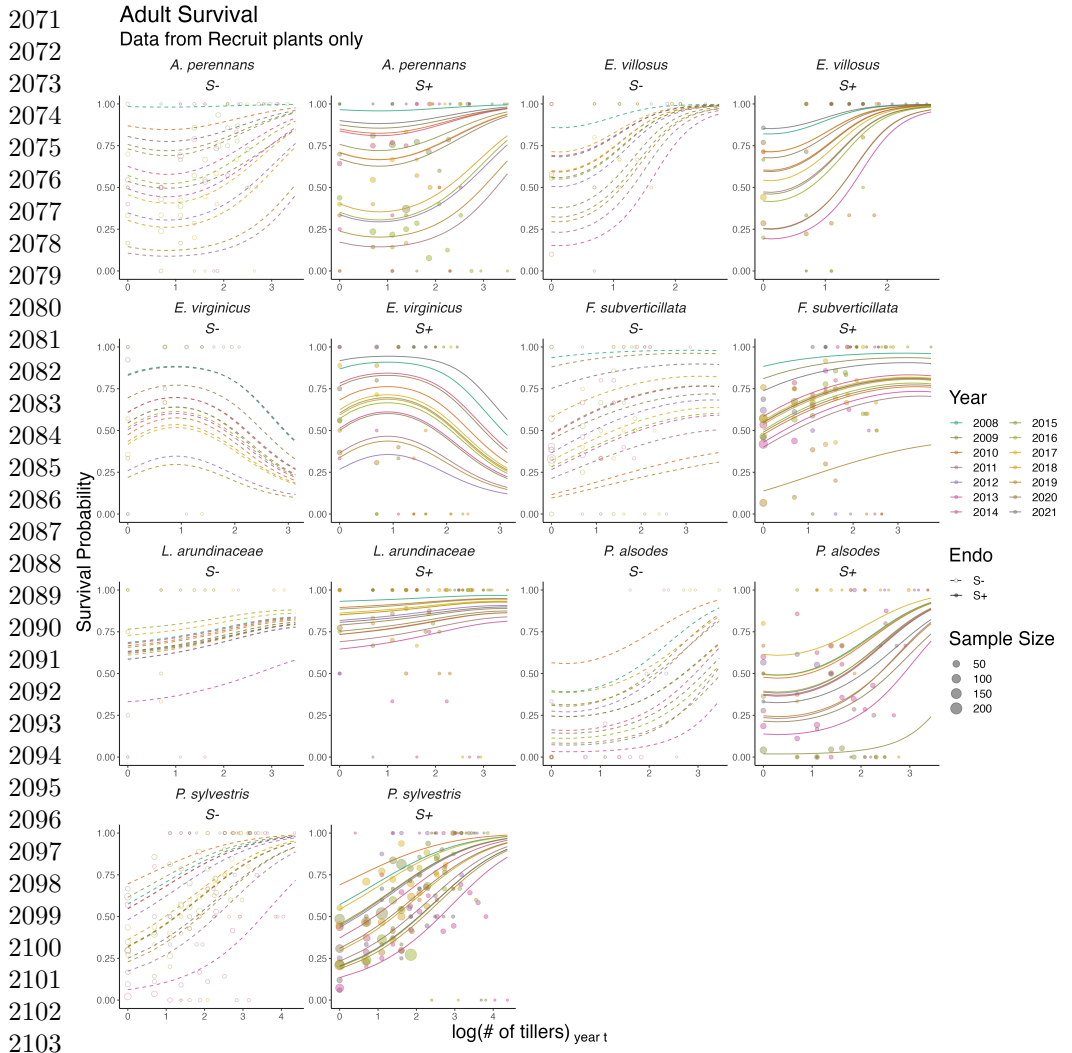


Figure S12: Effect of endophyte symbiosis on yearly adult survival. Fitted curves represent the size-specific annual survival probability for originally transplanted plants along with data binned by size and census year and averaged over many individuals, and plots shown as open circles with a dashed line for symbiont-free (S-) plants, while the solid line and filled circles represent symbiotic (S+) plants.



2104 Figure S13: Effect of endophyte symbiosis on yearly adult survival. Fitted curves  
2105 represent the size-specific annual survival probability for recruited plants along with  
2106 data binned by size and census year and averaged over many individuals, and plots  
2107 shown as open circles with a dashed line for symbiont-free (S-) plants, while the solid  
2108 line and filled circles represent symbiotic (S+) plants.

2109  
2110  
2111  
2112  
2113  
2114  
2115  
2116

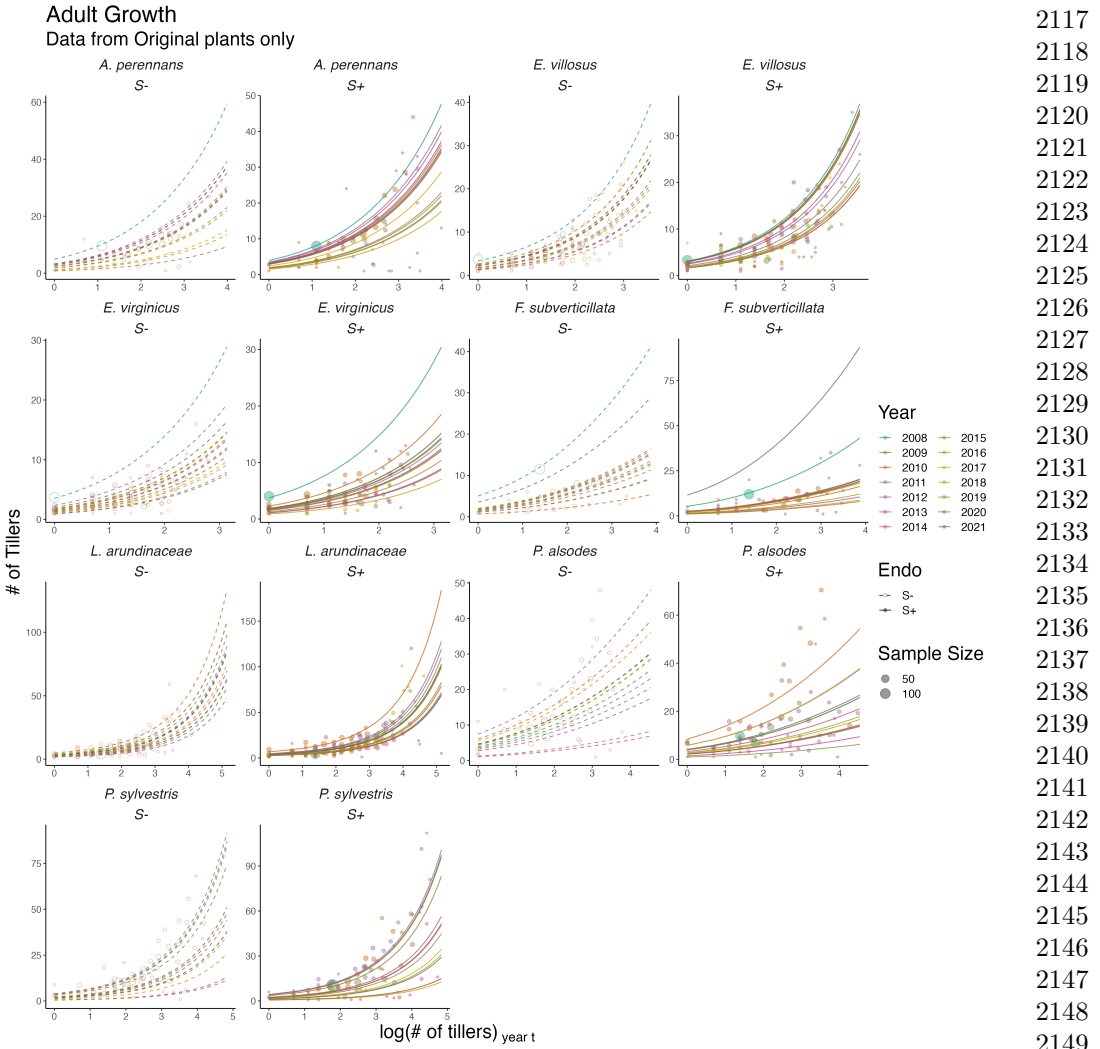
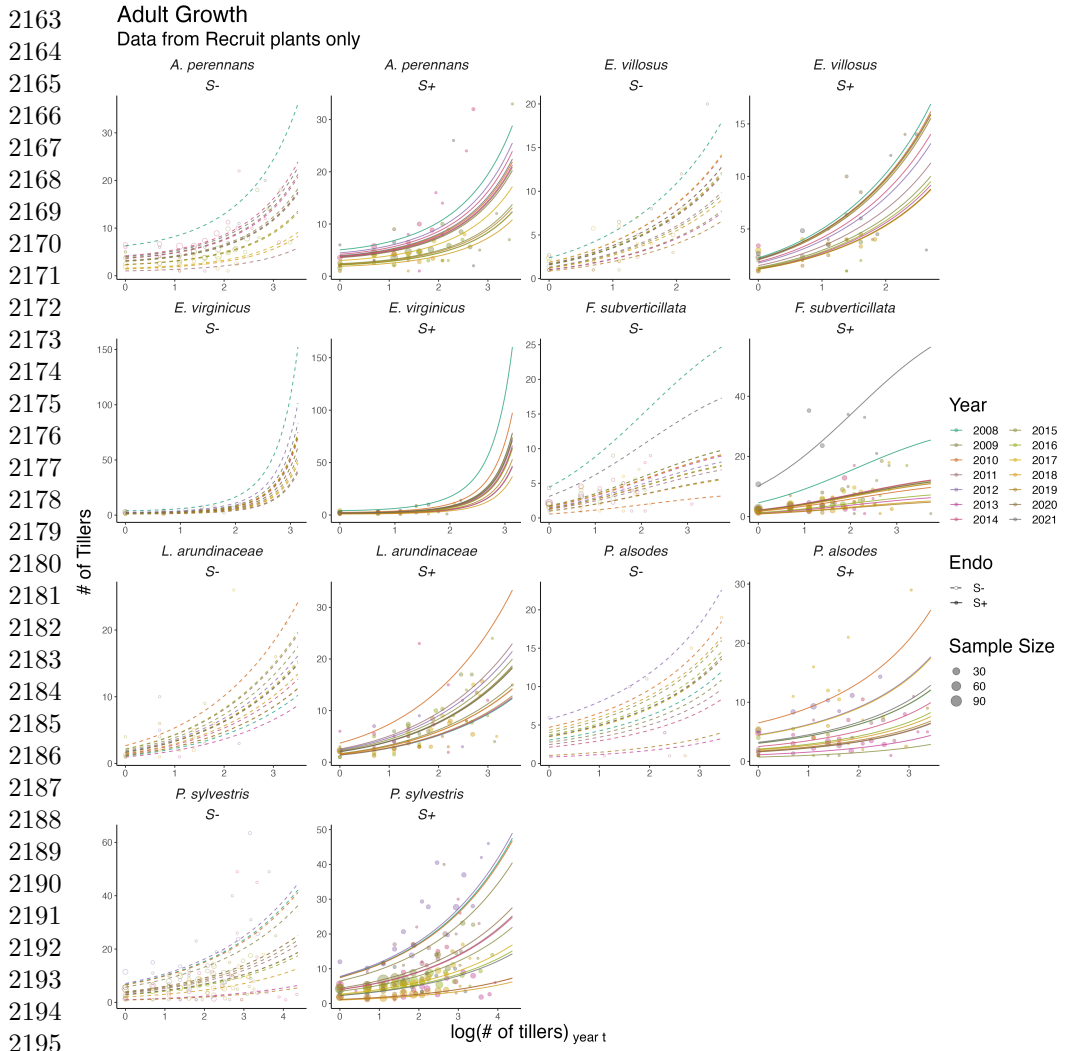


Figure S14: Effect of endophyte symbiosis on yearly adult growth. Fitted curves represent the size-specific annual expected plant size for originally transplanted plants along with data binned by size and census year and averaged over many individuals, and plots shown as open circles with a dashed line for symbiont-free (S-) plants, while the solid line and filled circles represent symbiotic (S+) plants.



2195      Figure S15: Effect of endophyte symbiosis on yearly adult growth. Fitted curves rep-  
2196 resent the size-specific annual expected plant size for recruited plants along with data  
2197 binned by size and census year and averaged over many individuals, and plots shown  
2198 as open circles with a dashed line for symbiont-free (S-) plants, while the solid line  
2199 and filled circles represent symbiotic (S+) plants.

2201  
2202  
2203  
2204  
2205  
2206  
2207  
2208

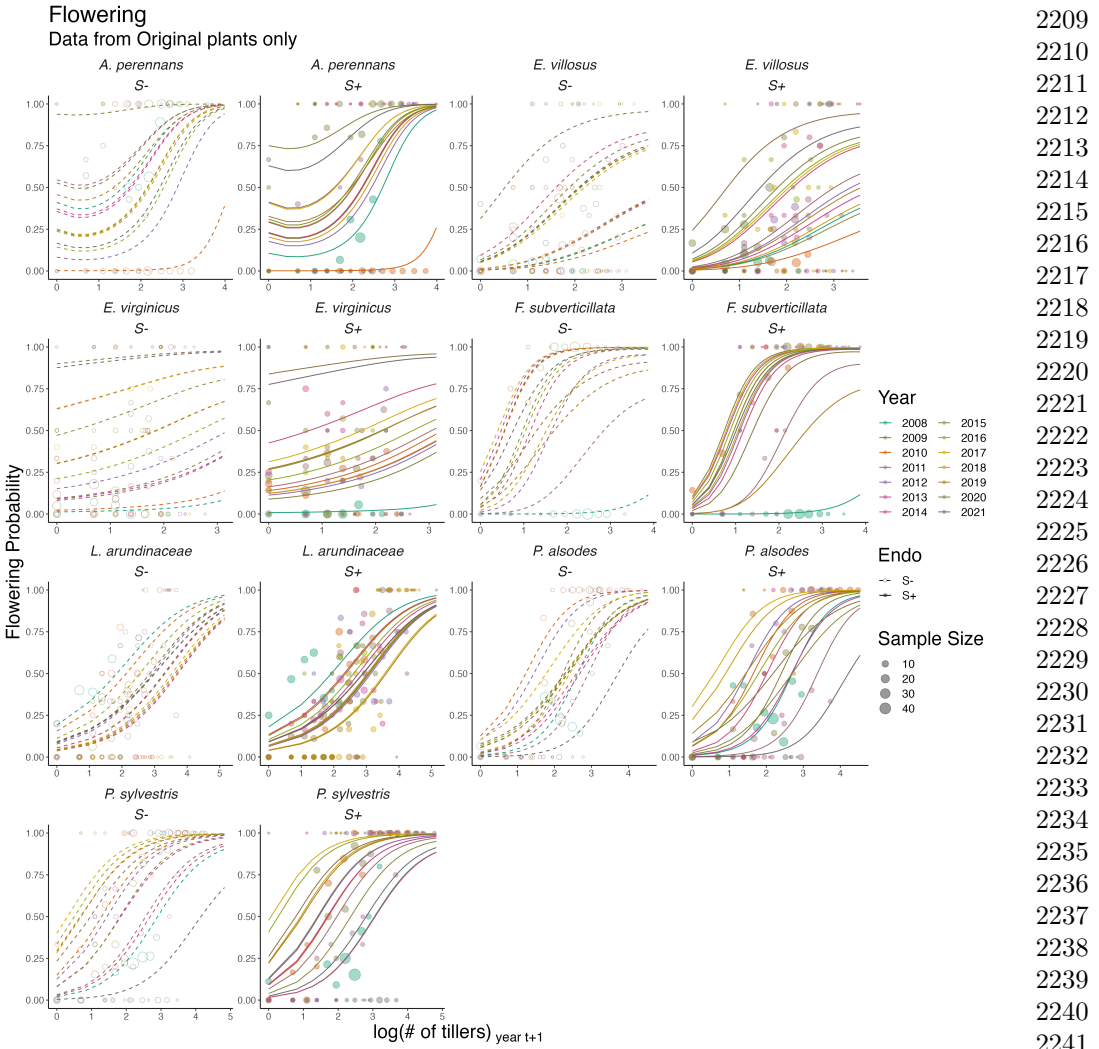
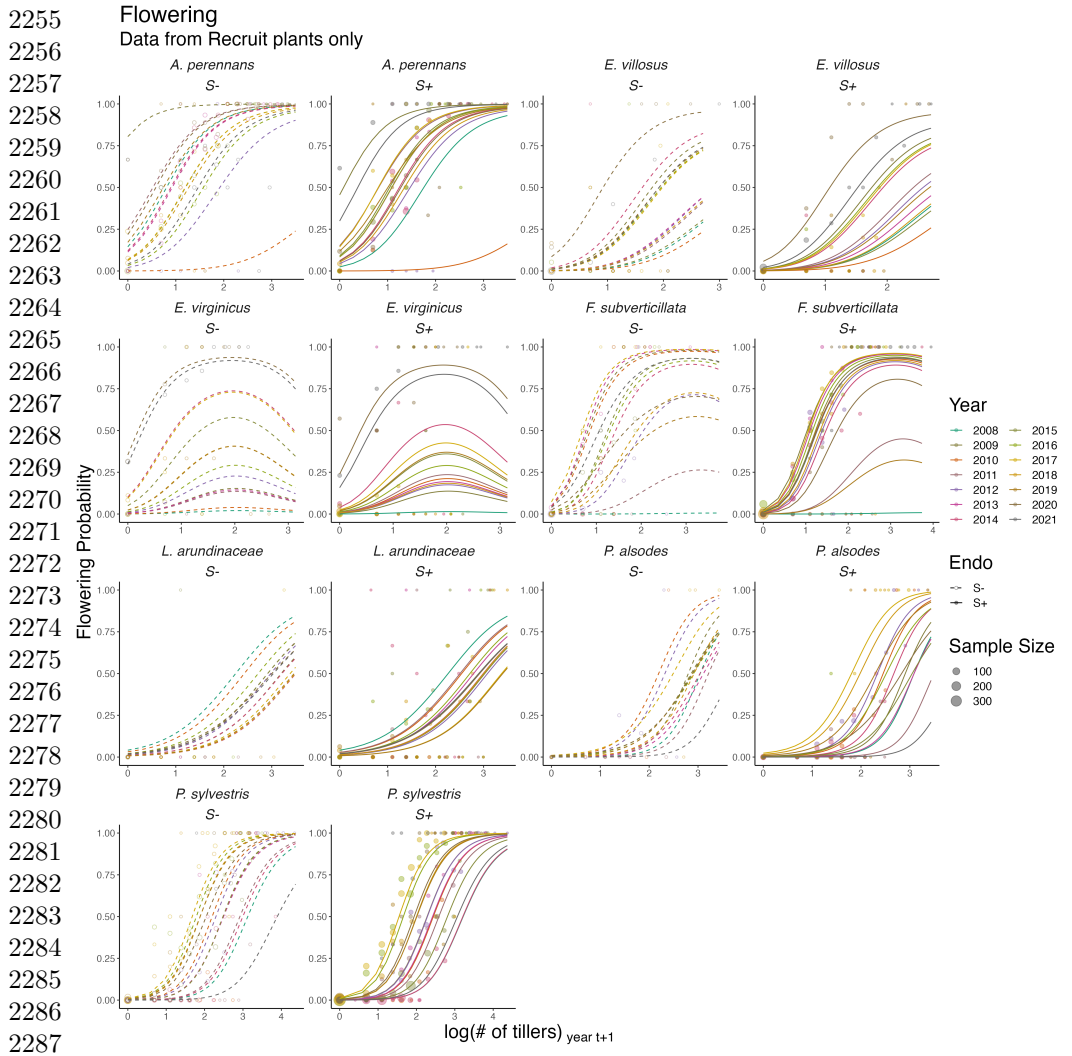


Figure S16: Effect of endophyte symbiosis on yearly flowering. Fitted curves represent the size-specific annual flowering probability for originally transplanted plants along with data binned by size and census year and averaged over many individuals, and plots shown as open circles with a dashed line for symbiont-free (S-) plants, while the solid line and filled circles represent symbiotic (S+) plants.

2209  
2210  
2211  
2212  
2213  
2214  
2215  
2216  
2217  
2218  
2219  
2220  
2221  
2222  
2223  
2224  
2225  
2226  
2227  
2228  
2229  
2230  
2231  
2232  
2233  
2234  
2235  
2236  
2237  
2238  
2239  
2240  
2241  
2242  
2243  
2244  
2245  
2246  
2247  
2248  
2249  
2250  
2251  
2252  
2253  
2254



2288 Figure S17: Effect of endophyte symbiosis on yearly flowering. Fitted curves represent the size-specific annual flowering probability for recruited plants along with data binned by size and census year and averaged over many individuals, and plots shown as open circles with a dashed line for symbiont-free (S-) plants, while the solid line and filled circles represent symbiotic (S+) plants.

2293  
2294  
2295  
2296  
2297  
2298  
2299  
2300

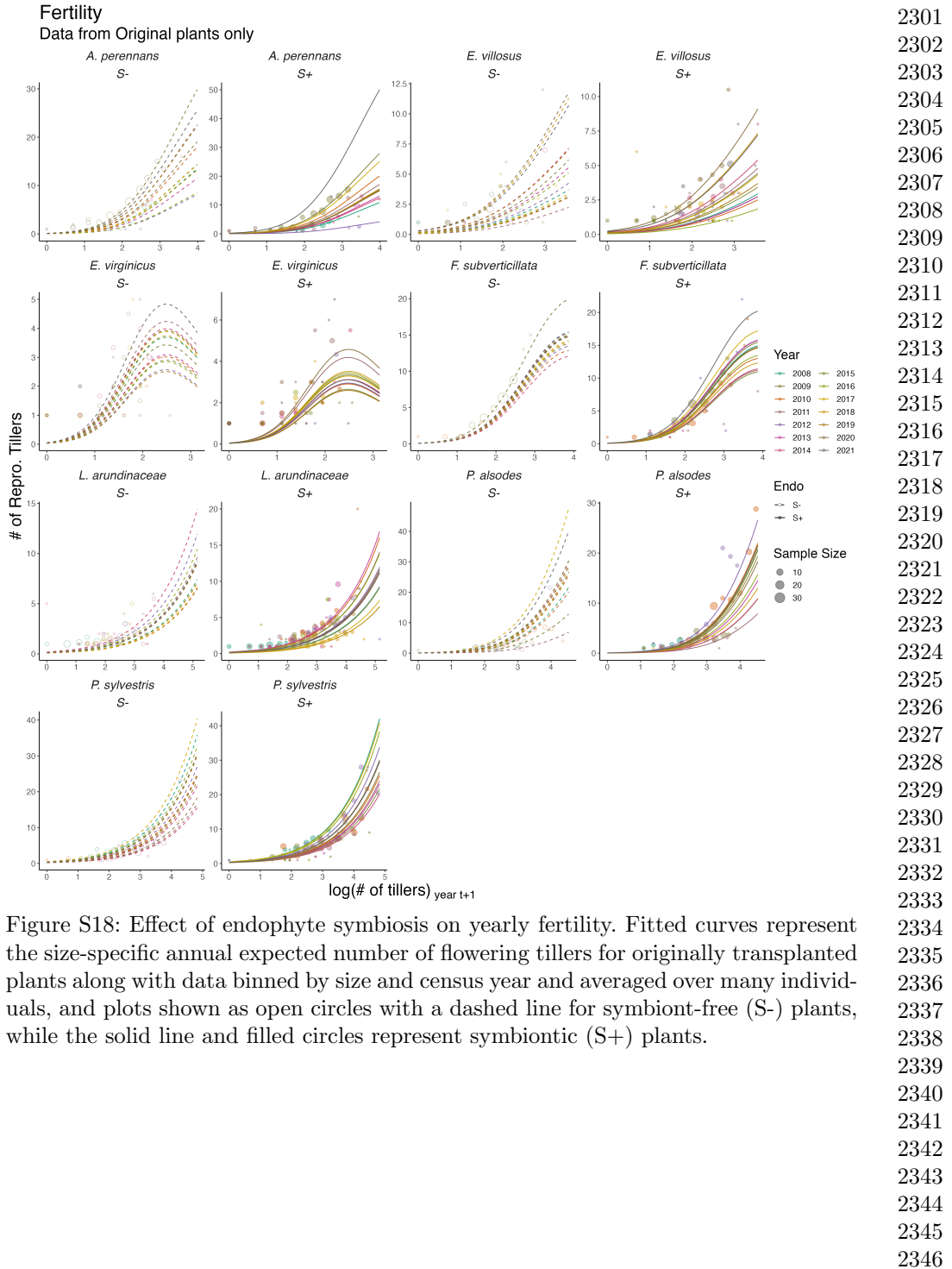
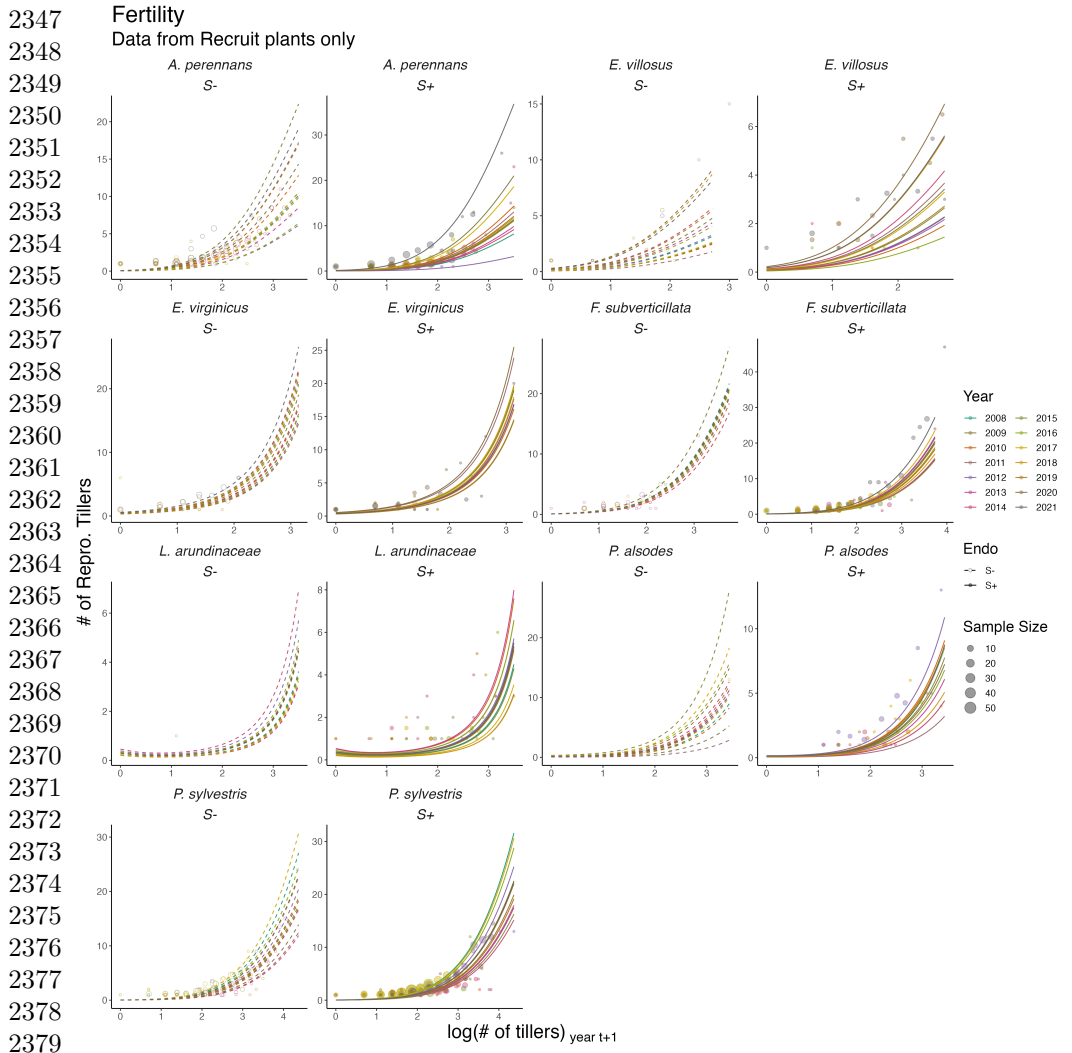


Figure S18: Effect of endophyte symbiosis on yearly fertility. Fitted curves represent the size-specific annual expected number of flowering tillers for originally transplanted plants along with data binned by size and census year and averaged over many individuals, and plots shown as open circles with a dashed line for symbiont-free (S-) plants, while the solid line and filled circles represent symbiotic (S+) plants.



2380 Figure S19: Effect of endophyte symbiosis on yearly fertility. Fitted curves represent  
 2381 the size-specific annual expected number of flowering tillers for recruited plants along  
 2382 with data binned by size and census year and averaged over many individuals, and  
 2383 plots shown as open circles with a dashed line for symbiont-free (S-) plants, while the  
 2384 solid line and filled circles represent symbiotic (S+) plants.

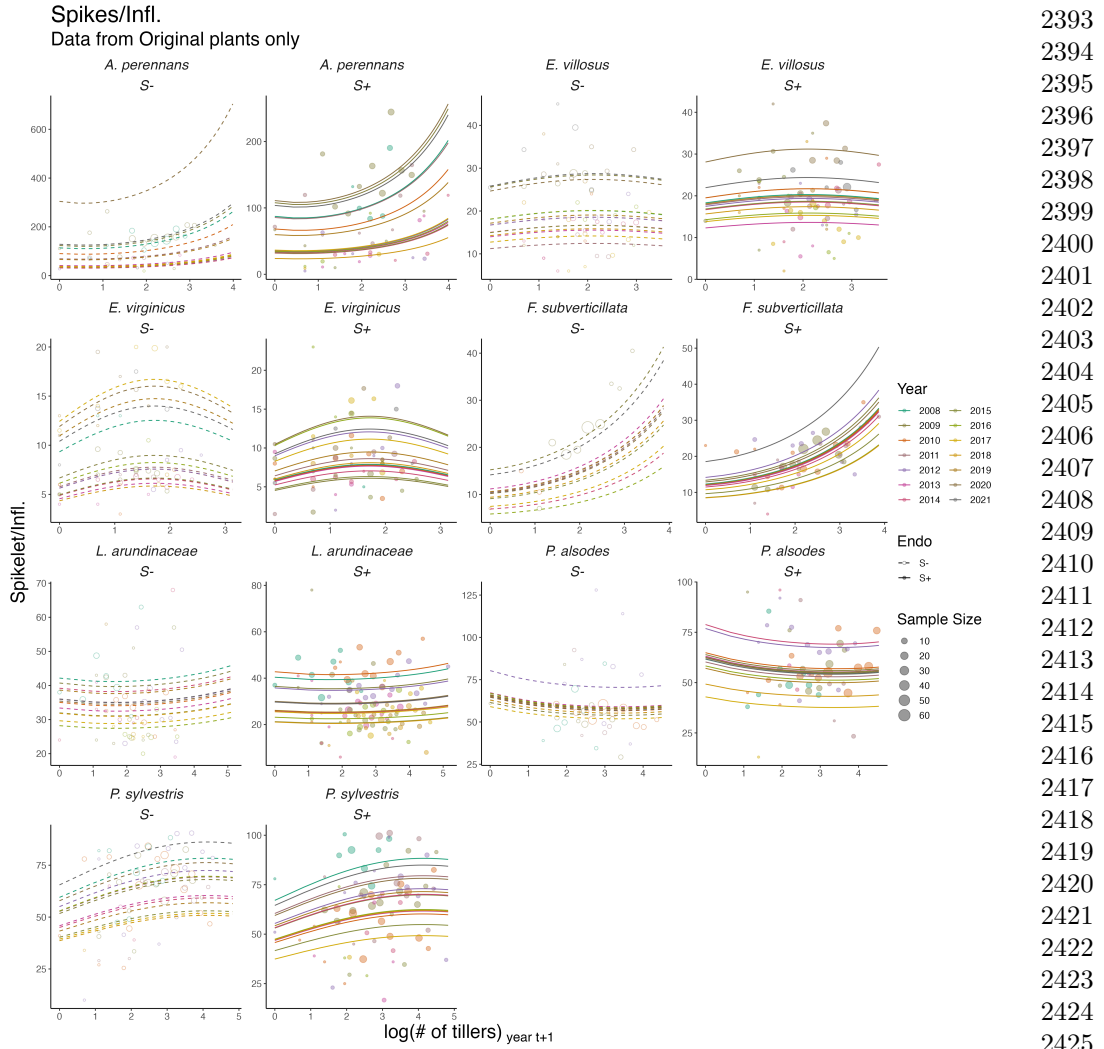
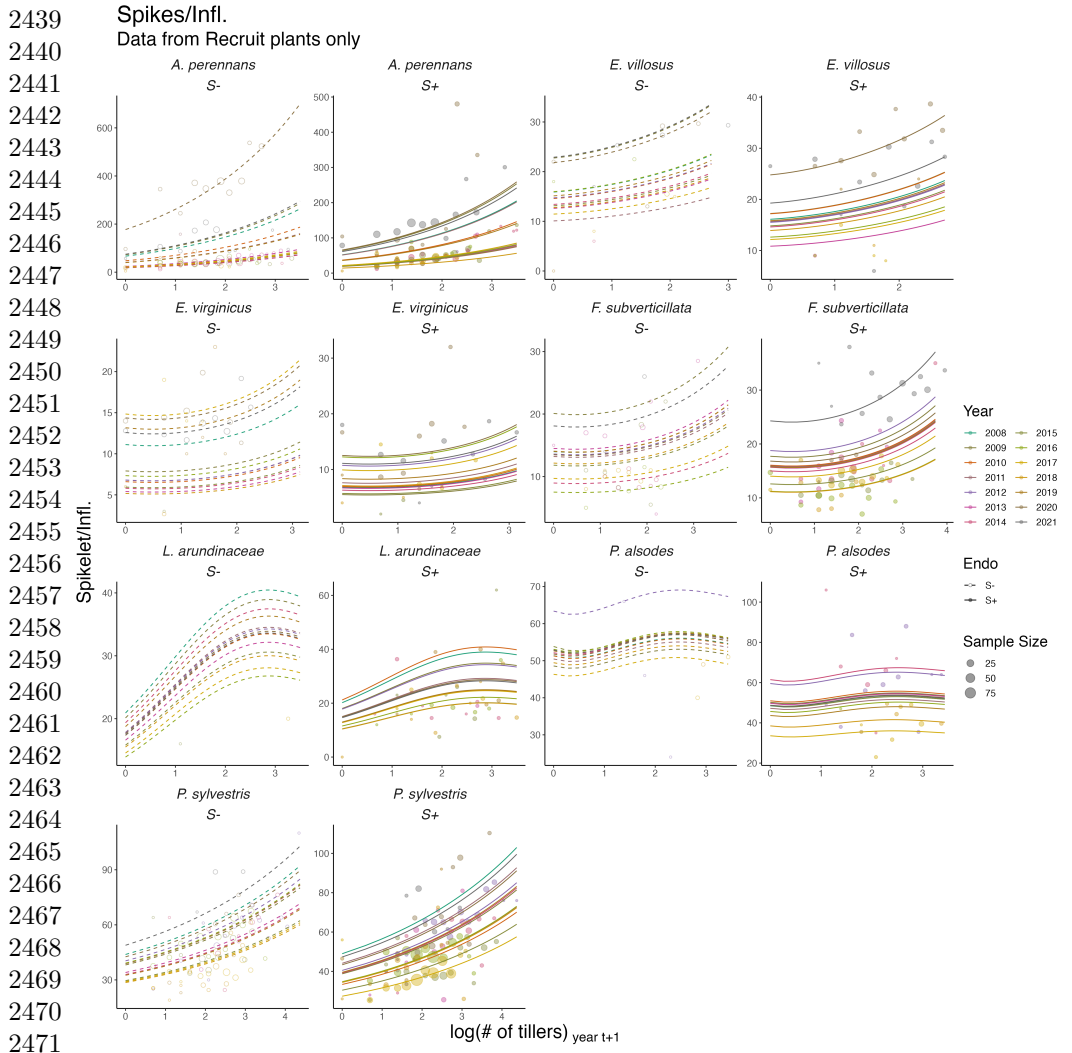


Figure S20: Effect of endophyte symbiosis on yearly spikelet production. Fitted curves represent the size-specific annual expected number of spikelets per inflorescence for originally transplanted plants along with data binned by size and census year and averaged over many individuals, and plots shown as open circles with a dashed line for symbiont-free (S-) plants, while the solid line and filled circles represent symbiotic (S+) plants.



2472 Figure S21: Effect of endophyte symbiosis on yearly spikelet production. Fitted curves  
2473 represent the size-specific annual expected number of spikelets per inflorescence for  
2474 recruited plants along with data binned by size and census year and averaged over  
2475 many individuals, and plots shown as open circles with a dashed line for symbiont-free  
2476 (S-) plants, while the solid line and filled circles represent symbiotic (S+) plants.

2477  
2478  
2479  
2480  
2481  
2482  
2483  
2484

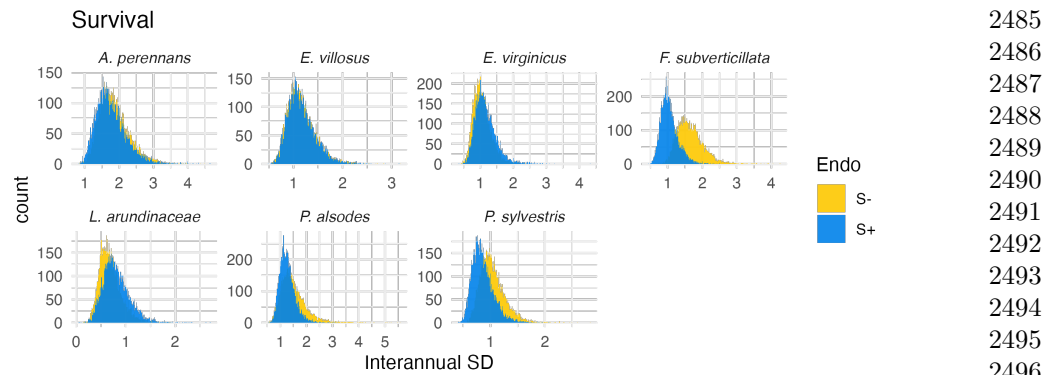


Figure S22: Posterior distributions of the standard deviations of inter-annual year effects for survival. Histograms include 7500 post-warmup MCMC samples for symbiotic (S+; blue) and symbiont-free (S-; tan) plants from fitted vital rate model.

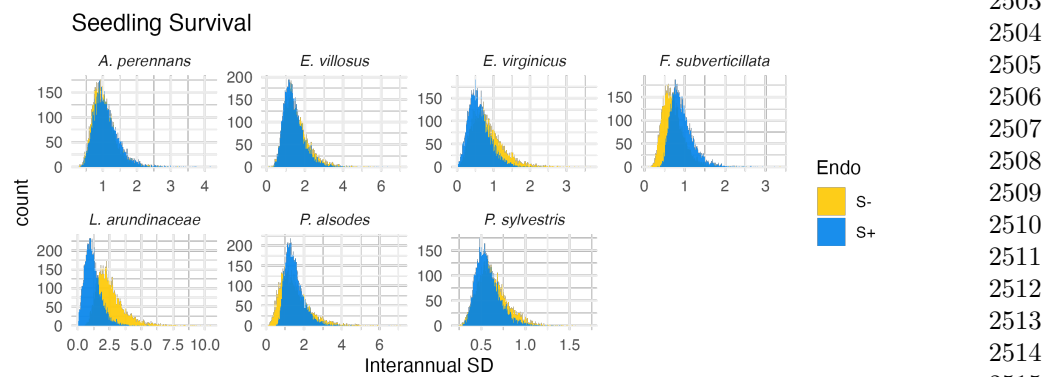
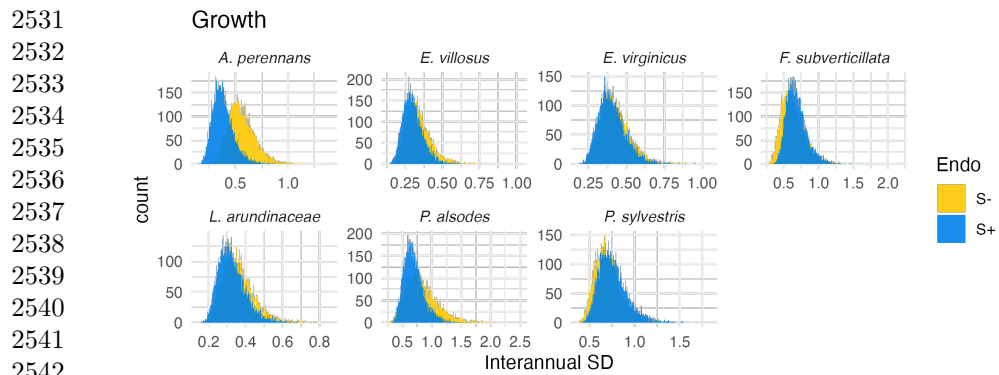
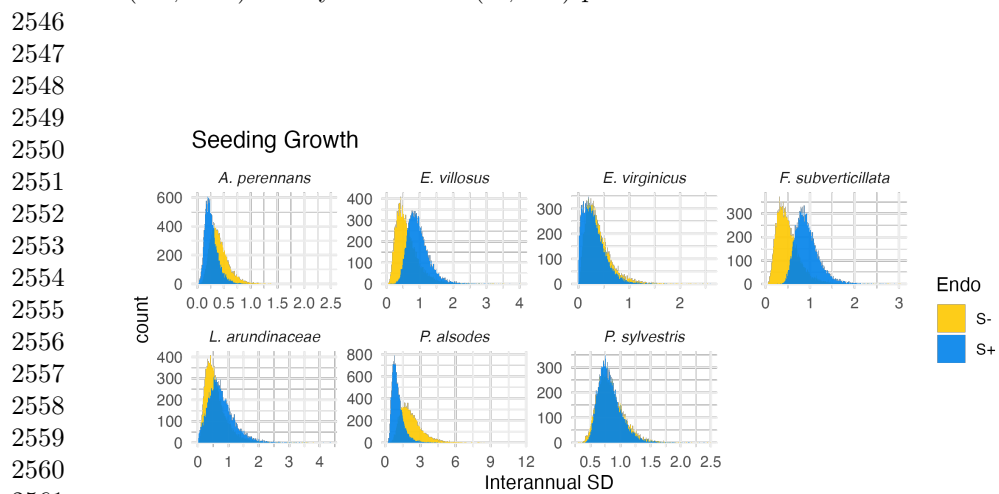


Figure S23: Posterior distributions of the standard deviations of inter-annual year effects for seedling survival. Histograms include 7500 post-warmup MCMC samples for symbiotic (S+; blue) and symbiont-free (S-; tan) plants from fitted vital rate model.



2543 Figure S24: Posterior distributions of the standard deviations of inter-annual year  
 2544 effects for growth. Histograms include 7500 post-warmup MCMC samples for symbi-  
 2545 otic (S+; blue) and symbiont-free (S-; tan) plants from fitted vital rate model.



2561 Figure S25: Posterior distributions of the standard deviations of inter-annual year  
 2562 effects for seedling growth. Histograms include 7500 post-warmup MCMC samples for  
 2563 symbiotic (S+; blue) and symbiont-free (S-; tan) plants from fitted vital rate model.

2565

2566

2567

2568

2569

2570

2571

2572

2573

2574

2575

2576

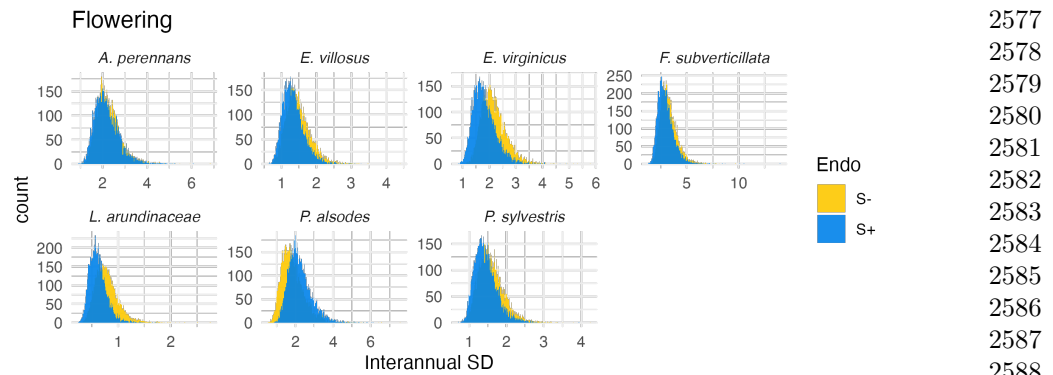


Figure S26: Posterior distributions of the standard deviations of inter-annual year effects for flowering probability. Histograms include 7500 post-warmup MCMC samples for symbiotic (S+; blue) and symbiont-free (S-; tan) plants from fitted vital rate model.

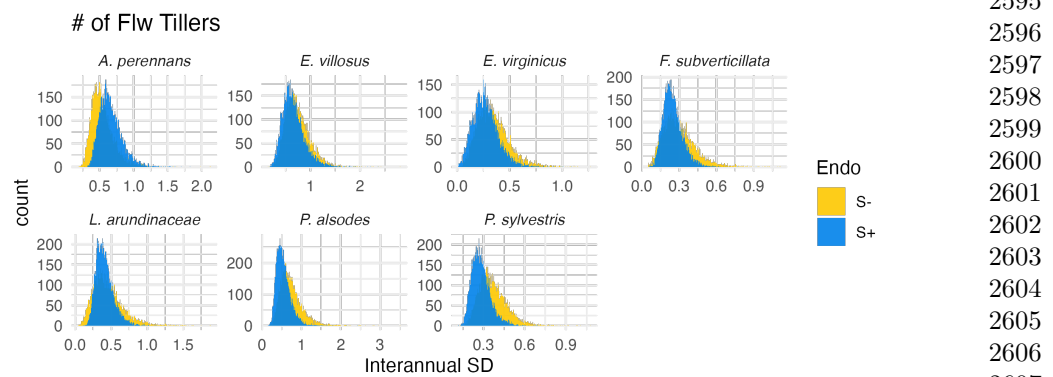
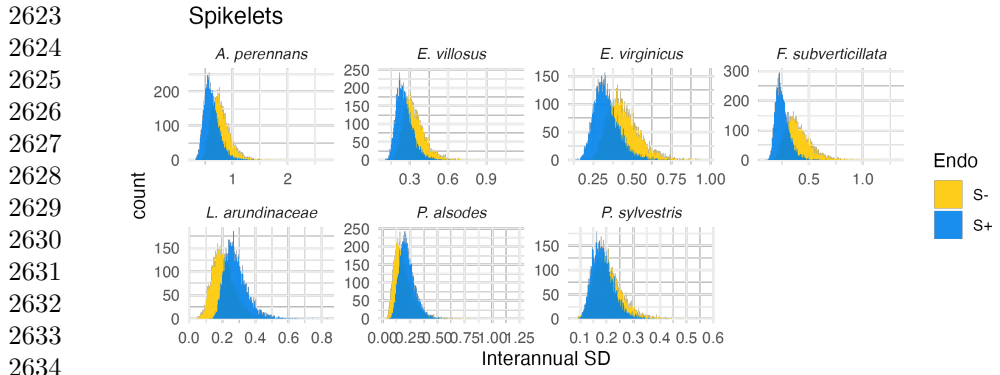
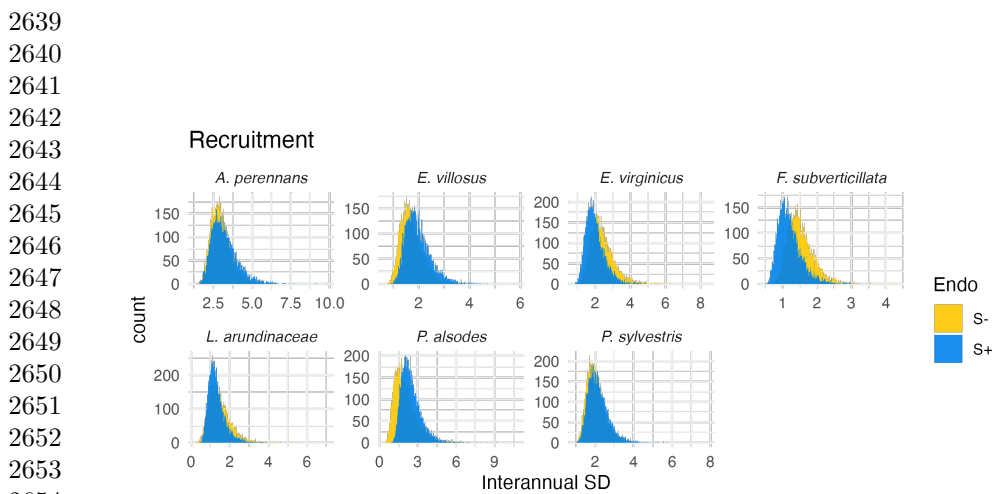


Figure S27: Posterior distributions of the standard deviations of inter-annual year effects for fertility (no. of flowering tillers). Histograms include 7500 post-warmup MCMC samples for symbiotic (S+; blue) and symbiont-free (S-; tan) plants from fitted vital rate model.



2635 Figure S28: Posterior distributions of the standard deviations of inter-annual year  
 2636 effects for spikelets per inflorescence. Histograms include 7500 post-warmup MCMC  
 2637 samples for symbiotic (S+; blue) and symbiont-free (S-; tan) plants from fitted vital  
 2638 rate model.



2654 Figure S29: Posterior distributions of the standard deviations of inter-annual year  
 2655 effects for recruitment. Histograms include 7500 post-warmup MCMC samples for  
 2656 symbiotic (S+; blue) and symbiont-free (S-; tan) plants from fitted vital rate model.  
 2657

2658  
2659  
2660  
2661  
2662  
2663  
2664  
2665  
2666  
2667  
2668

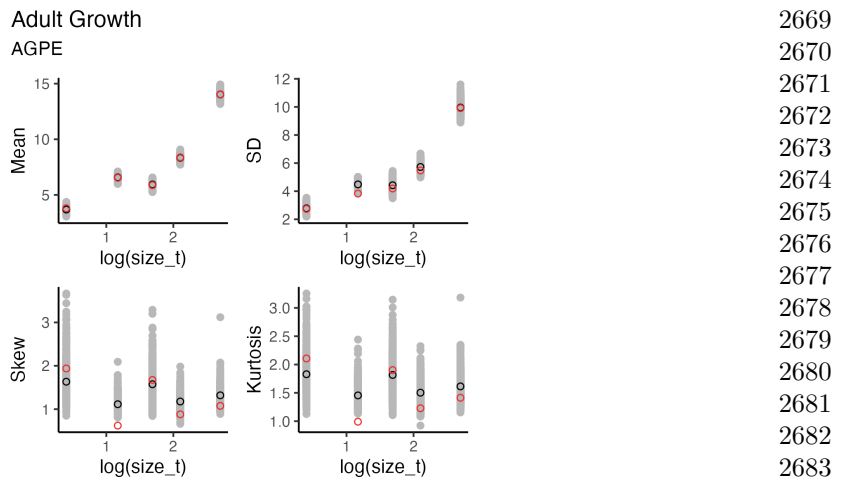


Figure S30: Graphical posterior predictive check for mean and higher moments of *A. perennans* growth model across size. Consistency between real data and fitted values across sizes indicates that the vital rate models are accurately capturing size dependence. Points show the value of statistical moments binned across size for the observed data (red circles) compared to the simulated datasets (grey circles) and the median of the simulated values (black circles) generated from 500 posterior draws from the fitted model.

2715

2716

2717

2718

2719

2720

2721

2722

2723

2724

2725

2726

2727

2728

2729

2730

2731

2732

2733

2734

2735

2736

2737

2738

2739

2740

2741

2742

2743

2744

2745

2746

2747

2748

2749

2750

2751

2752

2753

2754

2755

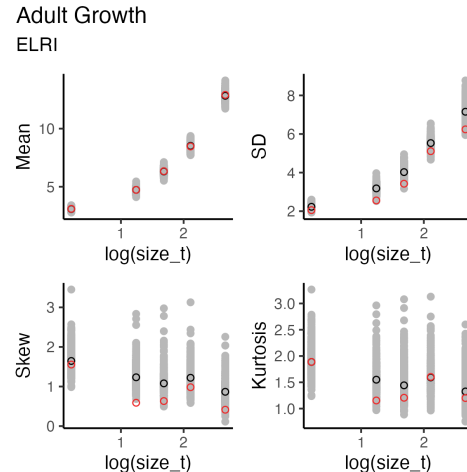
2756

2757

2758

2759

2760



2730 Figure S31: Graphical posterior predictive check for mean and higher moments of *E.*  
 2731 *villosus* growth model across size. Consistency between real data and fitted values  
 2732 across sizes indicates that the vital rate models are accurately capturing size depen-  
 2733 dence. Points show the value of statistical moments binned across size for the observed  
 2734 data (red circles) compared to the simulated datasets (grey circles) and the median  
 2735 of the simulated values (black circles) generated from 500 posterior draws from the  
 2736 fitted model.

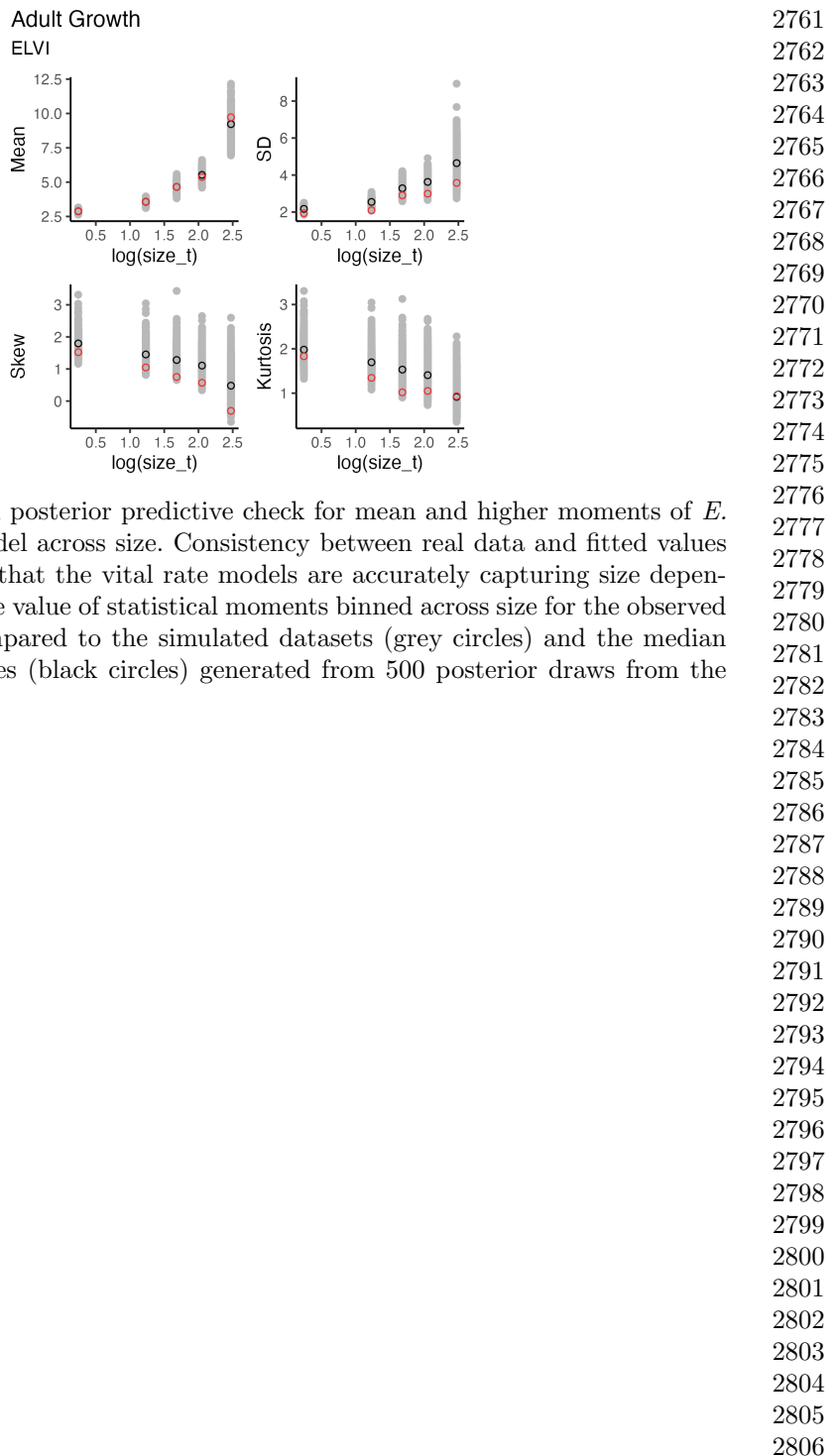


Figure S32: Graphical posterior predictive check for mean and higher moments of *E. virginicus* growth model across size. Consistency between real data and fitted values across sizes indicates that the vital rate models are accurately capturing size dependence. Points show the value of statistical moments binned across size for the observed data (red circles) compared to the simulated datasets (grey circles) and the median of the simulated values (black circles) generated from 500 posterior draws from the fitted model.

2807  
2808  
2809  
2810  
2811  
2812  
2813  
2814  
2815  
2816  
2817  
2818  
2819  
2820  
2821  
2822  
2823  
2824  
2825  
2826  
2827  
2828  
2829  
2830  
2831  
2832  
2833  
2834  
2835  
2836  
2837  
2838  
2839  
2840  
2841  
2842  
2843  
2844  
2845  
2846  
2847  
2848  
2849  
2850  
2851  
2852

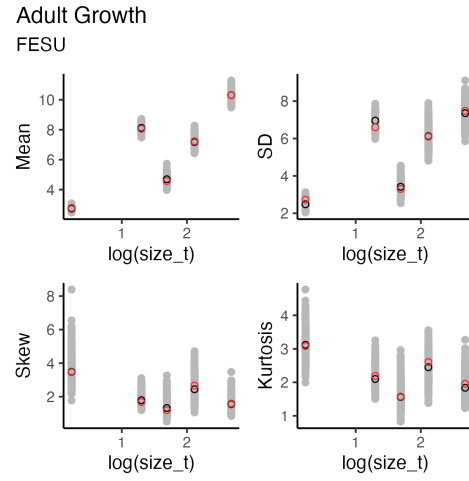
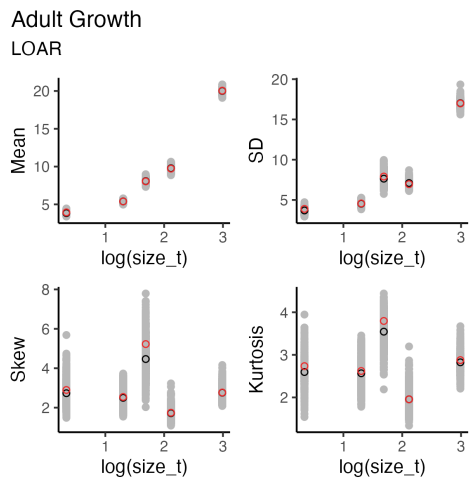


Figure S33: Graphical posterior predictive check for mean and higher moments of *F. subverticillata* growth model across size. Consistency between real data and fitted values across sizes indicates that the vital rate models are accurately capturing size dependence. Points show the value of statistical moments binned across size for the observed data (red circles) compared to the simulated datasets (grey circles) and the median of the simulated values (black circles) generated from 500 posterior draws from the fitted model.



2853  
 2854  
 2855  
 2856  
 2857  
 2858  
 2859  
 2860  
 2861  
 2862  
 2863  
 2864  
 2865  
 2866  
 2867  
 2868  
 2869  
 2870  
 2871  
 2872  
 2873  
 2874  
 2875  
 2876  
 2877  
 2878  
 2879  
 2880  
 2881  
 2882  
 2883  
 2884  
 2885  
 2886  
 2887  
 2888  
 2889  
 2890  
 2891  
 2892  
 2893  
 2894  
 2895  
 2896  
 2897  
 2898

2899

2900

2901

2902

2903

2904

2905

2906

2907

2908

2909

2910

2911

2912

2913

2914

Figure S35: Graphical posterior predictive check for mean and higher moments of *P. alsodes* growth model across size. Consistency between real data and fitted values across sizes indicates that the vital rate models are accurately capturing size dependence. Points show the value of statistical moments binned across size for the observed data (red circles) compared to the simulated datasets (grey circles) and the median of the simulated values (black circles) generated from 500 posterior draws from the fitted model.

2921

2922

2923

2924

2925

2926

2927

2928

2929

2930

2931

2932

2933

2934

2935

2936

2937

2938

2939

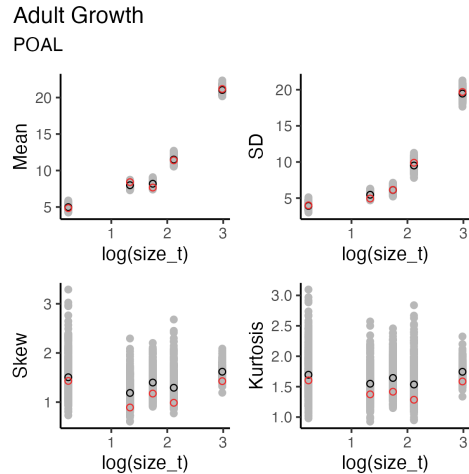
2940

2941

2942

2943

2944



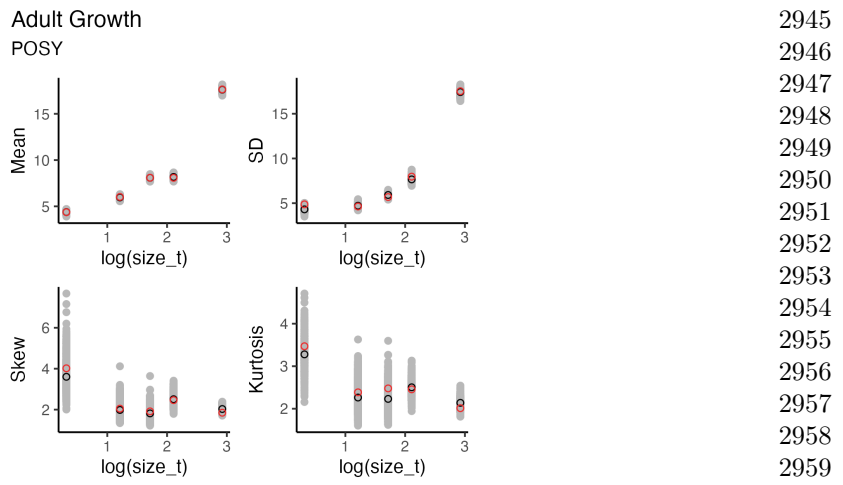


Figure S36: Graphical posterior predictive check for mean and higher moments of *P. sylvestris* growth model across size. Consistency between real data and fitted values across sizes indicates that the vital rate models are accurately capturing size dependence. Points show the value of statistical moments binned across size for the observed data (red circles) compared to the simulated datasets (grey circles) and the median of the simulated values (black circles) generated from 500 posterior draws from the fitted model.

2945  
2946  
2947  
2948  
2949  
2950  
2951  
2952  
2953  
2954  
2955  
2956  
2957  
2958  
2959  
2960  
2961  
2962  
2963  
2964  
2965  
2966  
2967  
2968  
2969  
2970  
2971  
2972  
2973  
2974  
2975  
2976  
2977  
2978  
2979  
2980  
2981  
2982  
2983  
2984  
2985  
2986  
2987  
2988  
2989  
2990

2991  
2992  
2993  
2994  
2995  
2996  
2997  
2998  
2999  
3000  
3001  
3002  
3003  
3004  
3005  
3006  
3013  
3014  
3015  
3016  
3017  
3018  
3019  
3020  
3021  
3022  
3023  
3024  
3025  
3026  
3027  
3028  
3029  
3030  
3031  
3032  
3033  
3034  
3035  
3036

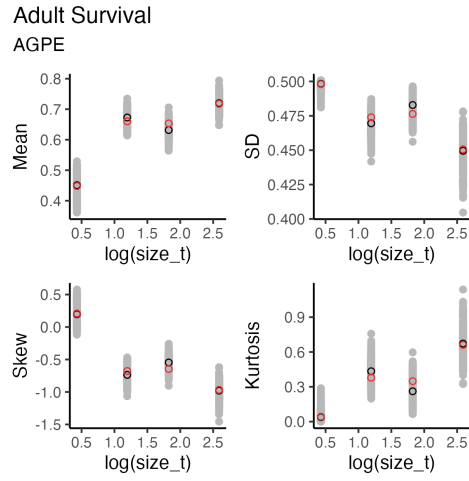


Figure S37: Graphical posterior predictive check for mean and higher moments of *A. perennans* survival model across size. Consistency between real data and fitted values across sizes indicates that the vital rate models are accurately capturing size dependence. Points show the value of statistical moments binned across size for the observed data (red circles) compared to the simulated datasets (grey circles) and the median of the simulated values (black circles) generated from 500 posterior draws from the fitted model.

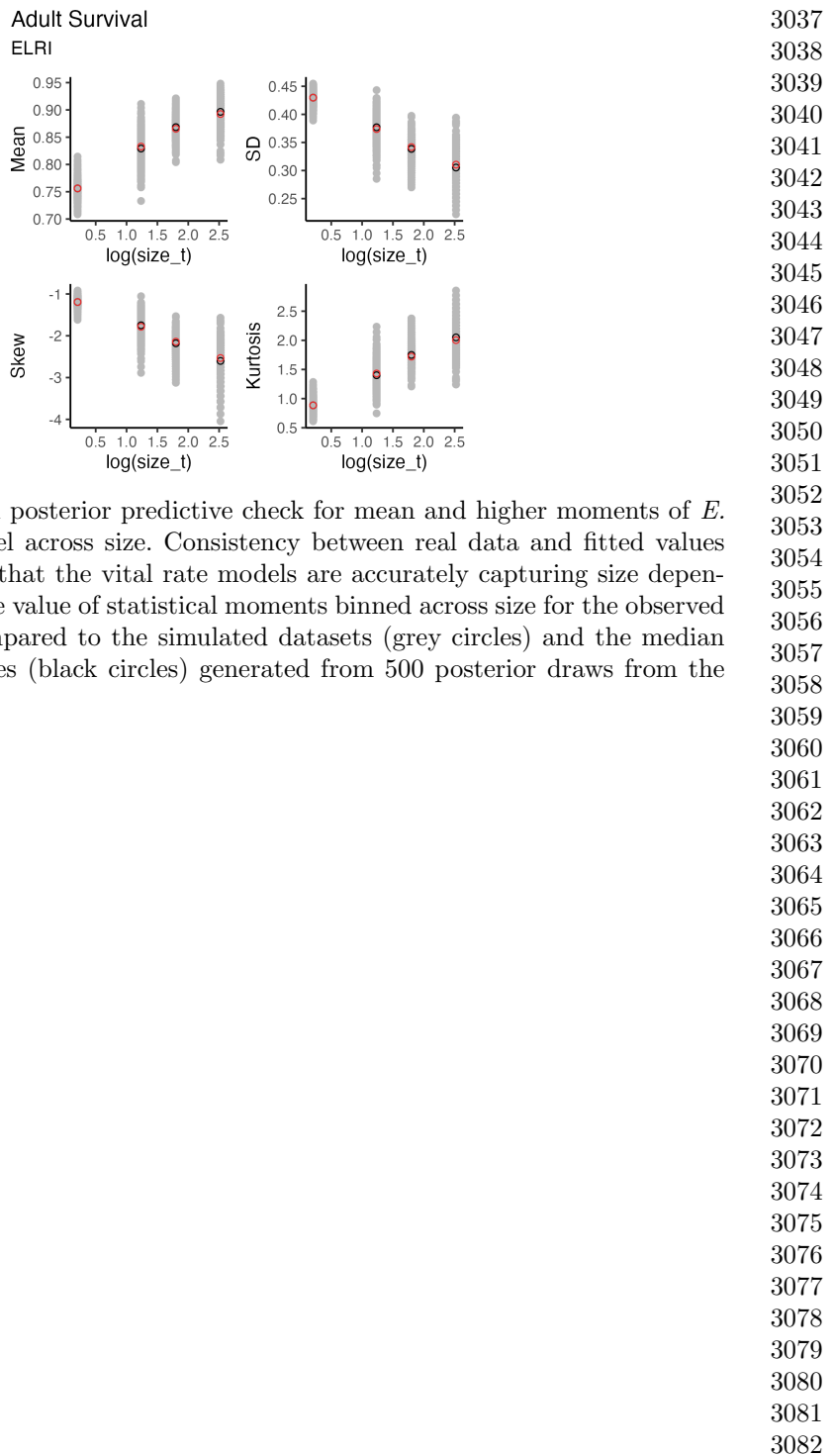


Figure S38: Graphical posterior predictive check for mean and higher moments of *E. villosus* survival model across size. Consistency between real data and fitted values across sizes indicates that the vital rate models are accurately capturing size dependence. Points show the value of statistical moments binned across size for the observed data (red circles) compared to the simulated datasets (grey circles) and the median of the simulated values (black circles) generated from 500 posterior draws from the fitted model.

3083  
3084  
3085  
3086  
3087  
3088  
3089  
3090  
3091  
3092  
3093  
3094  
3095  
3096  
3097  
3098  
3099  
3100  
3101  
3102  
3103  
3104  
3105  
3106  
3107  
3108  
3109  
3110  
3111  
3112  
3113  
3114  
3115  
3116  
3117  
3118  
3119  
3120  
3121  
3122  
3123  
3124  
3125  
3126  
3127  
3128

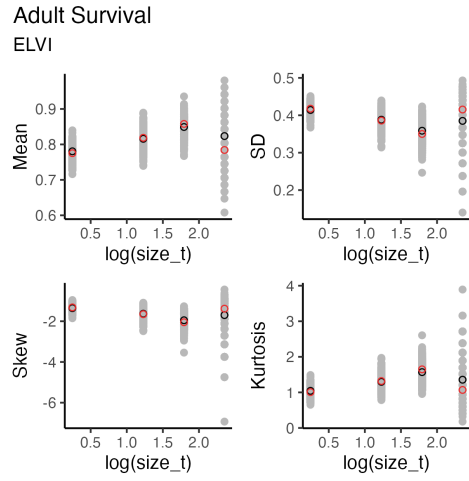


Figure S39: Graphical posterior predictive check for mean and higher moments of *E. virginicus* survival model across size. Consistency between real data and fitted values across sizes indicates that the vital rate models are accurately capturing size dependence. Points show the value of statistical moments binned across size for the observed data (red circles) compared to the simulated datasets (grey circles) and the median of the simulated values (black circles) generated from 500 posterior draws from the fitted model.

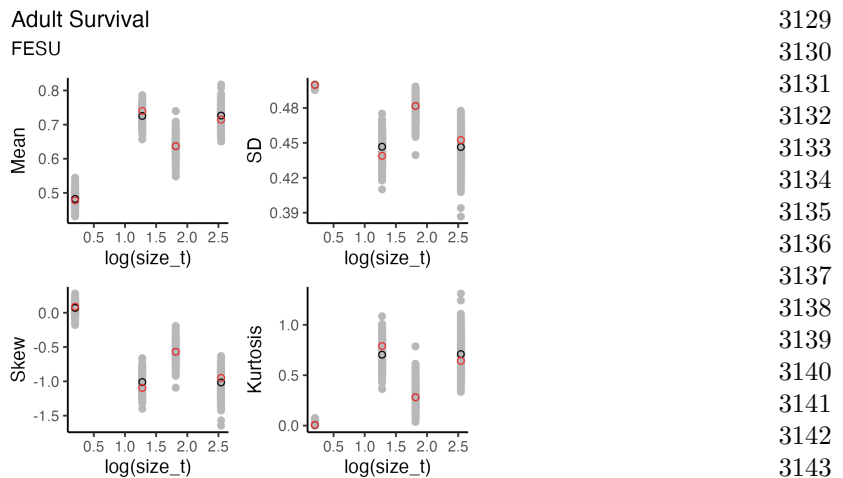


Figure S40: Graphical posterior predictive check for mean and higher moments of *F. subverticillata* survival model across size. Consistency between real data and fitted values across sizes indicates that the vital rate models are accurately capturing size dependence. Points show the value of statistical moments binned across size for the observed data (red circles) compared to the simulated datasets (grey circles) and the median of the simulated values (black circles) generated from 500 posterior draws from the fitted model.

3129  
3130  
3131  
3132  
3133  
3134  
3135  
3136  
3137  
3138  
3139  
3140  
3141  
3142  
3143  
3144  
3145  
3146  
3147  
3148  
3149  
3150  
3151  
3152  
3153  
3154  
3155  
3156  
3157  
3158  
3159  
3160  
3161  
3162  
3163  
3164  
3165  
3166  
3167  
3168  
3169  
3170  
3171  
3172  
3173  
3174

3175  
3176  
3177  
3178  
3179  
3180  
3181  
3182  
3183  
3184  
3185  
3186  
3187  
3188  
3189  
3190  
3191  
3192  
3193  
3194  
3195  
3196  
3197  
3198  
3199  
3200  
3201  
3202  
3203  
3204  
3205  
3206  
3207  
3208  
3209  
3210  
3211  
3212  
3213  
3214  
3215  
3216  
3217  
3218  
3219  
3220

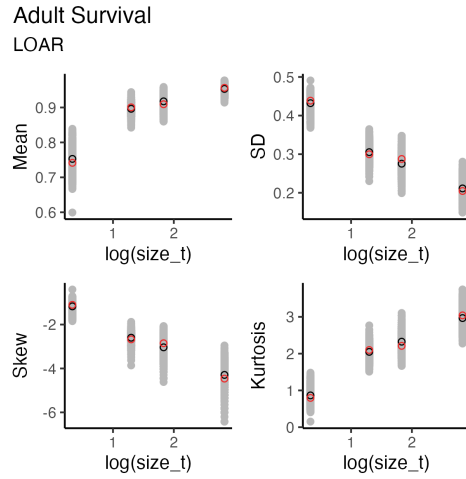


Figure S41: Graphical posterior predictive check for mean and higher moments of *L. arundinacea* survival model across size. Consistency between real data and fitted values across sizes indicates that the vital rate models are accurately capturing size dependence. Points show the value of statistical moments binned across size for the observed data (red circles) compared to the simulated datasets (grey circles) and the median of the simulated values (black circles) generated from 500 posterior draws from the fitted model.

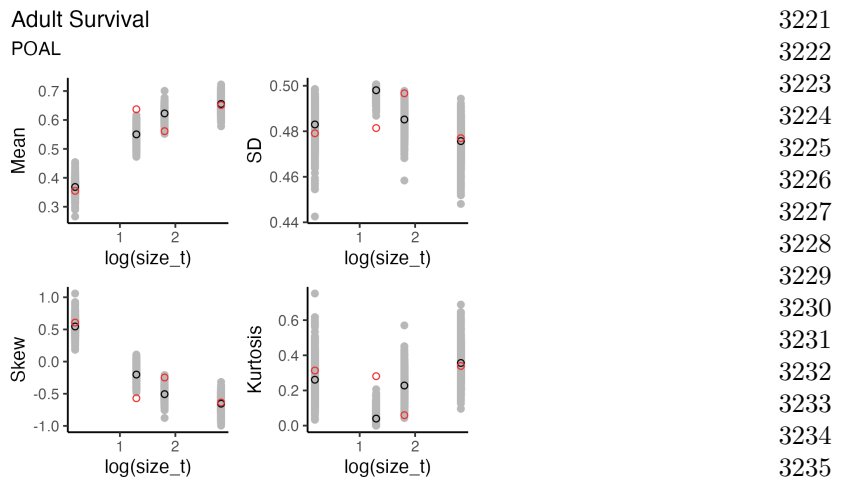


Figure S42: Graphical posterior predictive check for mean and higher moments of *P. alsodes* survival model across size. Consistency between real data and fitted values across sizes indicates that the vital rate models are accurately capturing size dependence. Points show the value of statistical moments binned across size for the observed data (red circles) compared to the simulated datasets (grey circles) and the median of the simulated values (black circles) generated from 500 posterior draws from the fitted model.

3267  
3268  
3269  
3270  
3271  
3272  
3273  
3274  
3275  
3276  
3277  
3278  
3279  
3280  
3281  
3282  
3283  
3284  
3285  
3286  
3287  
3288  
3289  
3290  
3291  
3292  
3293  
3294  
3295  
3296  
3297  
3298  
3299  
3300  
3301  
3302  
3303  
3304  
3305  
3306  
3307  
3308  
3309  
3310  
3311  
3312

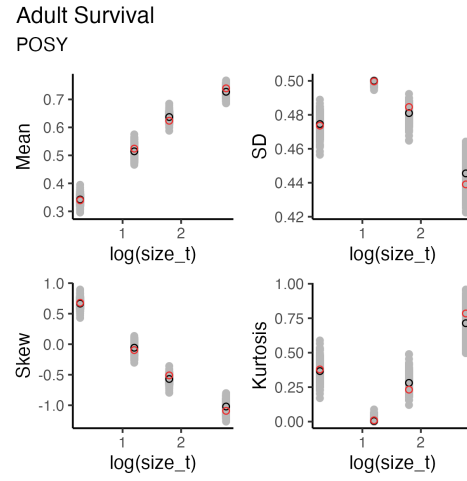
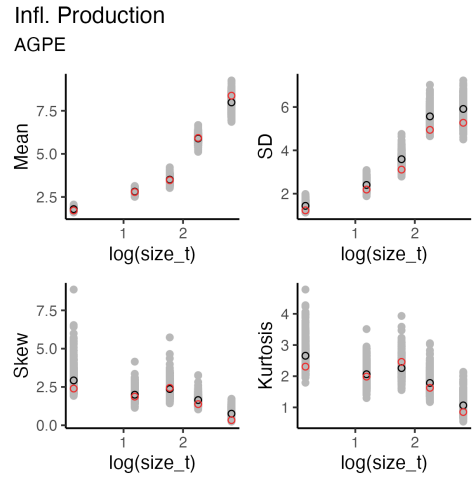


Figure S43: Graphical posterior predictive check for mean and higher moments of *P. sylvestris* survival model across size. Consistency between real data and fitted values across sizes indicates that the vital rate models are accurately capturing size dependence. Points show the value of statistical moments binned across size for the observed data (red circles) compared to the simulated datasets (grey circles) and the median of the simulated values (black circles) generated from 500 posterior draws from the fitted model.



Infl. Production  
 AGPE  
 3313  
 3314  
 3315  
 3316  
 3317  
 3318  
 3319  
 3320  
 3321  
 3322  
 3323  
 3324  
 3325  
 3326  
 3327  
 3328  
 3329  
 3330  
 3331  
 3332  
 3333  
 3334  
 3335  
 3336  
 3337  
 3338  
 3339  
 3340  
 3341  
 3342  
 3343  
 3344  
 3345  
 3346  
 3347  
 3348  
 3349  
 3350  
 3351  
 3352  
 3353  
 3354  
 3355  
 3356  
 3357  
 3358

3359  
3360  
3361  
3362  
3363  
3364  
3365  
3366  
3367  
3368  
3369  
3370  
3371  
3372  
3373  
3374  
3381  
3382  
3383  
3384  
3385  
3386  
3387  
3388  
3389  
3390  
3391  
3392  
3393  
3394  
3395  
3396  
3397  
3398  
3399  
3400  
3401  
3402  
3403  
3404

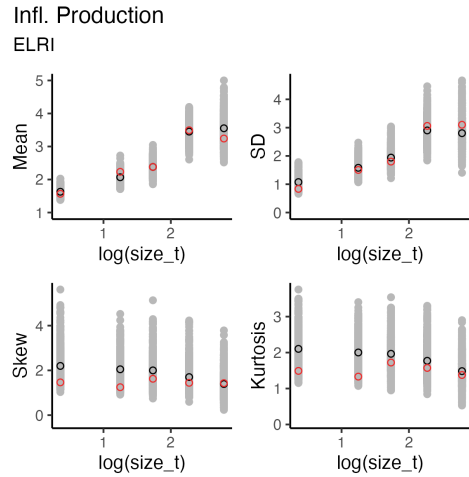
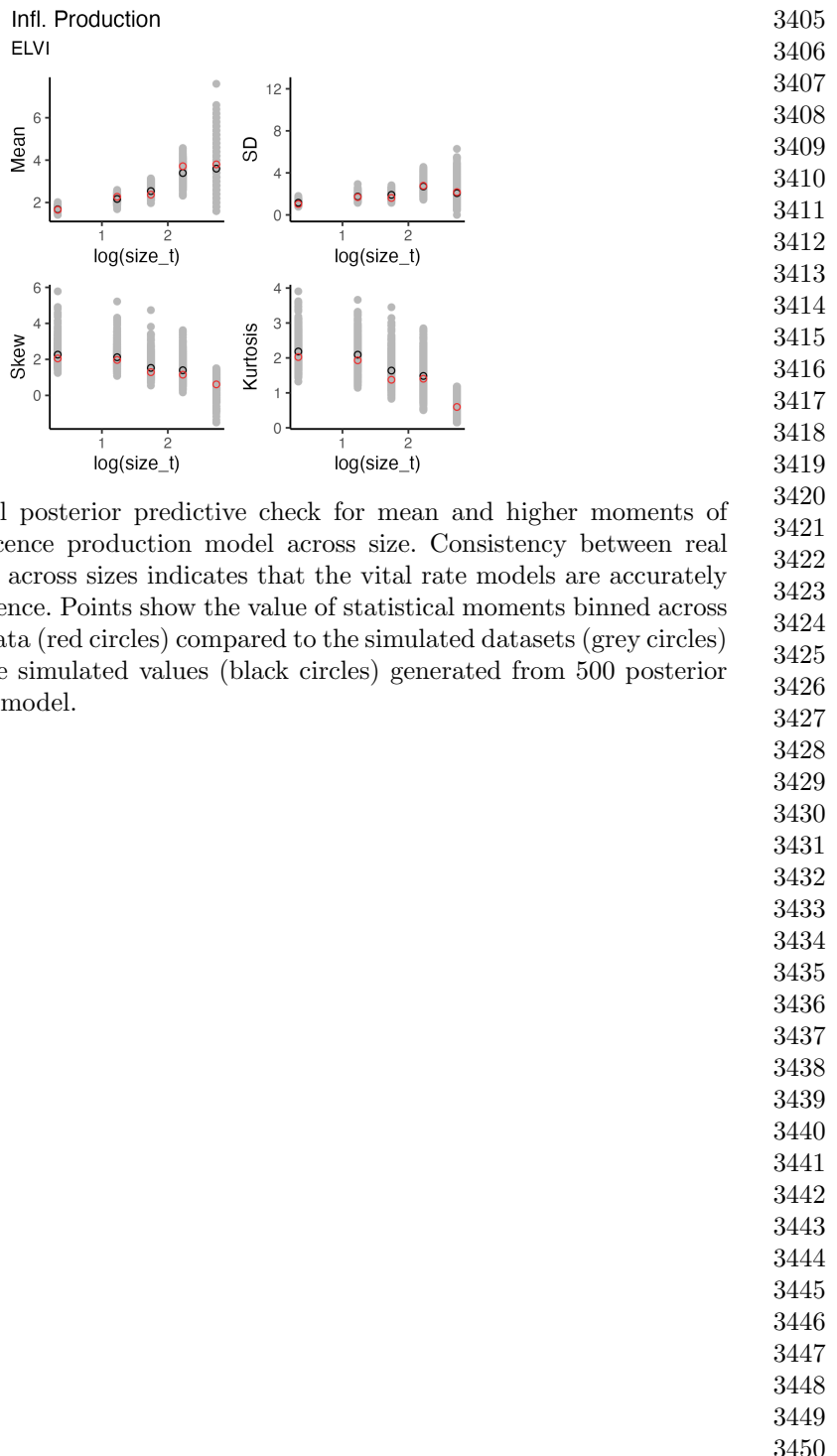


Figure S45: Graphical posterior predictive check for mean and higher moments of *E. villosus* inflorescence production model across size. Consistency between real data and fitted values across sizes indicates that the vital rate models are accurately capturing size dependence. Points show the value of statistical moments binned across size for the observed data (red circles) compared to the simulated datasets (grey circles) and the median of the simulated values (black circles) generated from 500 posterior draws from the fitted model.



3451  
3452  
3453  
3454  
3455  
3456  
3457  
3458  
3459  
3460  
3461  
3462  
3463  
3464  
3465  
3466  
3467  
3468  
3469  
3470  
3471  
3472  
3473  
3474  
3475  
3476  
3477  
3478  
3479  
3480  
3481  
3482  
3483  
3484  
3485  
3486  
3487  
3488  
3489  
3490  
3491  
3492  
3493  
3494  
3495  
3496

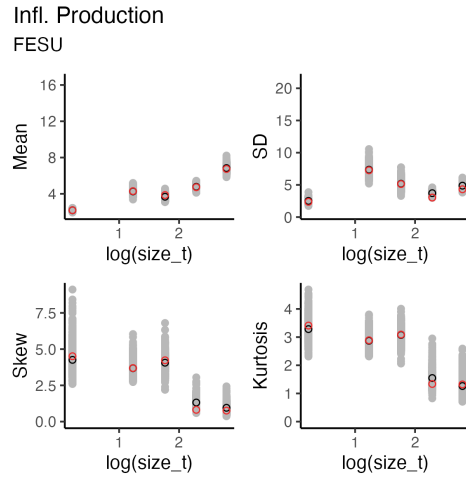


Figure S47: Graphical posterior predictive check for mean and higher moments of *F. subverticillata* inflorescence production model across size. Consistency between real data and fitted values across sizes indicates that the vital rate models are accurately capturing size dependence. Points show the value of statistical moments binned across size for the observed data (red circles) compared to the simulated datasets (grey circles) and the median of the simulated values (black circles) generated from 500 posterior draws from the fitted model.

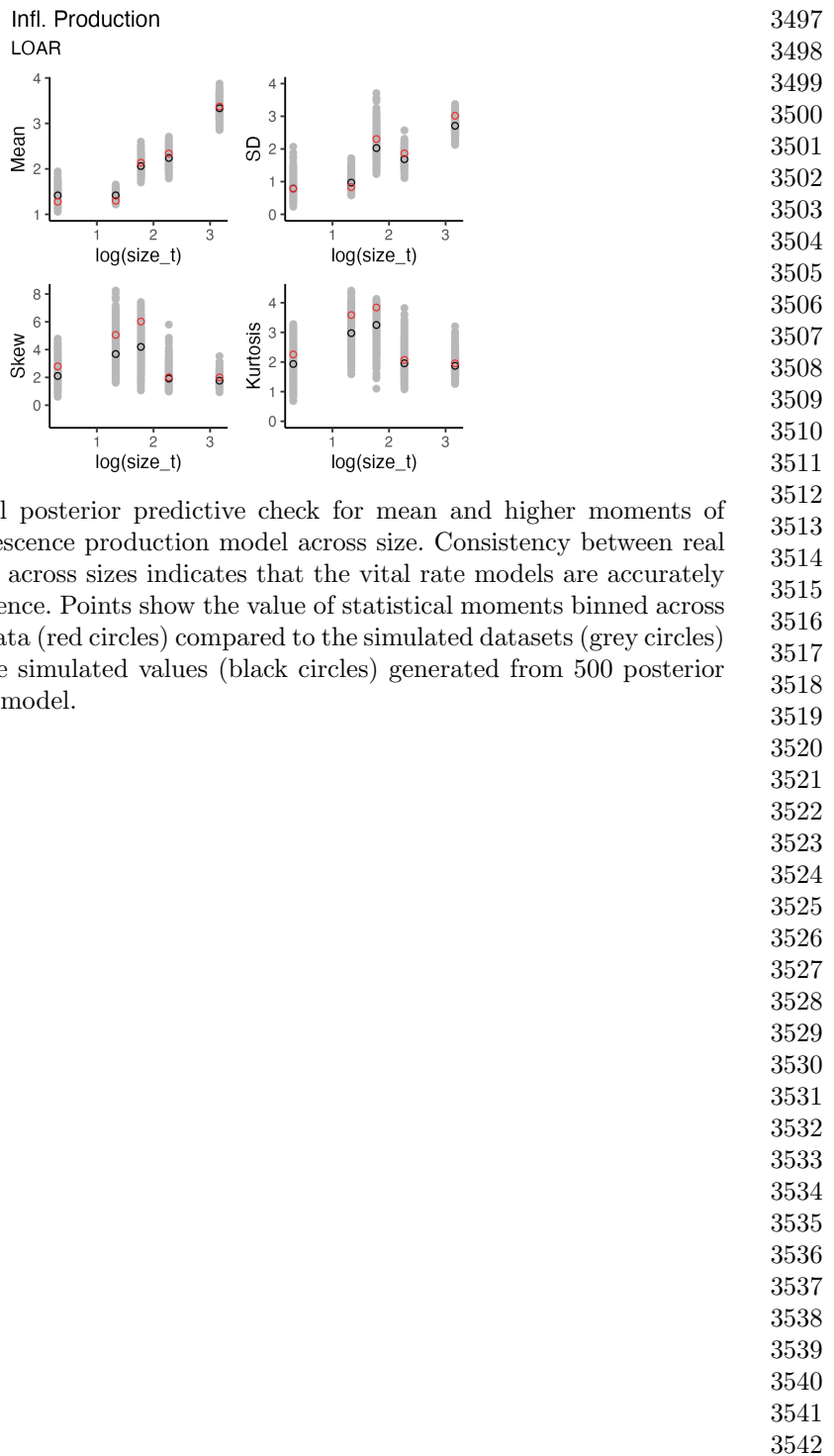


Figure S48: Graphical posterior predictive check for mean and higher moments of *L. arundinacea* inflorescence production model across size. Consistency between real data and fitted values across sizes indicates that the vital rate models are accurately capturing size dependence. Points show the value of statistical moments binned across size for the observed data (red circles) compared to the simulated datasets (grey circles) and the median of the simulated values (black circles) generated from 500 posterior draws from the fitted model.

3543  
3544  
3545  
3546  
3547  
3548  
3549  
3550  
3551  
3552  
3553  
3554  
3555  
3556  
3557  
3558  
3559  
3560  
3561  
3562  
3563  
3564  
3565  
3566  
3567  
3568  
3569  
3570  
3571  
3572  
3573  
3574  
3575  
3576  
3577  
3578  
3579  
3580  
3581  
3582  
3583  
3584  
3585  
3586  
3587  
3588

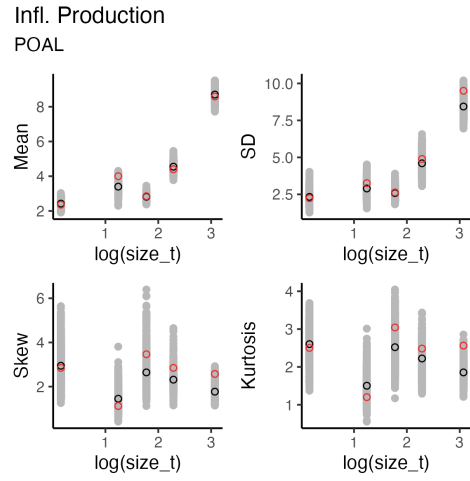


Figure S49: Graphical posterior predictive check for mean and higher moments of  $P$ . *alsodes* inflorescence production model across size. Consistency between real data and fitted values across sizes indicates that the vital rate models are accurately capturing size dependence. Points show the value of statistical moments binned across size for the observed data (red circles) compared to the simulated datasets (grey circles) and the median of the simulated values (black circles) generated from 500 posterior draws from the fitted model.

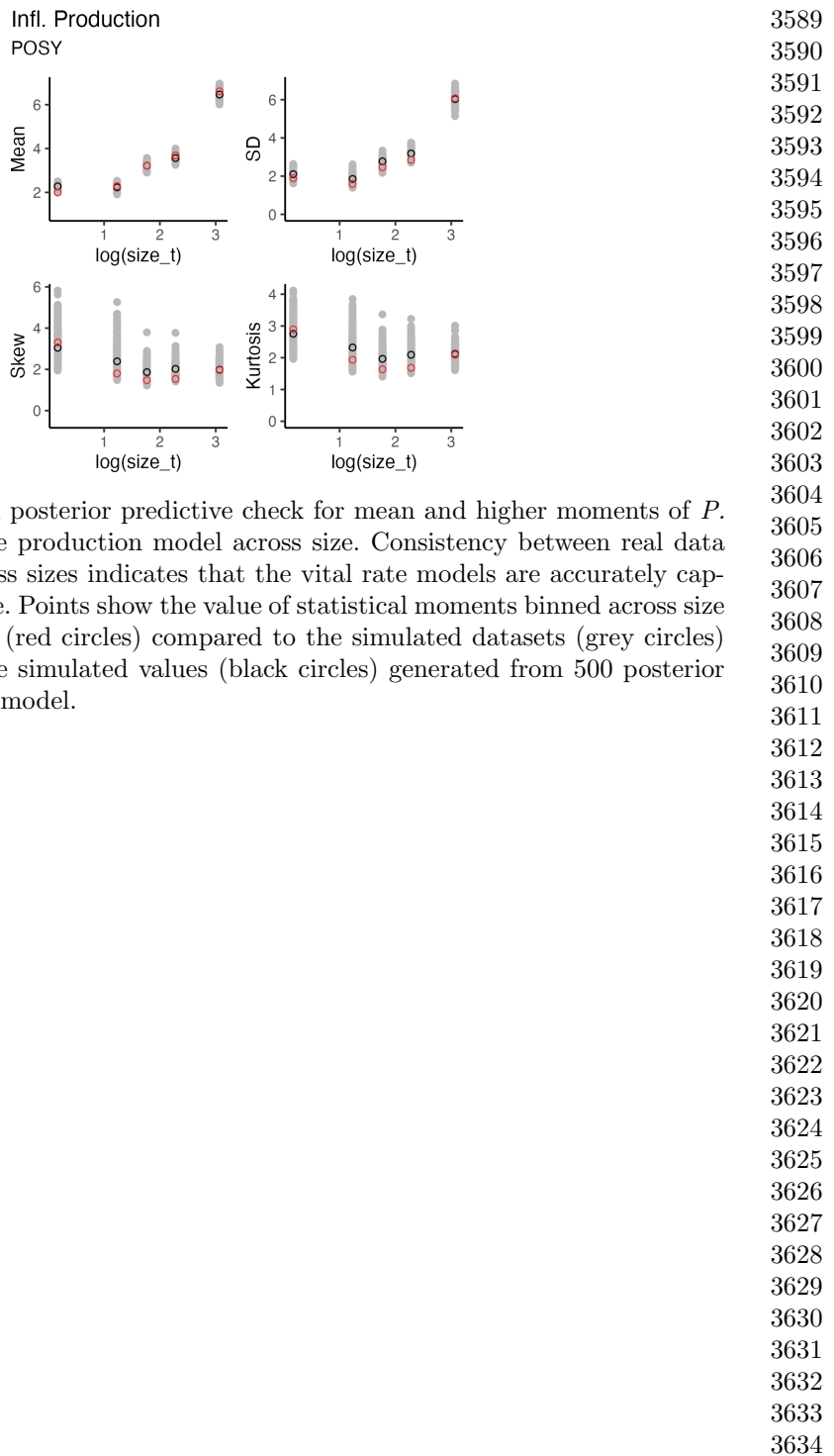


Figure S50: Graphical posterior predictive check for mean and higher moments of *P. sylvestris* inflorescence production model across size. Consistency between real data and fitted values across sizes indicates that the vital rate models are accurately capturing size dependence. Points show the value of statistical moments binned across size for the observed data (red circles) compared to the simulated datasets (grey circles) and the median of the simulated values (black circles) generated from 500 posterior draws from the fitted model.

3635  
3636  
3637  
3638  
3639  
3640  
3641  
3642  
3643  
3644  
3645  
3646  
3647  
3648  
3649  
3650  
3651  
3652  
3653  
3654  
3655  
3656  
3657  
3658  
3659  
3660  
3661  
3662  
3663  
3664  
3665  
3666  
3667  
3668  
3669  
3670  
3671  
3672  
3673  
3674  
3675  
3676  
3677  
3678  
3679  
3680

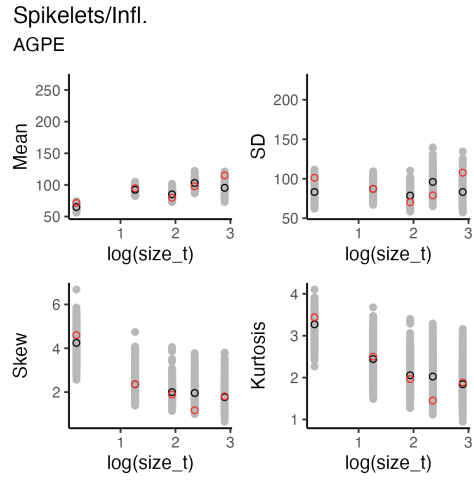


Figure S51: Graphical posterior predictive check for mean and higher moments of *A. perennans* spikelet model across size. Consistency between real data and fitted values across sizes indicates that the vital rate models are accurately capturing size dependence. Points show the value of statistical moments binned across size for the observed data (red circles) compared to the simulated datasets (grey circles) and the median of the simulated values (black circles) generated from 500 posterior draws from the fitted model.

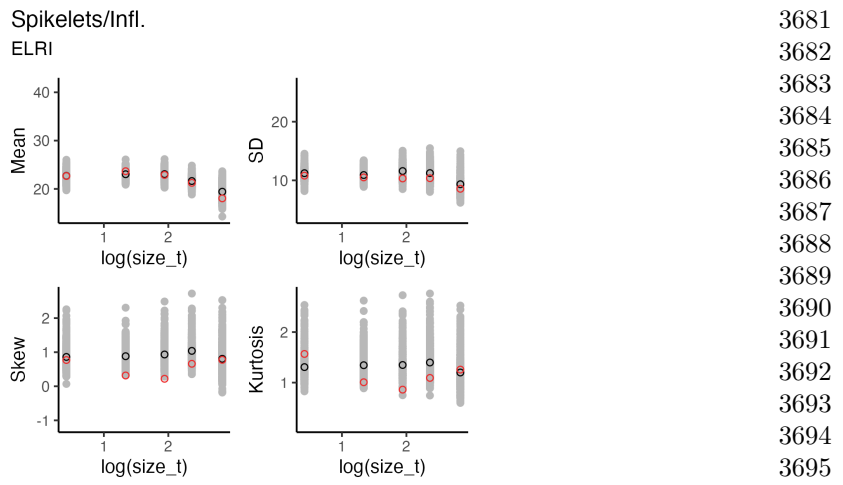


Figure S52: Graphical posterior predictive check for mean and higher moments of *E. villosus* spikelet model across size. Consistency between real data and fitted values across sizes indicates that the vital rate models are accurately capturing size dependence. Points show the value of statistical moments binned across size for the observed data (red circles) compared to the simulated datasets (grey circles) and the median of the simulated values (black circles) generated from 500 posterior draws from the fitted model.

3681  
3682  
3683  
3684  
3685  
3686  
3687  
3688  
3689  
3690  
3691  
3692  
3693  
3694  
3695  
3696  
3697  
3698  
3699  
3700  
3701  
3702  
3703  
3704  
3705  
3706  
3707  
3708  
3709  
3710  
3711  
3712  
3713  
3714  
3715  
3716  
3717  
3718  
3719  
3720  
3721  
3722  
3723  
3724  
3725  
3726

3727  
3728  
3729  
3730  
3731  
3732  
3733  
3734  
3735  
3736  
3737  
3738  
3739  
3740  
3741  
3742  
3743  
3744  
3745  
3746  
3747  
3748  
3749  
3750  
3751  
3752  
3753  
3754  
3755  
3756  
3757  
3758  
3759  
3760  
3761  
3762  
3763  
3764  
3765  
3766  
3767  
3768  
3769  
3770  
3771  
3772

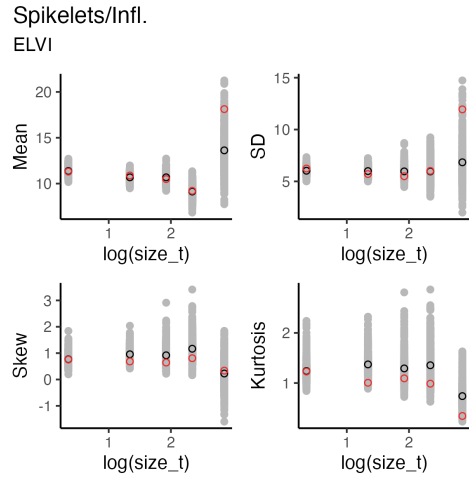


Figure S53: Graphical posterior predictive check for mean and higher moments of *E. virginicus* spikelet model across size. Consistency between real data and fitted values across sizes indicates that the vital rate models are accurately capturing size dependence. Points show the value of statistical moments binned across size for the observed data (red circles) compared to the simulated datasets (grey circles) and the median of the simulated values (black circles) generated from 500 posterior draws from the fitted model.

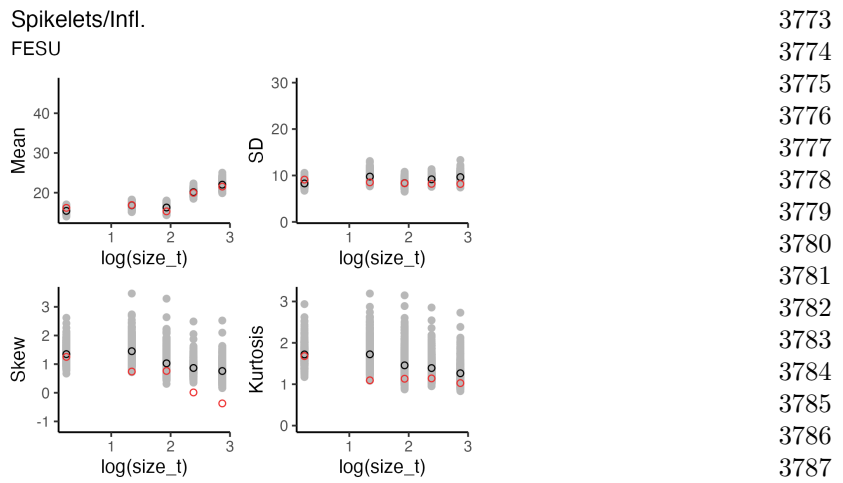


Figure S54: Graphical posterior predictive check for mean and higher moments of *F. subverticillata* spikelet model across size. Consistency between real data and fitted values across sizes indicates that the vital rate models are accurately capturing size dependence. Points show the value of statistical moments binned across size for the observed data (red circles) compared to the simulated datasets (grey circles) and the median of the simulated values (black circles) generated from 500 posterior draws from the fitted model.

3819  
3820  
3821  
3822  
3823  
3824  
3825  
3826  
3827  
3828  
3829  
3830  
3831  
3832  
3833  
3834  
3841  
3842  
3843  
3844  
3845  
3846  
3847  
3848  
3849  
3850  
3851  
3852  
3853  
3854  
3855  
3856  
3857  
3858  
3859  
3860  
3861  
3862  
3863  
3864

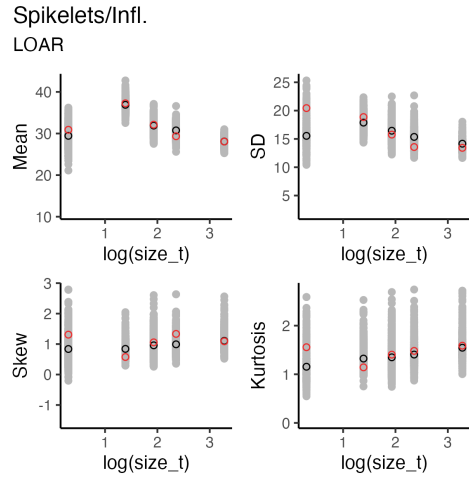


Figure S55: Graphical posterior predictive check for mean and higher moments of *L. arundinacea* spikelet model across size. Consistency between real data and fitted values across sizes indicates that the vital rate models are accurately capturing size dependence. Points show the value of statistical moments binned across size for the observed data (red circles) compared to the simulated datasets (grey circles) and the median of the simulated values (black circles) generated from 500 posterior draws from the fitted model.

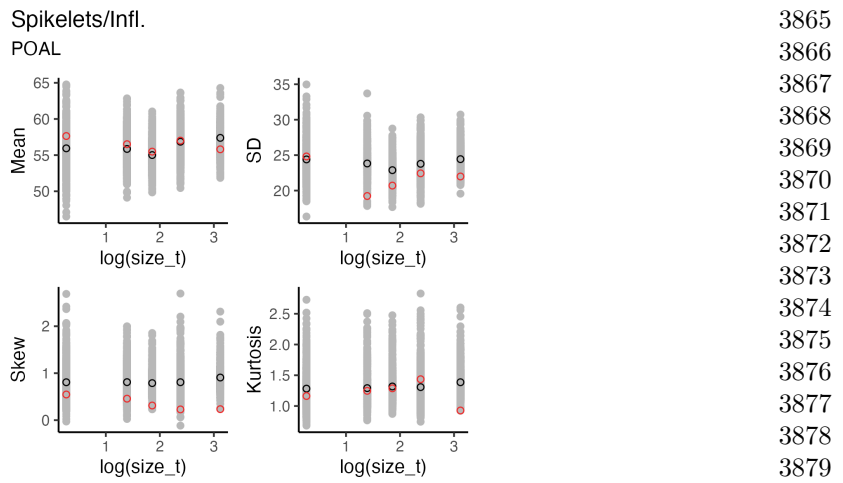


Figure S56: Graphical posterior predictive check for mean and higher moments of *P. alsodes* spikelet model across size. Consistency between real data and fitted values across sizes indicates that the vital rate models are accurately capturing size dependence. Points show the value of statistical moments binned across size for the observed data (red circles) compared to the simulated datasets (grey circles) and the median of the simulated values (black circles) generated from 500 posterior draws from the fitted model.

```

3865
3866
3867
3868
3869
3870
3871
3872
3873
3874
3875
3876
3877
3878
3879
3880
3881
3882
3883
3884
3885
3886
3887
3888
3889
3890
3891
3892
3893
3894
3895
3896
3897
3898
3899
3900
3901
3902
3903
3904
3905
3906
3907
3908
3909
3910

```

3911

3912

3913

3914

3915

3916

3917

3918

3919

3920

3921

3922

3923

3924

3925

3926

Figure S57: Graphical posterior predictive check for mean and higher moments of *P. sylvestris* spikelet model across size. Consistency between real data and fitted values across sizes indicates that the vital rate models are accurately capturing size dependence. Points show the value of statistical moments binned across size for the observed data (red circles) compared to the simulated datasets (grey circles) and the median of the simulated values (black circles) generated from 500 posterior draws from the fitted model.

3933

3934

3935

3936

3937

3938

3939

3940

3941

3942

3943

3944

3945

3946

3947

3948

3949

3950

3951

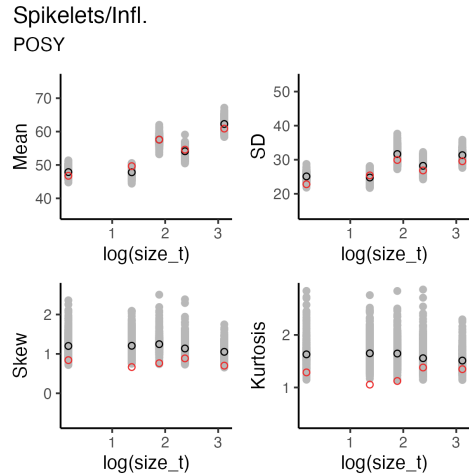
3952

3953

3954

3955

3956



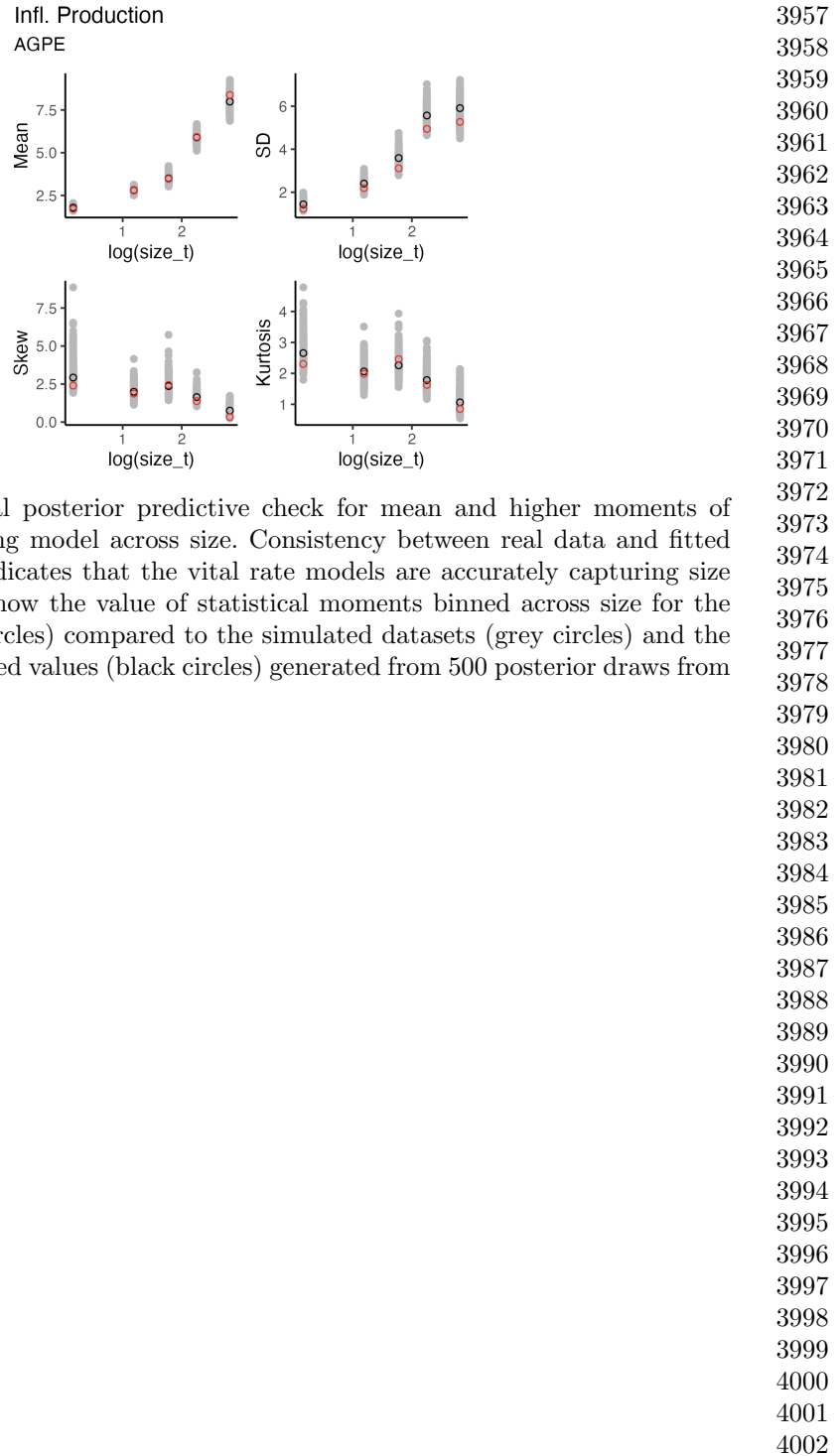


Figure S58: Graphical posterior predictive check for mean and higher moments of *A. perennans* flowering model across size. Consistency between real data and fitted values across sizes indicates that the vital rate models are accurately capturing size dependence. Points show the value of statistical moments binned across size for the observed data (red circles) compared to the simulated datasets (grey circles) and the median of the simulated values (black circles) generated from 500 posterior draws from the fitted model.

4003  
4004  
4005  
4006  
4007  
4008  
4009  
4010  
4011  
4012  
4013  
4014  
4015  
4016  
4017  
4018

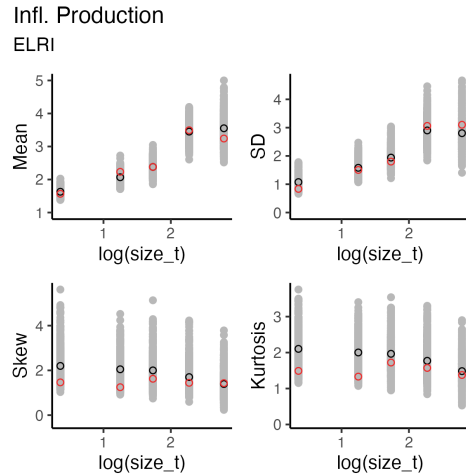
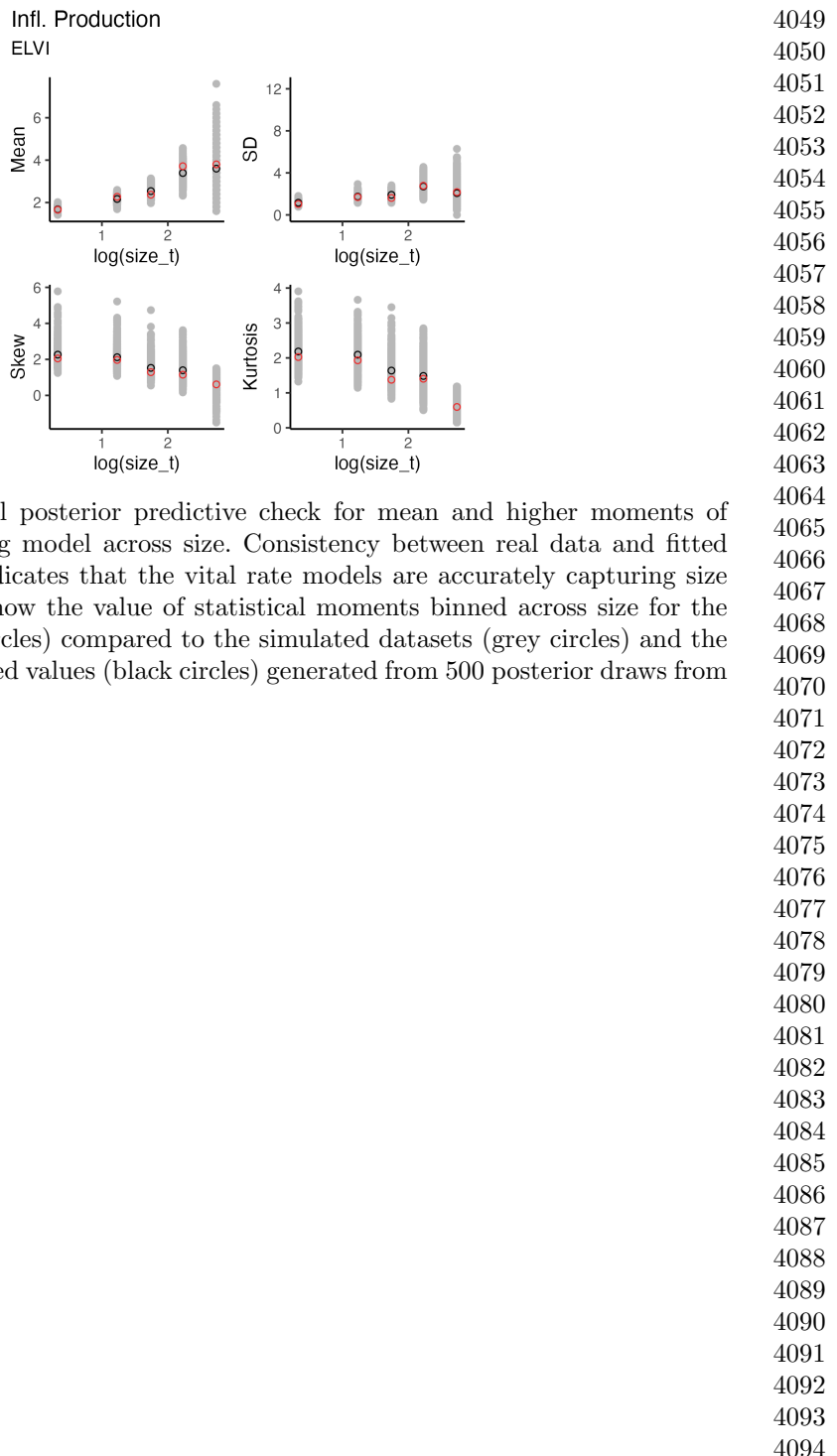


Figure S59: Graphical posterior predictive check for mean and higher moments of *E. villosus* flowering model across size. Consistency between real data and fitted values across sizes indicates that the vital rate models are accurately capturing size dependence. Points show the value of statistical moments binned across size for the observed data (red circles) compared to the simulated datasets (grey circles) and the median of the simulated values (black circles) generated from 500 posterior draws from the fitted model.

4025  
4026  
4027  
4028  
4029  
4030  
4031  
4032  
4033  
4034  
4035  
4036  
4037  
4038  
4039  
4040  
4041  
4042  
4043  
4044  
4045  
4046  
4047  
4048



4095  
4096  
4097  
4098  
4099  
4100  
4101  
4102  
4103  
4104  
4105  
4106  
4107  
4108  
4109  
4110  
4111  
4112  
4113  
4114  
4115  
4116  
4117  
4118  
4119  
4120  
4121  
4122  
4123  
4124  
4125  
4126  
4127  
4128  
4129  
4130  
4131  
4132  
4133  
4134  
4135  
4136  
4137  
4138  
4139  
4140

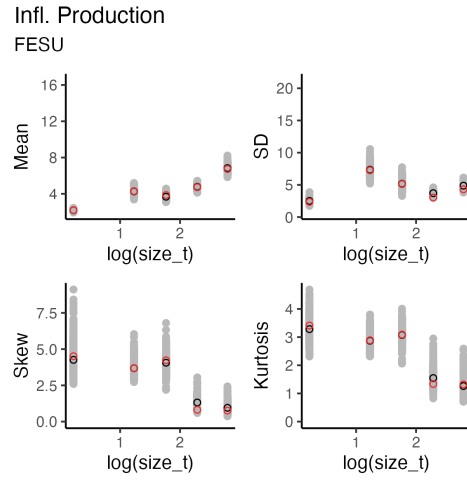


Figure S61: Graphical posterior predictive check for mean and higher moments of *F. subverticillata* flowering model across size. Consistency between real data and fitted values across sizes indicates that the vital rate models are accurately capturing size dependence. Points show the value of statistical moments binned across size for the observed data (red circles) compared to the simulated datasets (grey circles) and the median of the simulated values (black circles) generated from 500 posterior draws from the fitted model.

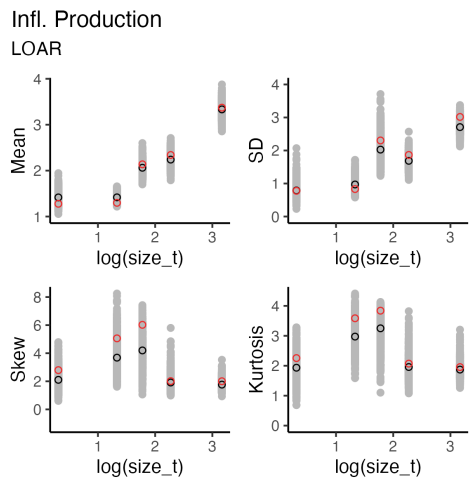
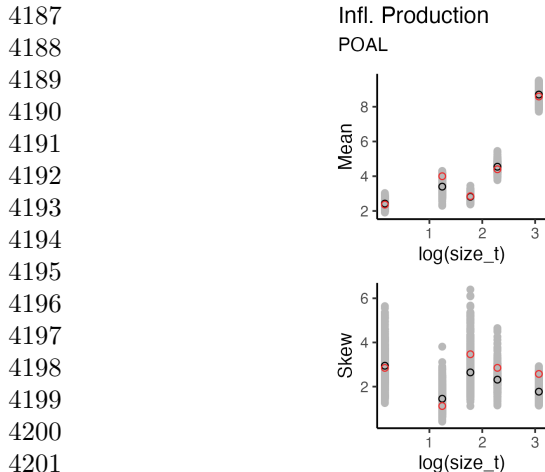


Figure S62: Graphical posterior predictive check for mean and higher moments of *L. arundinacea* flowering model across size. Consistency between real data and fitted values across sizes indicates that the vital rate models are accurately capturing size dependence. Points show the value of statistical moments binned across size for the observed data (red circles) compared to the simulated datasets (grey circles) and the median of the simulated values (black circles) generated from 500 posterior draws from the fitted model.

4141  
4142  
4143  
4144  
4145  
4146  
4147  
4148  
4149  
4150  
4151  
4152  
4153  
4154  
4155  
4156  
4157  
4158  
4159  
4160  
4161  
4162  
4163  
4164  
4165  
4166  
4167  
4168  
4169  
4170  
4171  
4172  
4173  
4174  
4175  
4176  
4177  
4178  
4179  
4180  
4181  
4182  
4183  
4184  
4185  
4186



4203 Figure S63: Graphical posterior predictive check for mean and higher moments of *P.*  
 4204 *alsodes* flowering model across size. Consistency between real data and fitted values  
 4205 across sizes indicates that the vital rate models are accurately capturing size depen-  
 4206 dence. Points show the value of statistical moments binned across size for the observed  
 4207 data (red circles) compared to the simulated datasets (grey circles) and the median  
 4208 of the simulated values (black circles) generated from 500 posterior draws from the  
 4209 fitted model.

4210  
 4211  
 4212  
 4213  
 4214  
 4215  
 4216  
 4217  
 4218  
 4219  
 4220  
 4221  
 4222  
 4223  
 4224  
 4225  
 4226  
 4227  
 4228  
 4229  
 4230  
 4231  
 4232

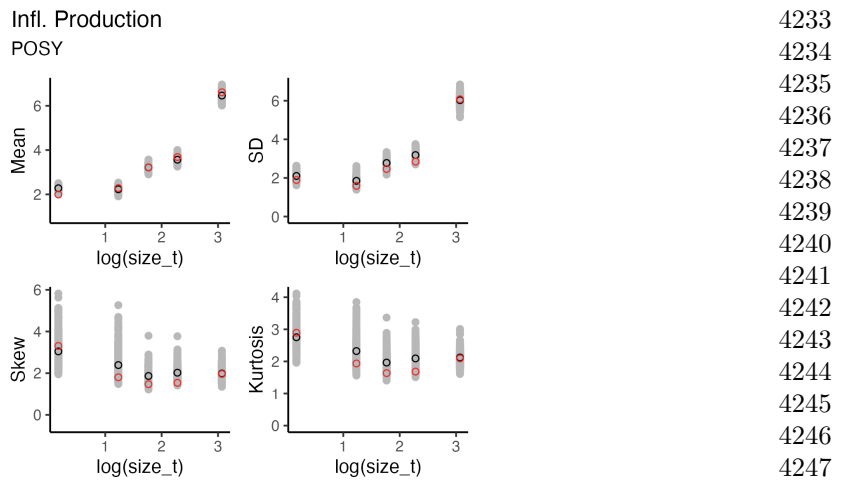
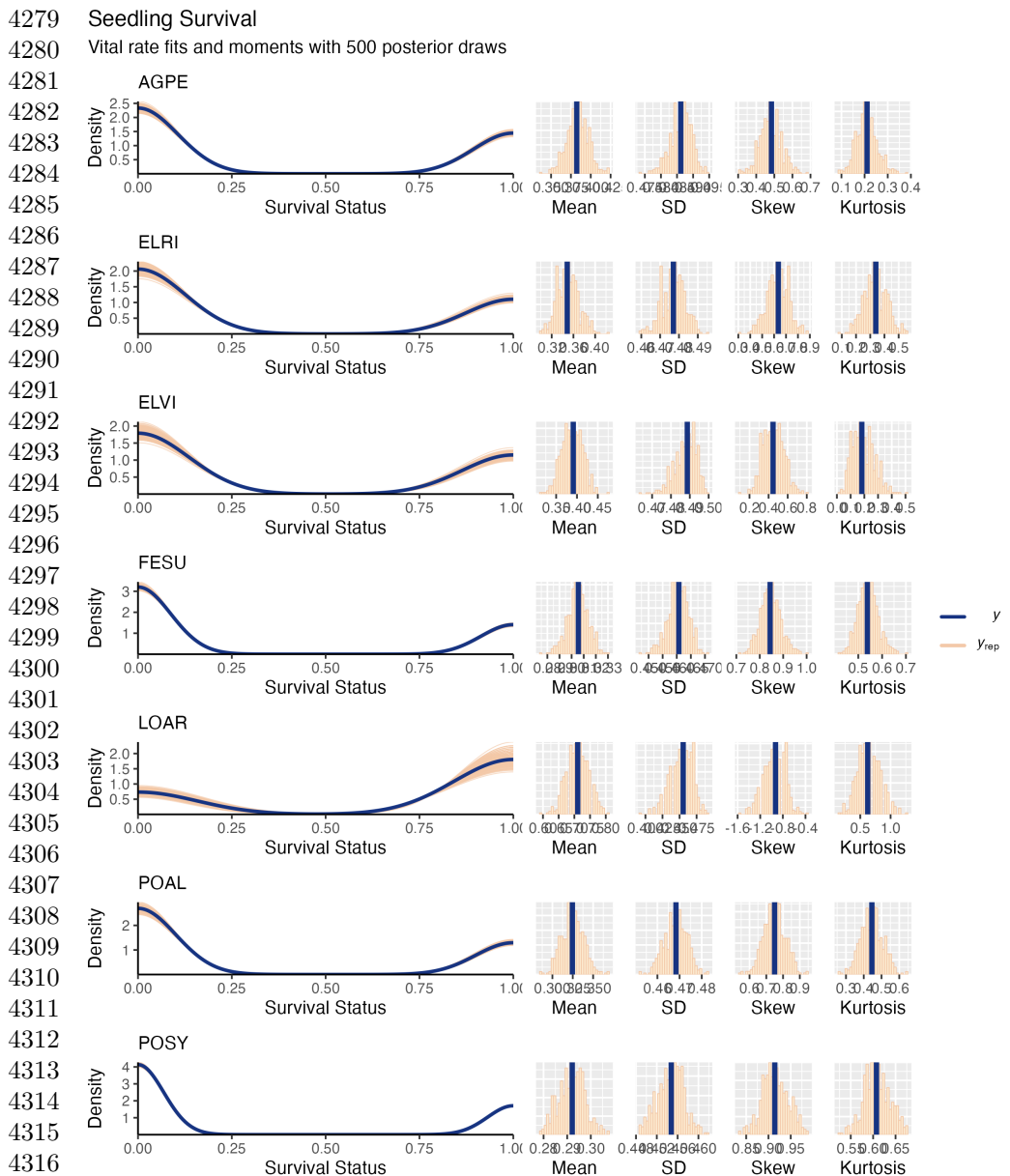


Figure S64: Graphical posterior predictive check for mean and higher moments of *P. sylvestris* flowering model across size. Consistency between real data and fitted values across sizes indicates that the vital rate models are accurately capturing size dependence. Points show the value of statistical moments binned across size for the observed data (red circles) compared to the simulated datasets (grey circles) and the median of the simulated values (black circles) generated from 500 posterior draws from the fitted model.



4318 Figure S65: Graphical posterior predictive check for statistical model of Seedling  
4319 Survival. Consistency between real data and simulated values indicates that fitted  
4320 models describe the data well. Lines show density distributions of observed data (blue  
4321 line) compared to data simulated from fitted models (tan lines) generated from 500  
4322 draws from posterior distributions of model parameters along with the distribution's  
4323 moments.

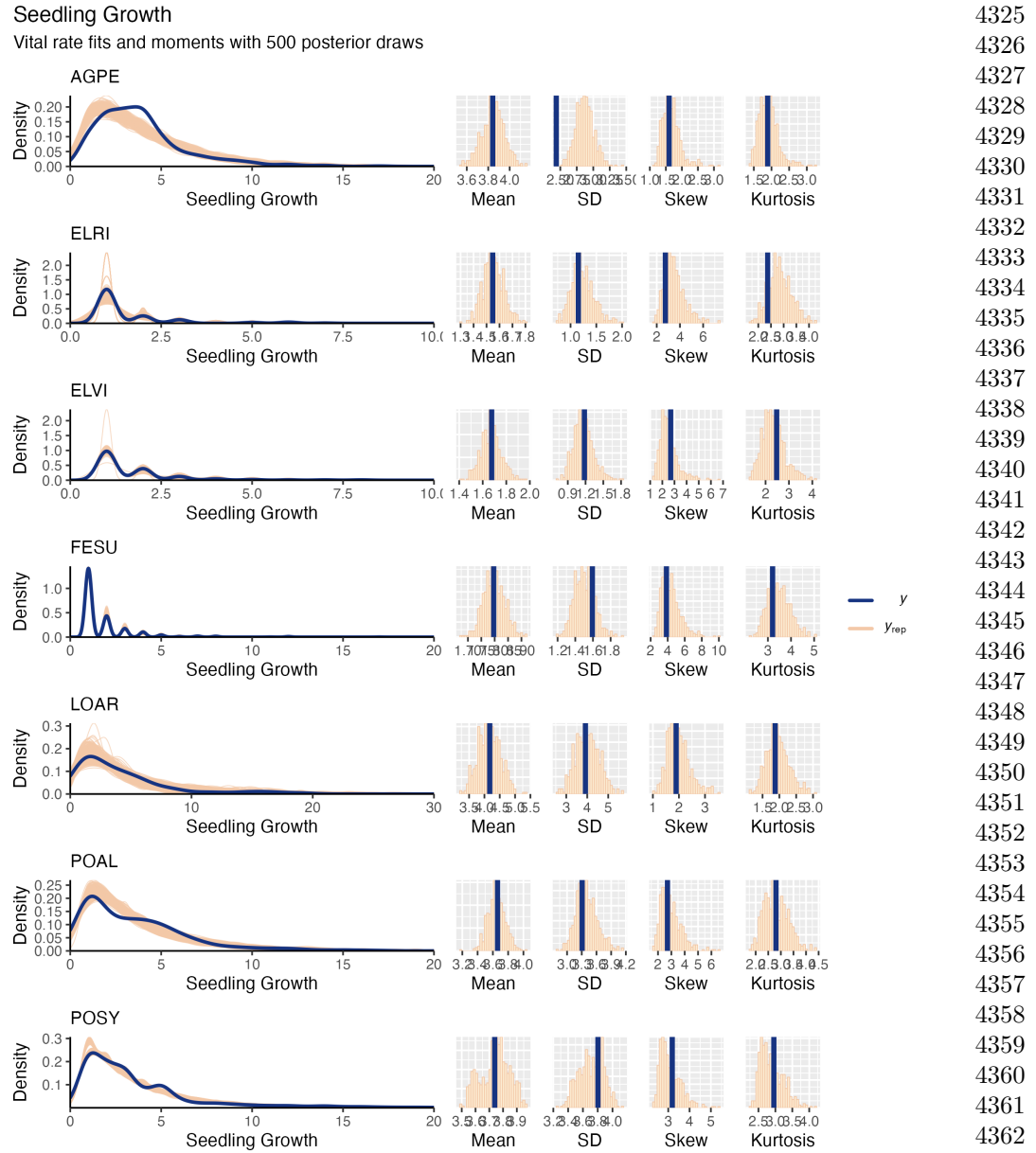
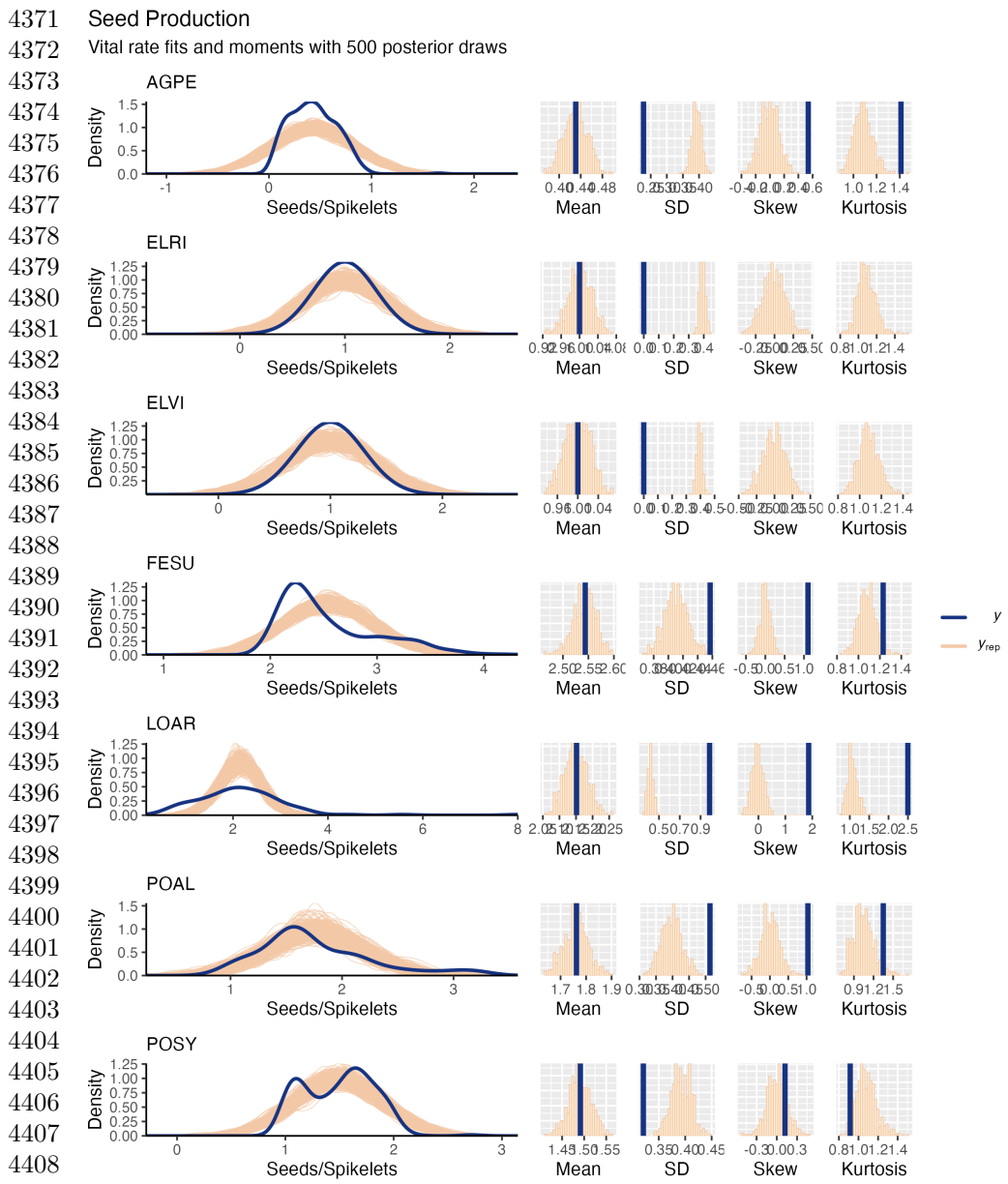


Figure S66: Graphical posterior predictive check for statistical model of Seedling Growth. Consistency between real data and simulated values indicates that fitted models describe the data well. Lines show density distributions of observed data (blue line) compared to data simulated from fitted models (tan lines) generated from 500 draws from posterior distributions of model parameters along with the distribution's moments.



4409 Figure S67: Graphical posterior predictive check for statistical model of Mean Seed-  
4410 s/Spikelet. Consistency between real data and simulated values indicates that fitted  
4411 models describe the data well. Lines show density distributions of observed data (blue  
4412 line) compared to data simulated from fitted models (tan lines) generated from 500  
4413 draws from posterior distributions of model parameters along with the distribution's  
4414 moments.  
4415

4416

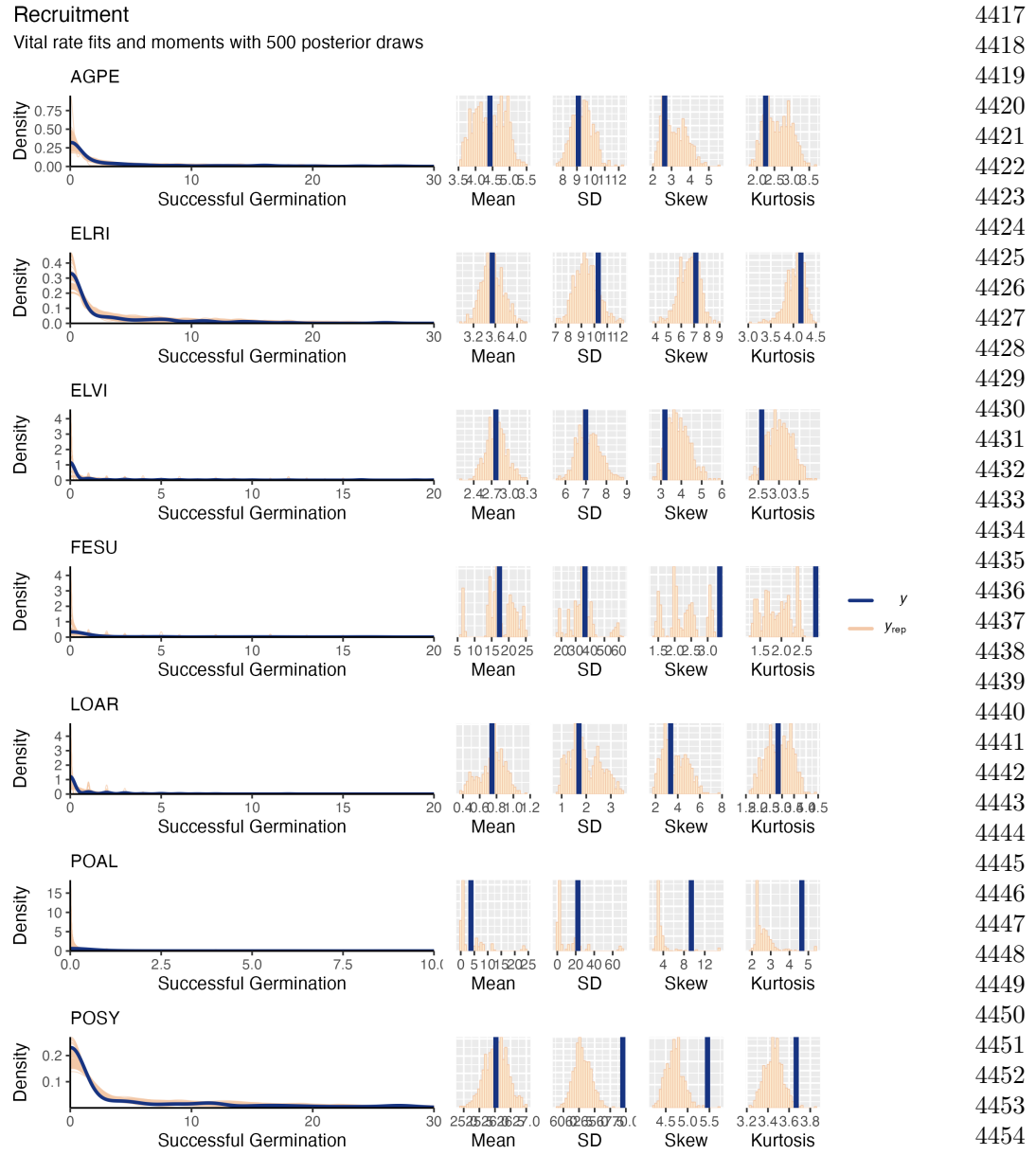


Figure S68: Graphical posterior predictive check for statistical model of Recruitment. Consistency between real data and simulated values indicates that fitted models describe the data well. Lines show density distributions of observed data (blue line) compared to data simulated from fitted models (tan lines) generated from 500 draws from posterior distributions of model parameters along with the distribution's moments.

4463 Adult Survival

4464 Posterior mean with 80% credible intervals

4465

4466

4467

4468

$\beta_{0ho}$ - AGPE; Orig.

4469  $\beta_{0ho}$ - ELRI; Rec.

4470  $\beta_{0ho}$ - ELRI; Orig.

4471  $\beta_{0ho}$ - FESU; Orig.

4472  $\beta_{0ho}$ - LOAR; Orig.

4473  $\beta_{0ho}$ - POAL; Orig.

4474  $\beta_{0ho}$ - POSY; Orig.

4475  $\beta_{0ho}$ - AGPE; Rec.

4476  $\beta_{0ho}$ - ELRI; Rec.

4477  $\beta_{0ho}$ - FESU; Rec.

4478  $\beta_{0ho}$ - LOAR; Rec.

4479  $\beta_{0ho}$ - POAL; Rec.

4480  $\beta_{0ho}$ - POSY; Rec.

4481  $\beta_{2ho}$ - AGPE Size; Orig.

4482  $\beta_{2ho}$ - ELRI Size; Orig.

4483  $\beta_{2ho}$ - ELVI Size; Orig.

4484  $\beta_{2ho}$ - FESU Size; Orig.

4485  $\beta_{2ho}$ - LOAR Size; Orig.

4486  $\beta_{2ho}$ - POAL Size; Orig.

4487  $\beta_{2ho}$ - POSY Size; Orig.

4488  $\beta_{2ho}$ - AGPE Quadratic; Orig.

4489  $\beta_{2ho}$ - ELRI Quadratic; Orig.

4490  $\beta_{2ho}$ - ELVI Quadratic; Orig.

4491  $\beta_{2ho}$ - FESU Quadratic; Orig.

4492  $\beta_{2ho}$ - LOAR Quadratic; Orig.

4493  $\beta_{2ho}$ - POAL Quadratic; Orig.

4494  $\beta_{2ho}$ - POSY Quadratic; Orig.

4495  $\beta_{2ho}$ - AGPE Quadratic; Rec.

4496  $\beta_{2ho}$ - ELRI Quadratic; Rec.

4497  $\beta_{2ho}$ - ELVI Quadratic; Rec.

4498  $\beta_{2ho}$ - FESU Quadratic; Rec.

4499  $\beta_{2ho}$ - LOAR Quadratic; Rec.

4500  $\beta_{2ho}$ - POAL Quadratic; Rec.

4501  $\beta_{2ho}$ - POSY Quadratic; Rec.

4502  $\beta_{1h}$ - AGPE Endo

4503  $\beta_{1h}$ - ELRI Endo

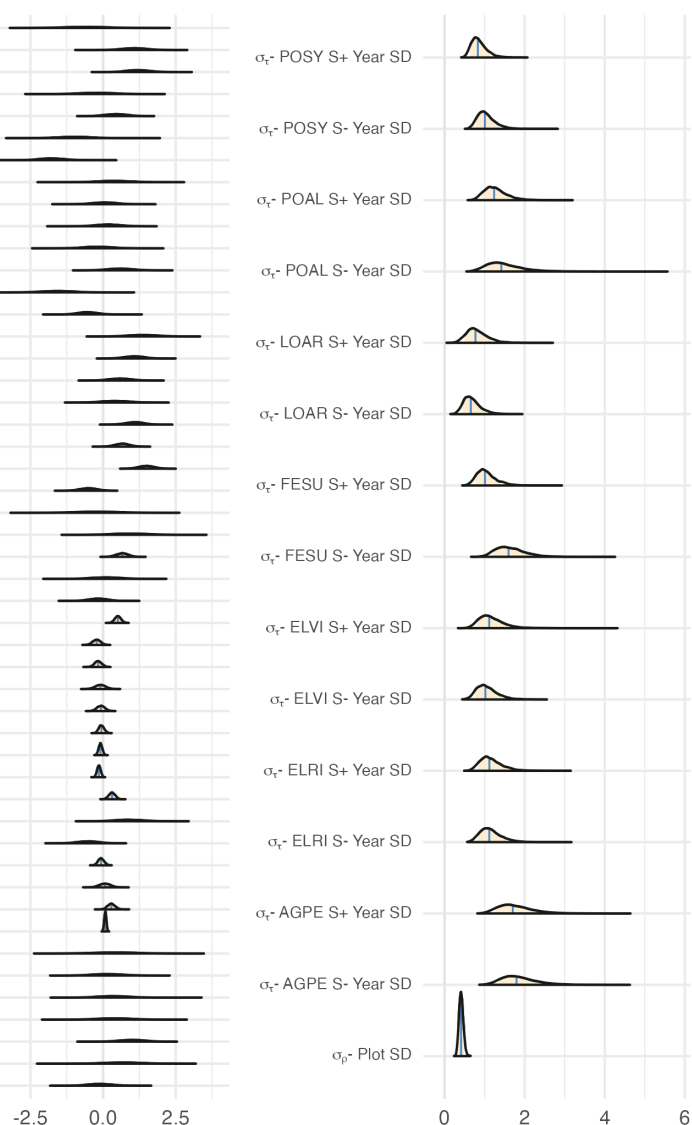
4504  $\beta_{1h}$ - ELVI Endo

4505  $\beta_{1h}$ - FESU Endo

4506  $\beta_{1h}$ - LOAR Endo

4507  $\beta_{1h}$ - POAL Endo

4508  $\beta_{1h}$ - POSY Endo



4504 Figure S69: Posterior distributions of the vital rate regressions for Adult Survival.

4505 Density curves show 80% credible interval along with the posterior posterior mean.

4506

4507

4508

**Seedling Survival**  
 Posterior mean with 80% credible intervals

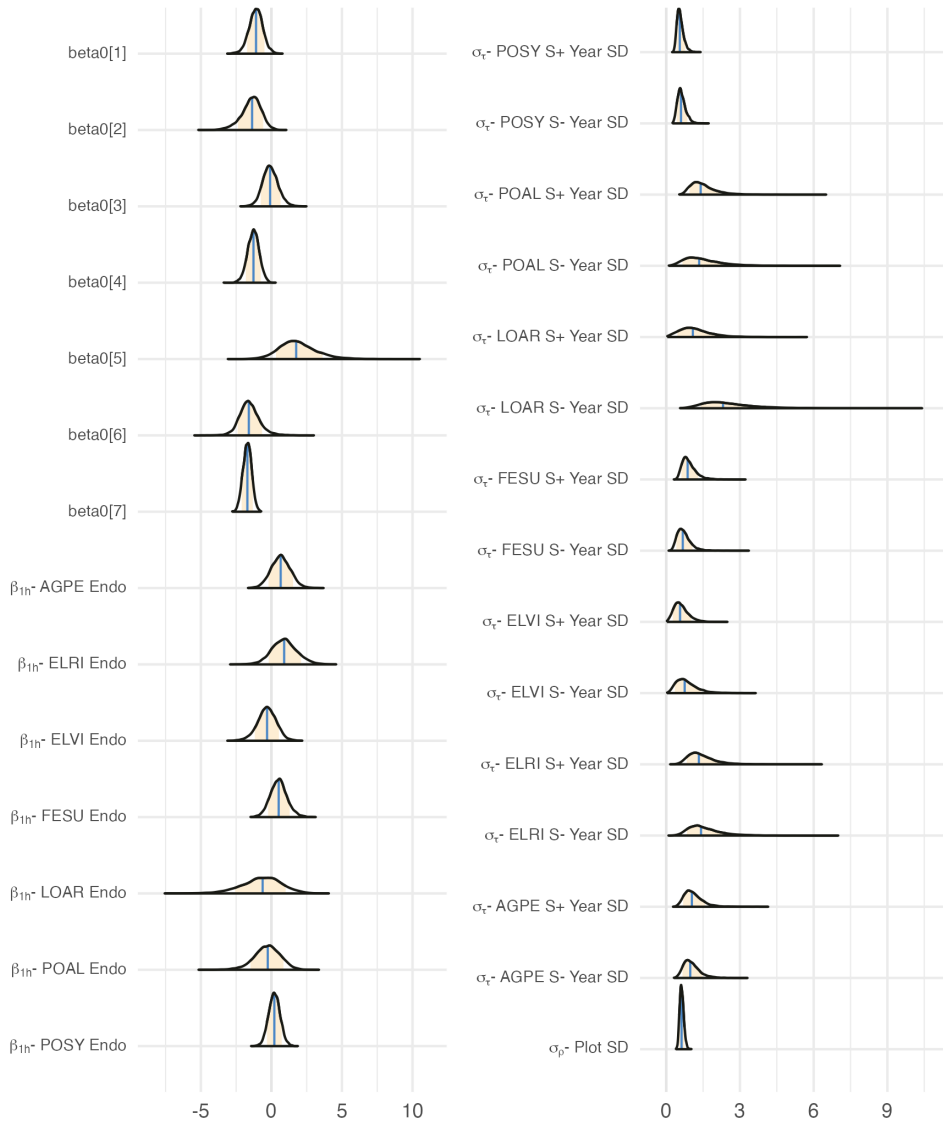
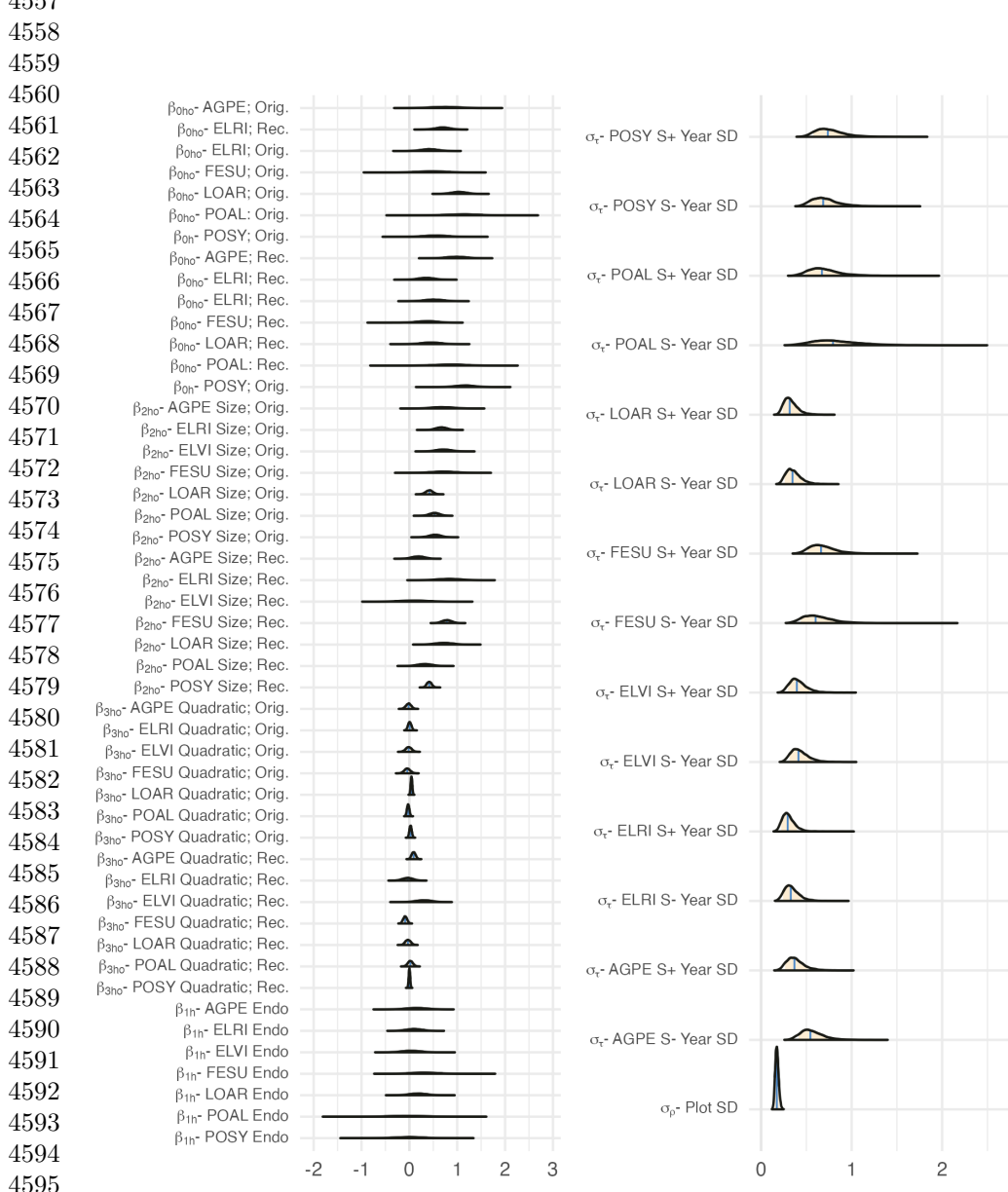


Figure S70: Posterior distributions of the vital rate regressions for Seedling Survival. Density curves show 80% credible interval along with the posterior posterior mean.

4555 Adult Growth  
 4556 Posterior mean with 80% credible intervals



4596 Figure S71: Posterior distributions of the vital rate regressions for Adult Growth.  
 4597 Density curves show 80% credible interval along with the posterior posterior mean.  
 4598  
 4599  
 4600

**Seedling Growth**  
 Posterior mean with 80% credible intervals

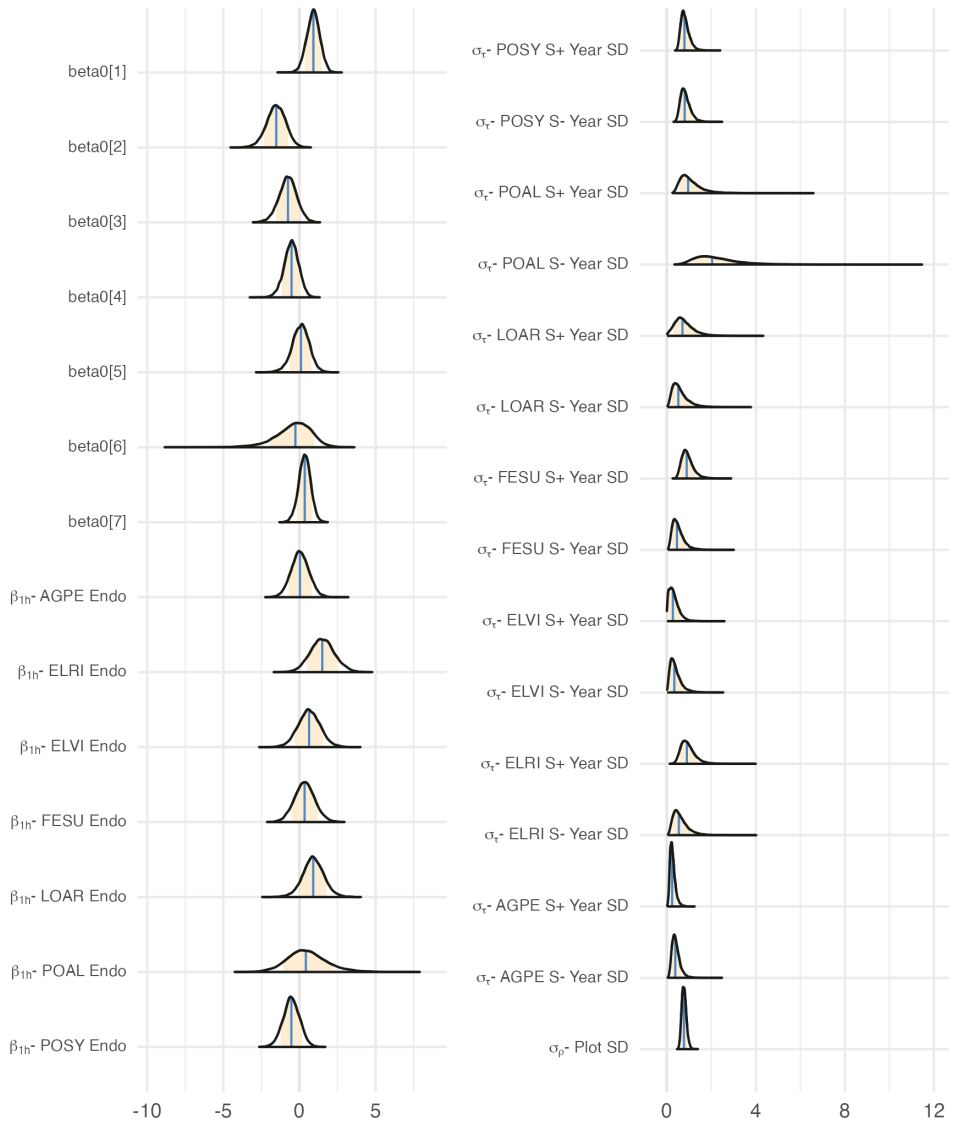
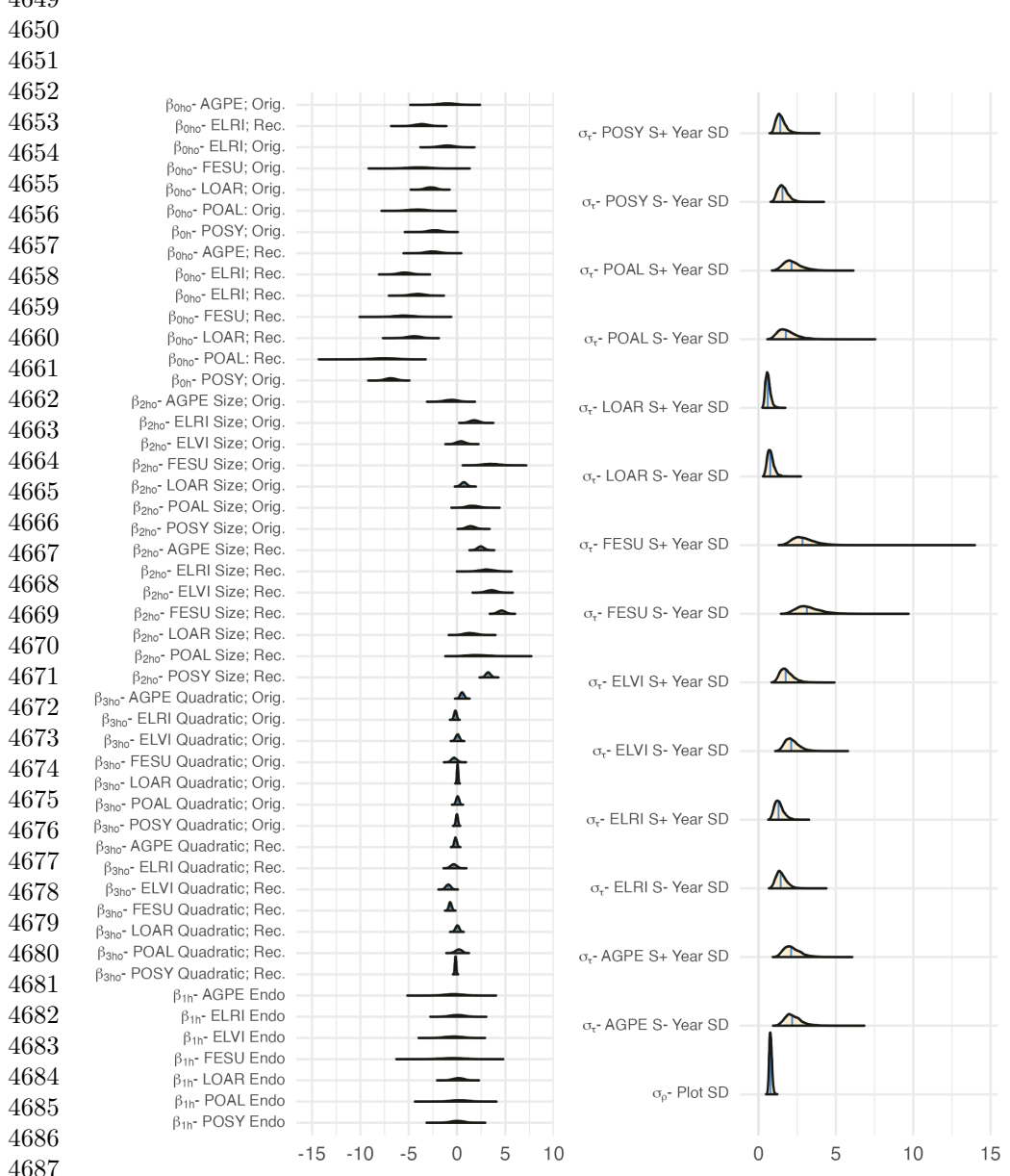


Figure S72: Posterior distributions of the vital rate regressions for Seedling Growth. Density curves show 80% credible interval along with the posterior posterior mean.

4647 Flowering Probability  
 4648 Posterior mean with 80% credible intervals



4688 Figure S73: Posterior distributions of the vital rate regressions for Flowering Probability. Density curves show 80% credible interval along with the posterior posterior mean.

4691  
 4692

## Infl. Production

Posterior mean with 80% credible intervals

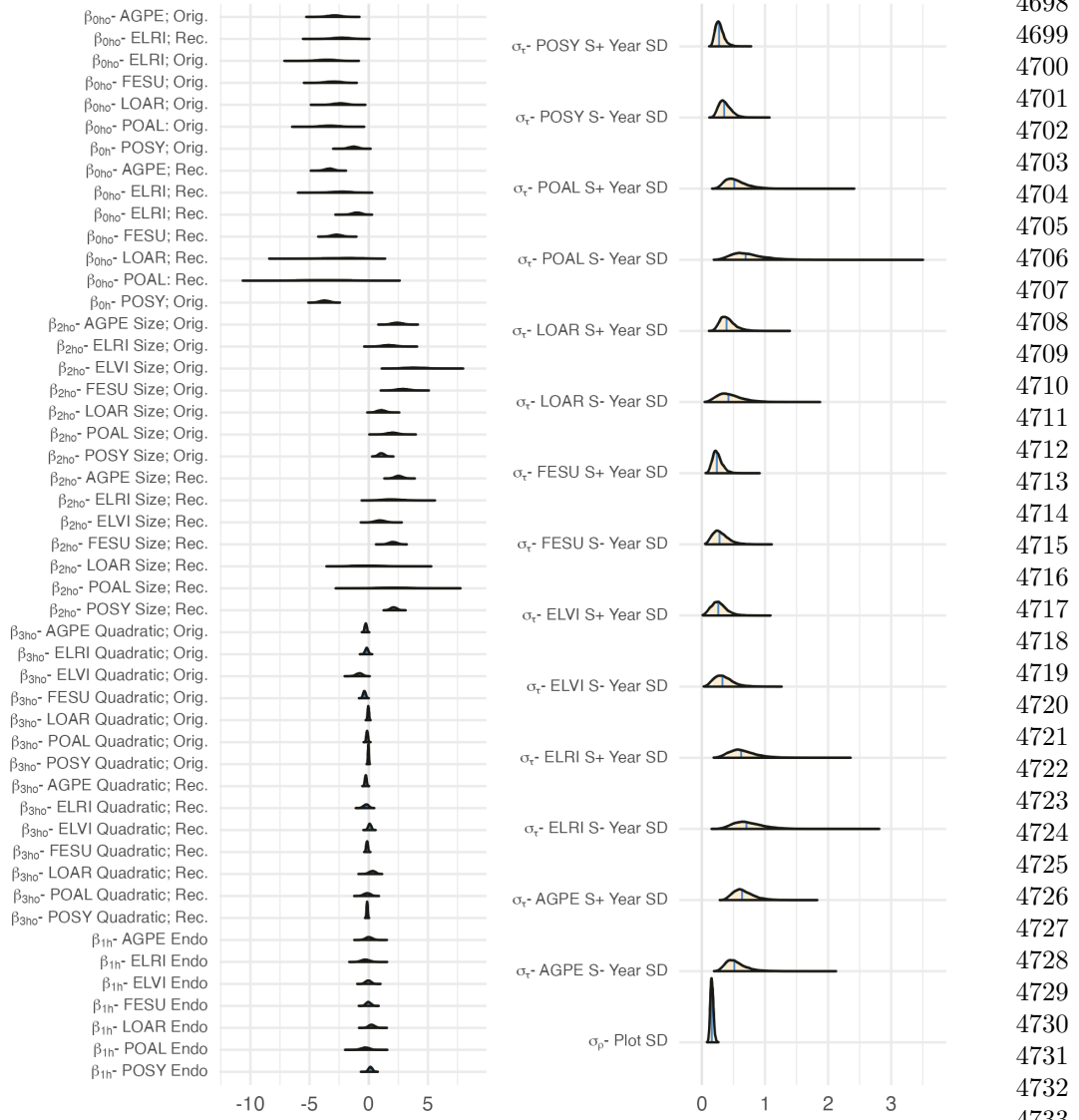
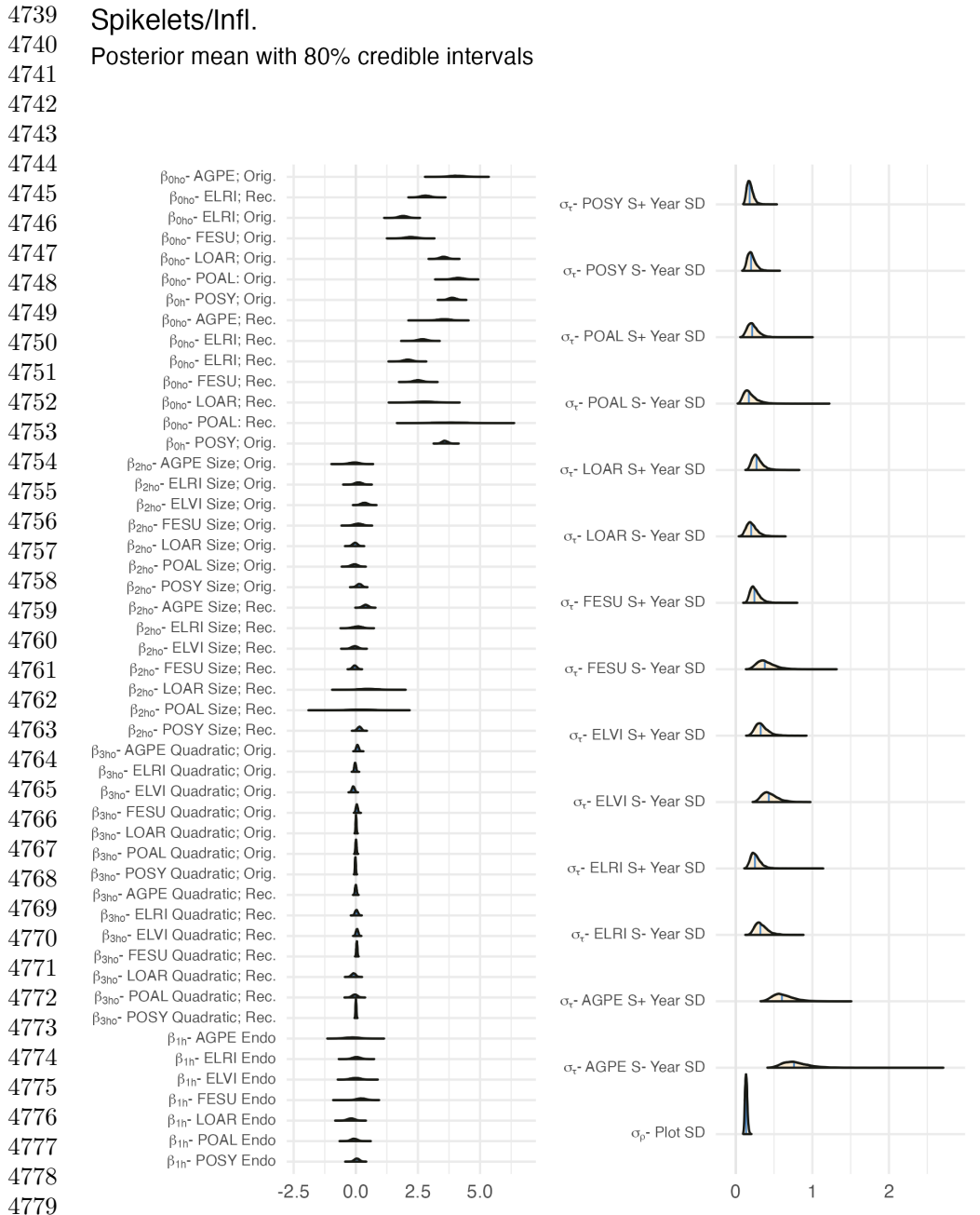


Figure S74: Posterior distributions of the vital rate regressions for Inflorescence Production. Density curves show 80% credible interval along with the posterior posterior mean.



4780 Figure S75: Posterior distributions of the vital rate regressions for Spikelets/Inflorescence. Density curves show 80% credible interval along with the posterior posterior  
 4781 mean.

4783  
 4784

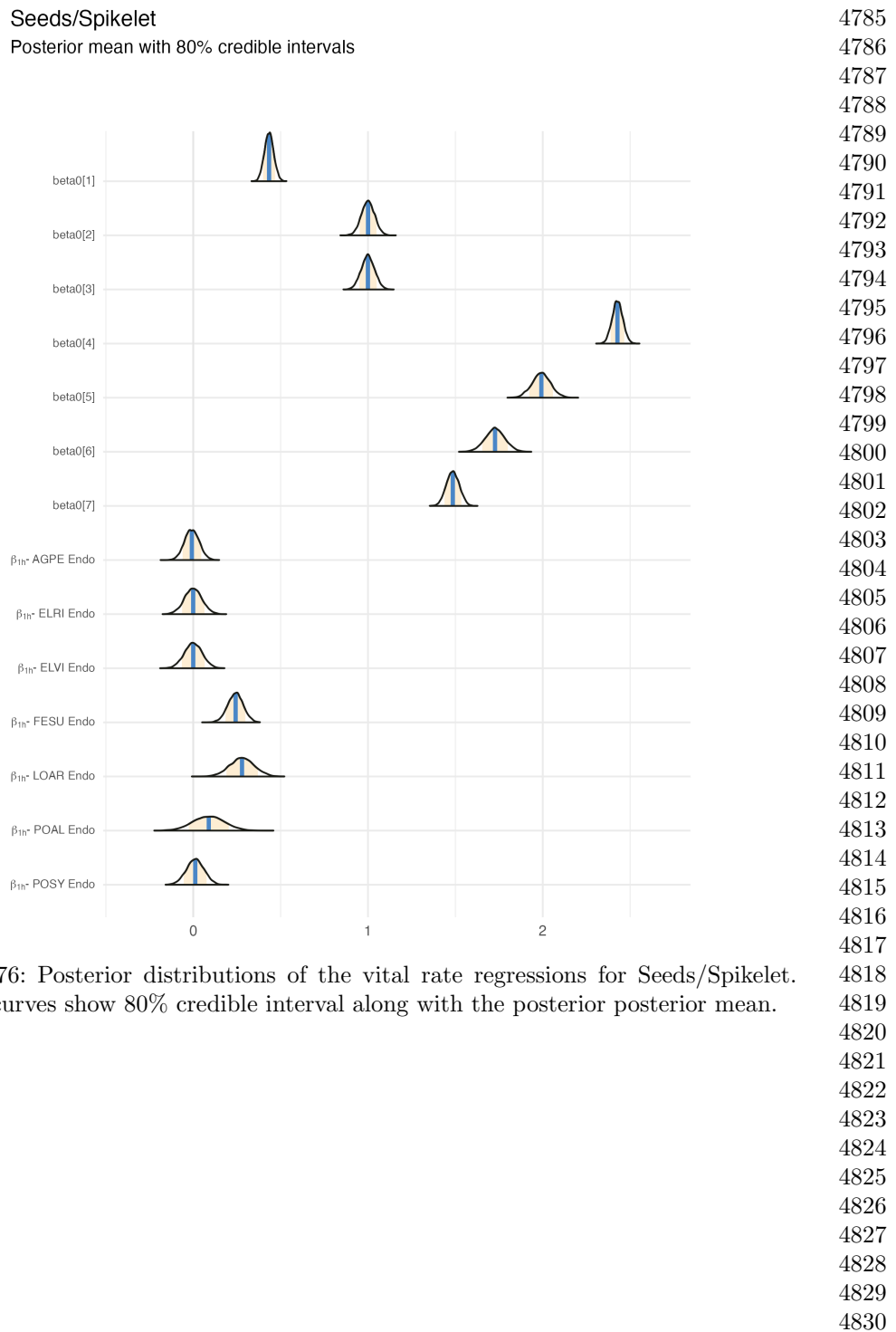
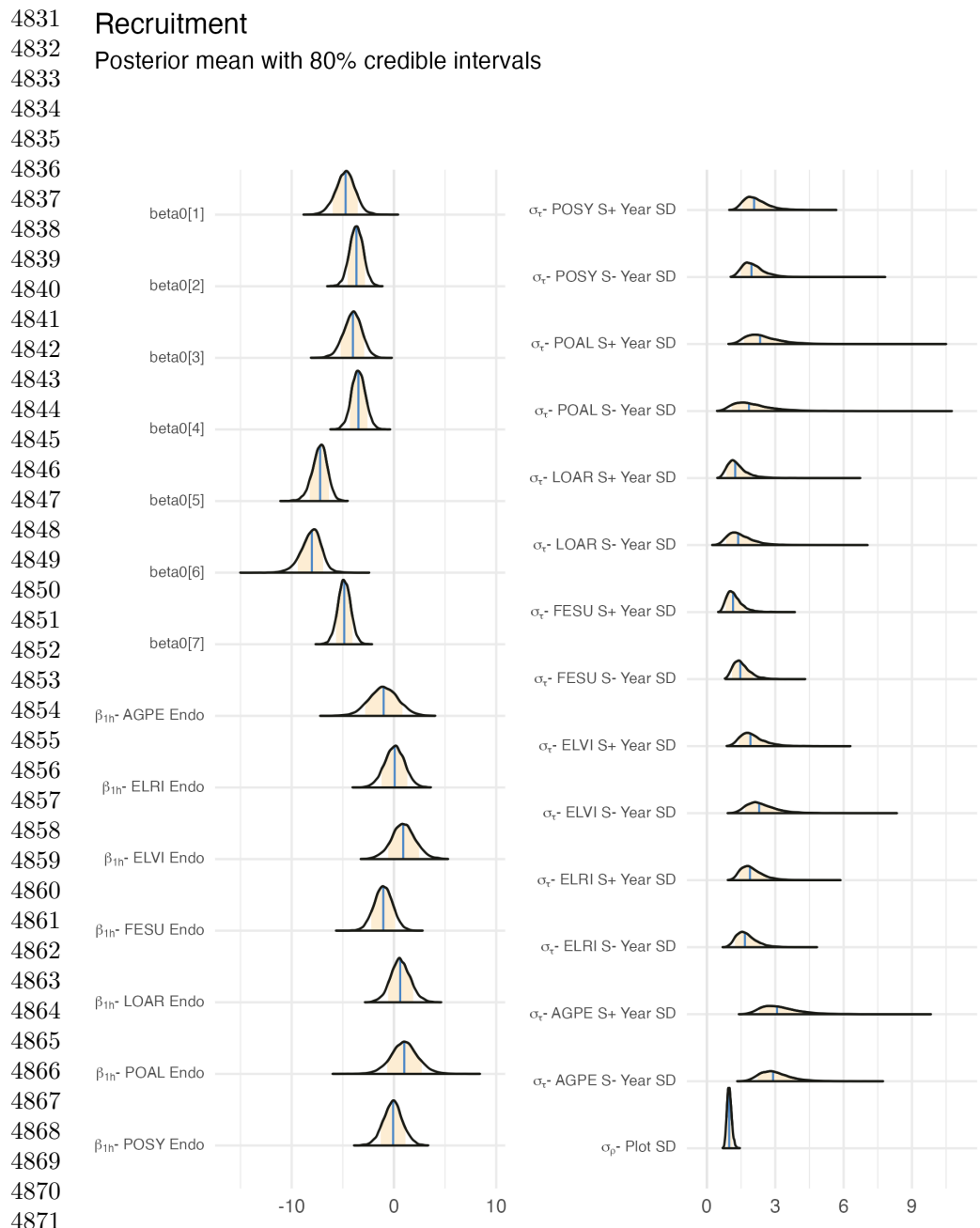


Figure S76: Posterior distributions of the vital rate regressions for Seeds/Spikelet. Density curves show 80% credible interval along with the posterior posterior mean.



4872 Figure S77: Posterior distributions of the vital rate regressions for Recruitment.

4873 Density curves show 80% credible interval along with the posterior posterior mean.

4874

4875

4876

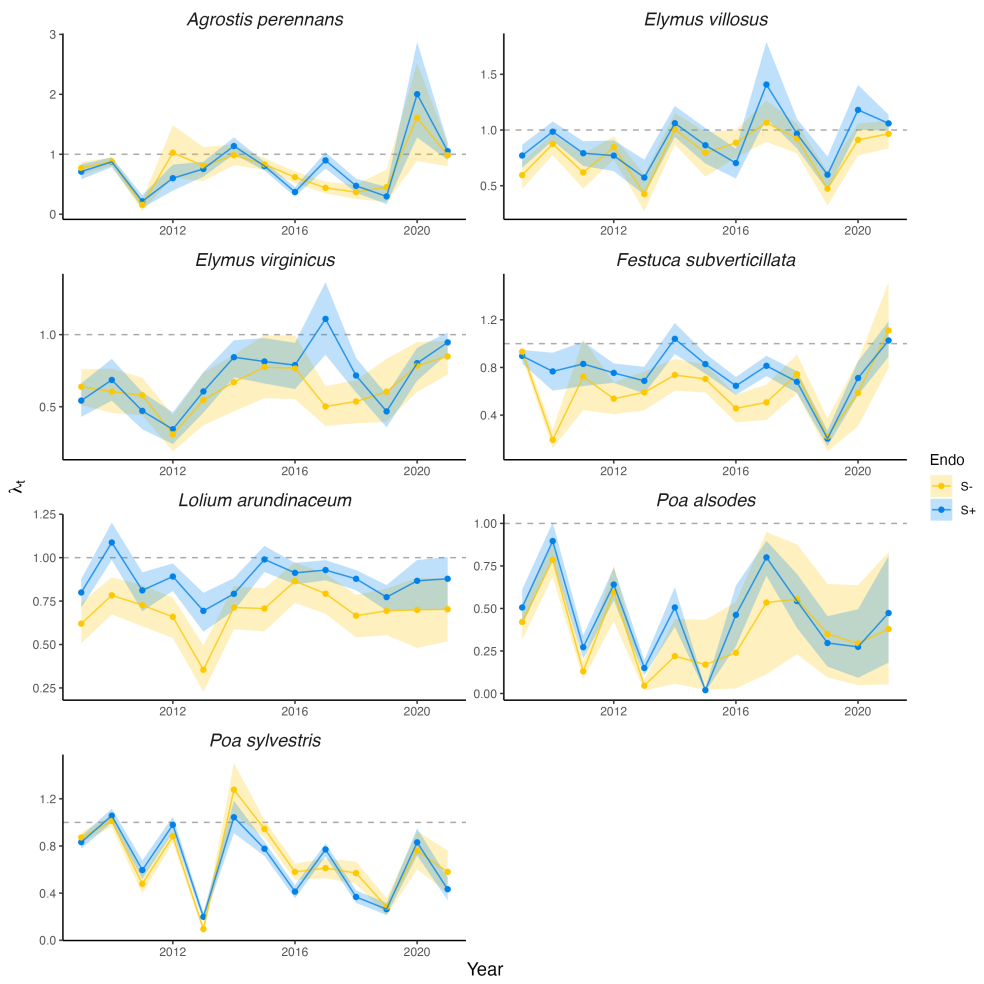


Figure S78: Annual growth rate values ( $\lambda_t$ ) over thirteen years. Mean values for symbiotic (blue) and symbiont-free (yellow) population growth rates are shown along with 80% credible intervals. Dashed line at  $\lambda_t = 1$  indicates stable population growth rate. All values are calculated from matrix models representing recruit plants.

4877  
4878  
4879  
4880  
4881  
4882  
4883  
4884  
4885  
4886  
4887  
4888  
4889  
4890  
4891  
4892  
4893  
4894  
4895  
4896  
4897  
4898  
4899  
4900  
4901  
4902  
4903  
4904  
4905  
4906  
4907  
4908  
4909  
4910  
4911  
4912  
4913  
4914  
4915  
4916  
4917  
4918  
4919  
4920  
4921  
4922

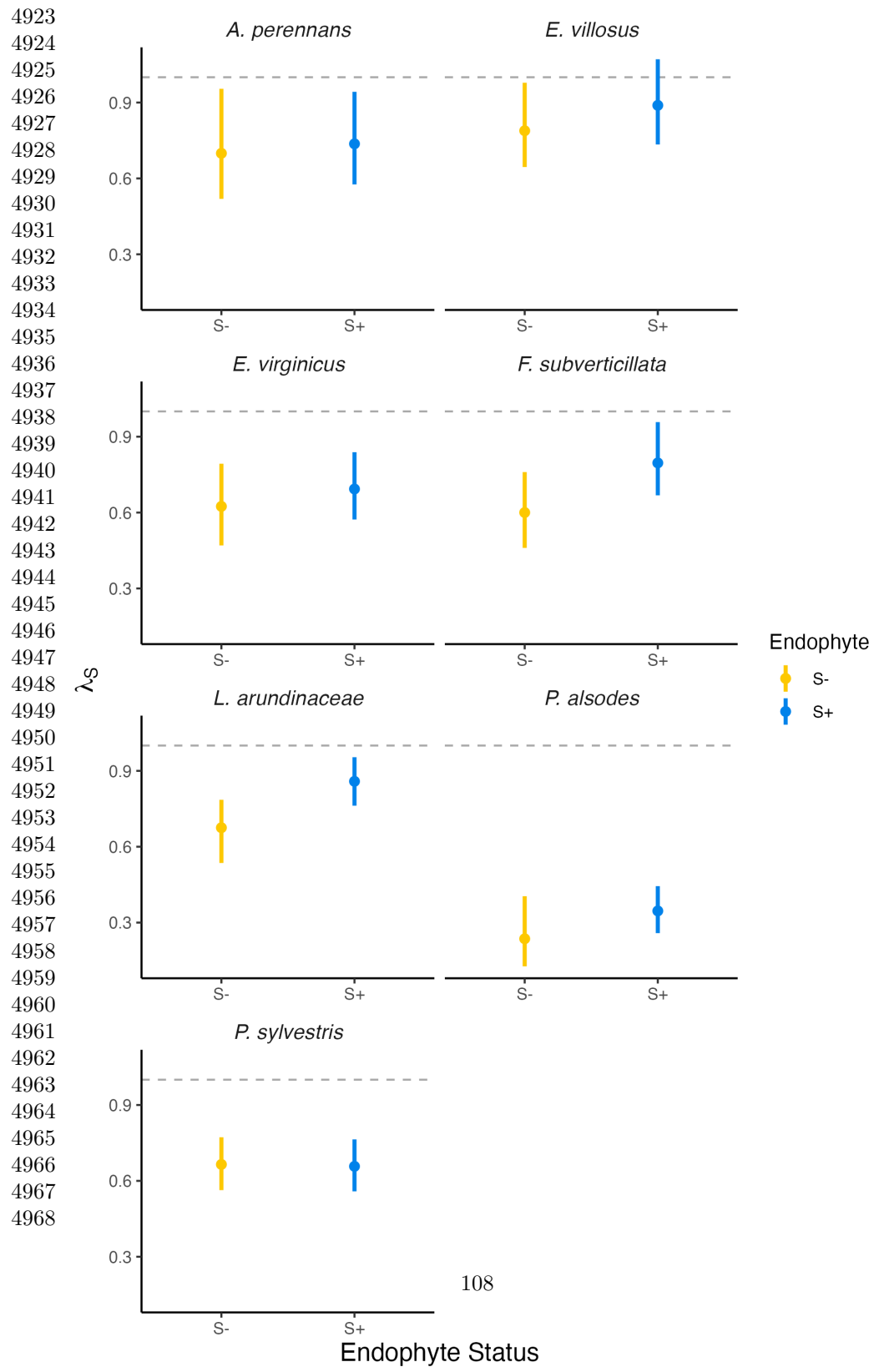
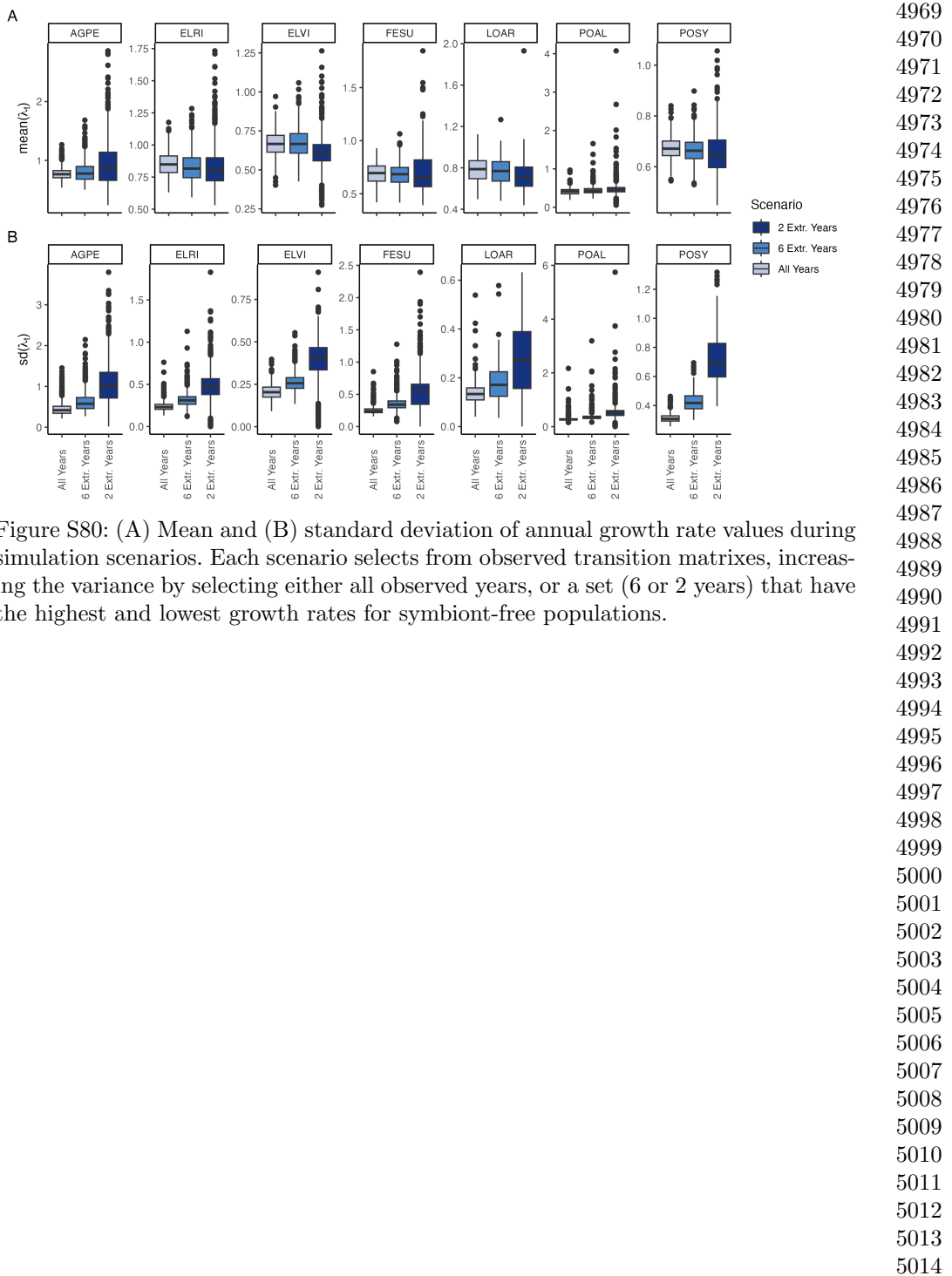
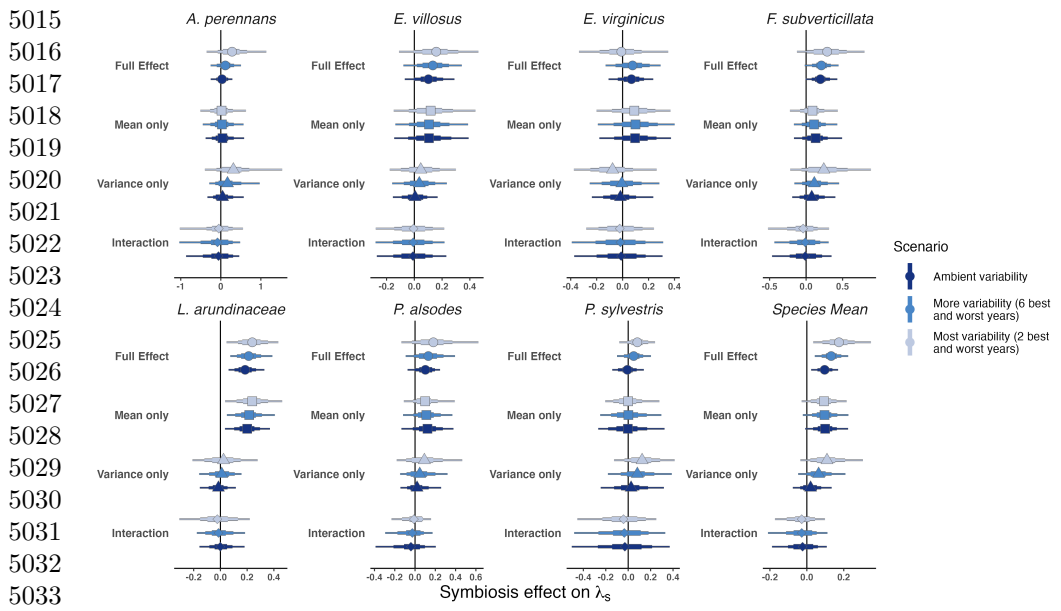


Figure S79: Stochastic population growth rates ( $\lambda_S$ ) for symbiotic (blue) and symbiont-free (yellow) populations. Points show posterior medians along with the 95% credible interval and posterior medians. All values are calculated from matrix models representing recruit plants.





5034 Figure S81: Endophyte contributions to stochastic growth rates under observed and  
 5035 elevated variance across species. The total effect of endophytes (circle) comes from  
 5036 mean benefits (square) and variance buffering (triangle) as well as the interaction  
 5037 between mean and variance effects (diamond). Shapes indicate the posterior mean of  
 5038 each contribution, along with bars for the 50, 75 and 95 % credible intervals. Under  
 5039 scenarios of increasing variance, represented by increasing color intensity, effects of  
 5040 variance buffering increase leading to a more mutualistic symbiosis.

5041  
 5042  
 5043  
 5044  
 5045  
 5046  
 5047  
 5048  
 5049  
 5050  
 5051  
 5052  
 5053  
 5054  
 5055  
 5056  
 5057  
 5058  
 5059  
 5060

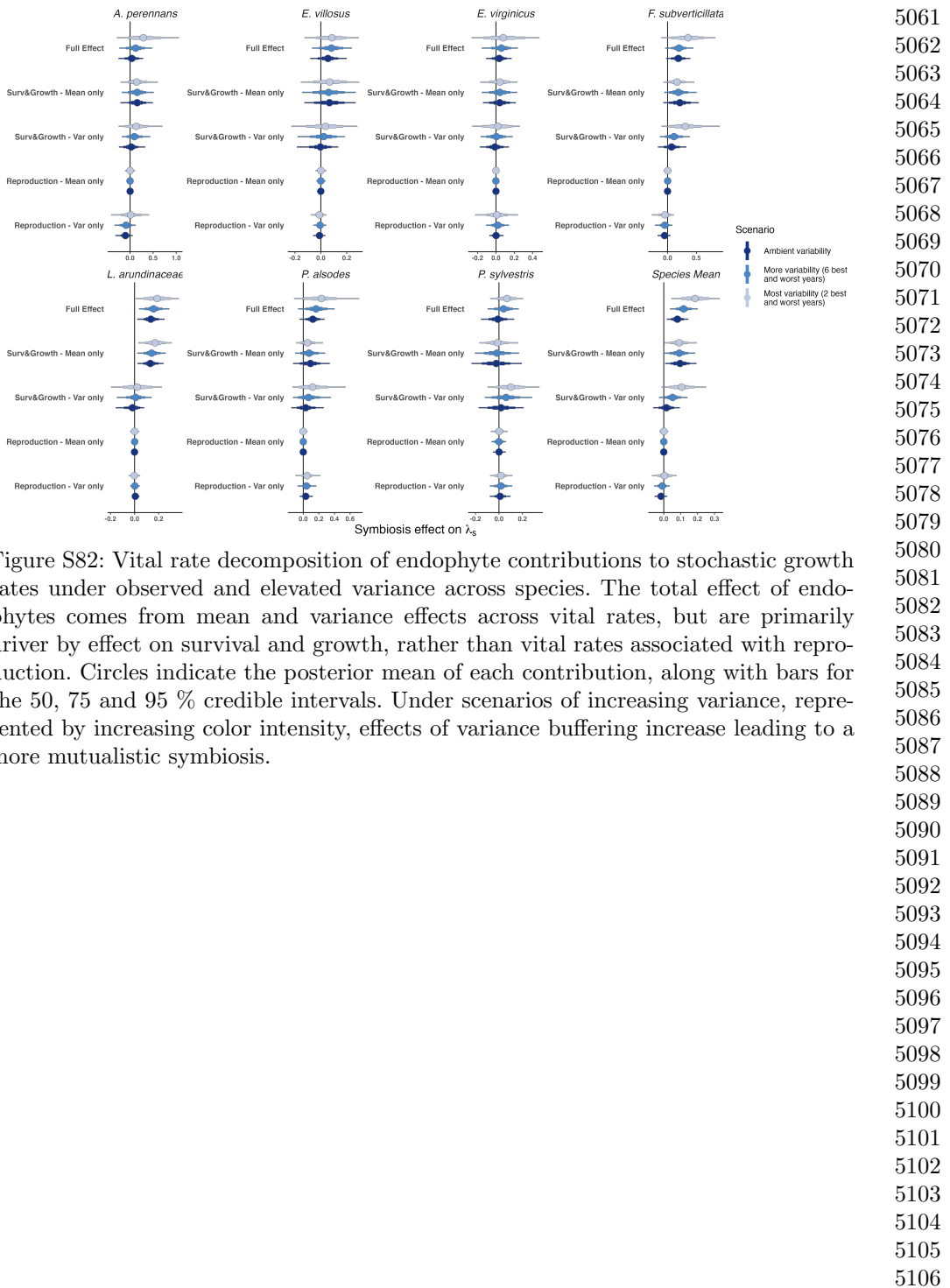
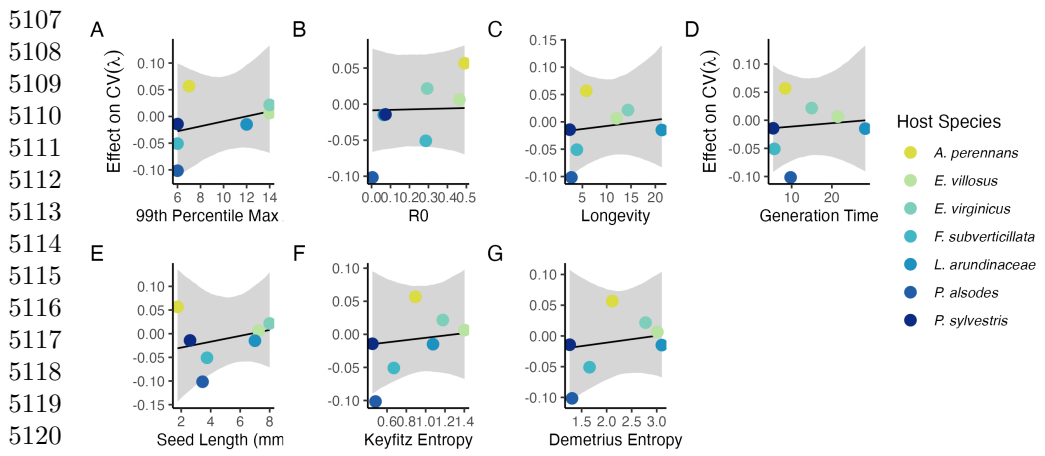


Figure S82: Vital rate decomposition of endophyte contributions to stochastic growth rates under observed and elevated variance across species. The total effect of endophytes comes from mean and variance effects across vital rates, but are primarily driver by effect on survival and growth, rather than vital rates associated with reproduction. Circles indicate the posterior mean of each contribution, along with bars for the 50, 75 and 95 % credible intervals. Under scenarios of increasing variance, represented by increasing color intensity, effects of variance buffering increase leading to a more mutualistic symbiosis.



5121 Figure S83: Relationship between variance buffering and life history traits describing  
 5122 the fast-slow life history continuum accounting for phylogenetic covariance between  
 5123 grass host species. Regressions between life history traits describing the fast-slow life  
 5124 history continuum ((A) 99th percentile maximum age observed during long term cen-  
 5125 suses in years; (B) Net reproductive rate; (C) Longevity; (D) Generation time in years;  
 5126 (E) Seed size) and the effect of endophyte symbiosis on the coefficient of variation in  
 5127 population growth rate ( $\lambda$ ). Each panel shows the fitted mean relationship (line) along  
 5128 with the 95% credible interval.  
 5129

5130  
 5131  
 5132  
 5133  
 5134  
 5135  
 5136  
 5137  
 5138  
 5139  
 5140  
 5141  
 5142  
 5143  
 5144  
 5145  
 5146  
 5147  
 5148  
 5149  
 5150  
 5151  
 5152

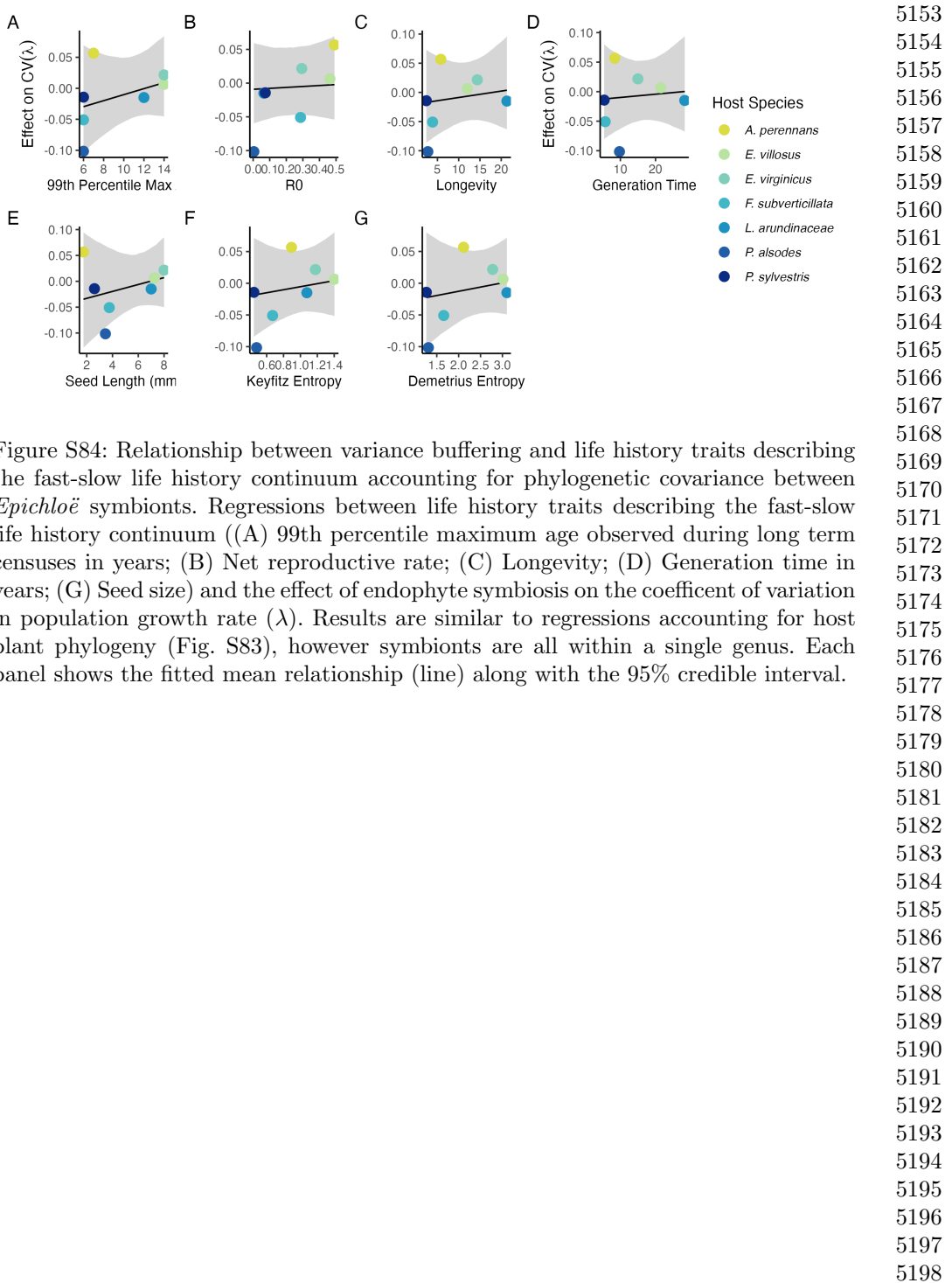
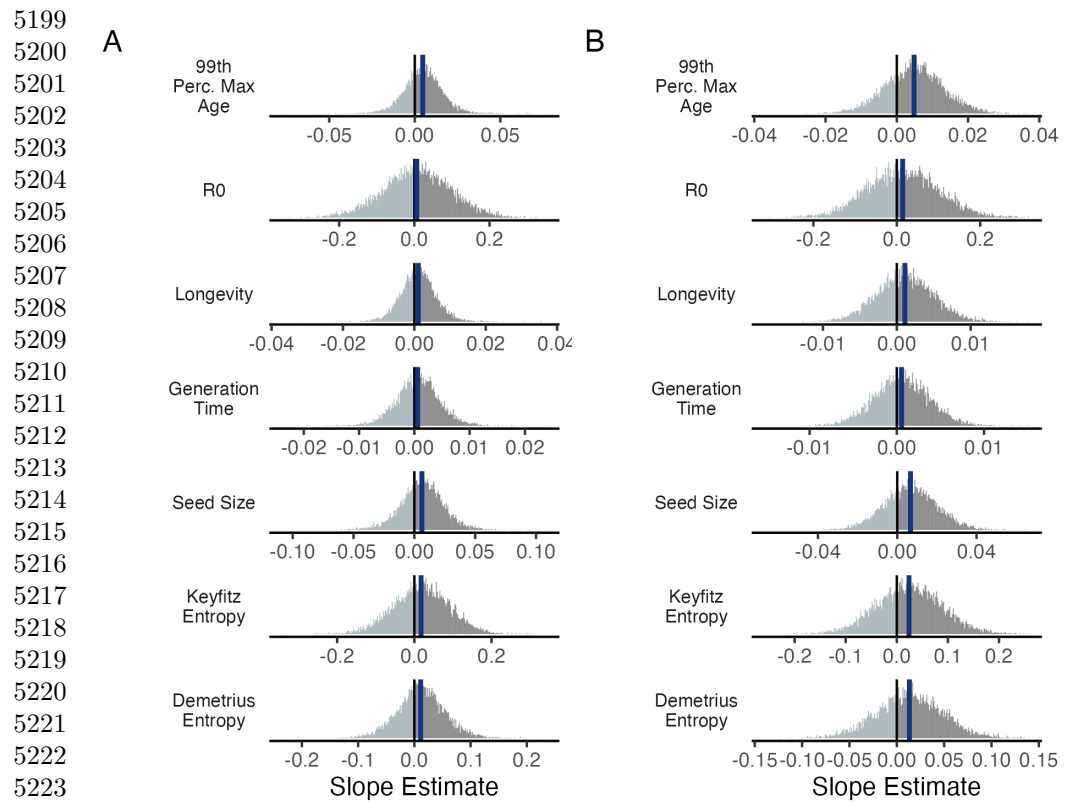


Figure S84: Relationship between variance buffering and life history traits describing the fast-slow life history continuum accounting for phylogenetic covariance between *Epichloë* symbionts. Regressions between life history traits describing the fast-slow life history continuum ((A) 99th percentile maximum age observed during long term censuses in years; (B) Net reproductive rate; (C) Longevity; (D) Generation time in years; (G) Seed size) and the effect of endophyte symbiosis on the coefficient of variation in population growth rate ( $\lambda$ ). Results are similar to regressions accounting for host plant phylogeny (Fig. S83), however symbionts are all within a single genus. Each panel shows the fitted mean relationship (line) along with the 95% credible interval.



5225 Figure S85: Posterior estimates of life history trait effects on variance buffering.  
 5226 Grey histograms show the posterior distribution of the slope parameter from models  
 5227 incorporating (A) host plant phylogenetic covariance and (B) symbiont phylogenetic  
 5228 covariance for each life history trait with blue bars showing the posterior mean.

5229  
 5230  
 5231  
 5232  
 5233  
 5234  
 5235  
 5236  
 5237  
 5238  
 5239  
 5240  
 5241  
 5242  
 5243  
 5244

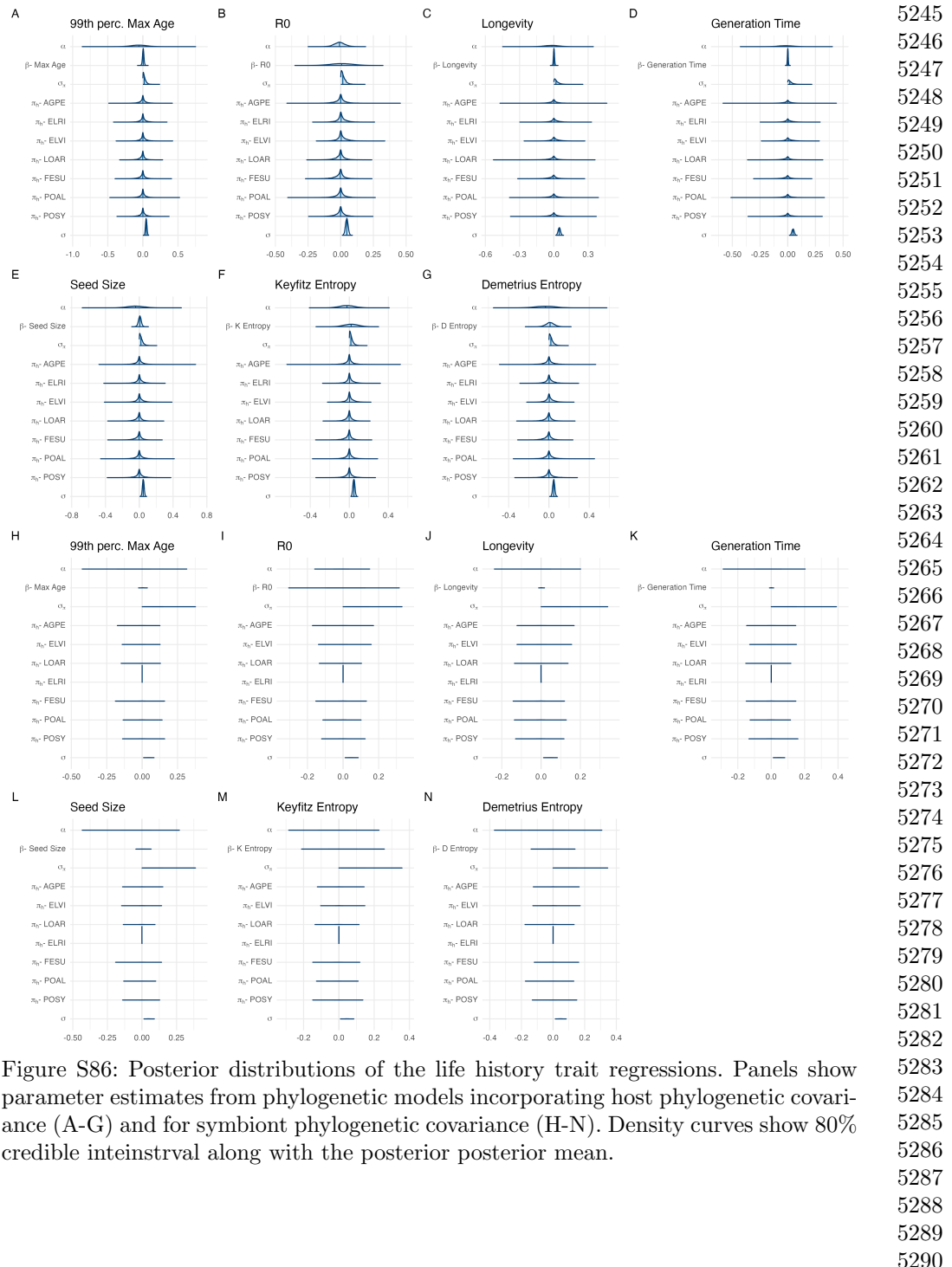
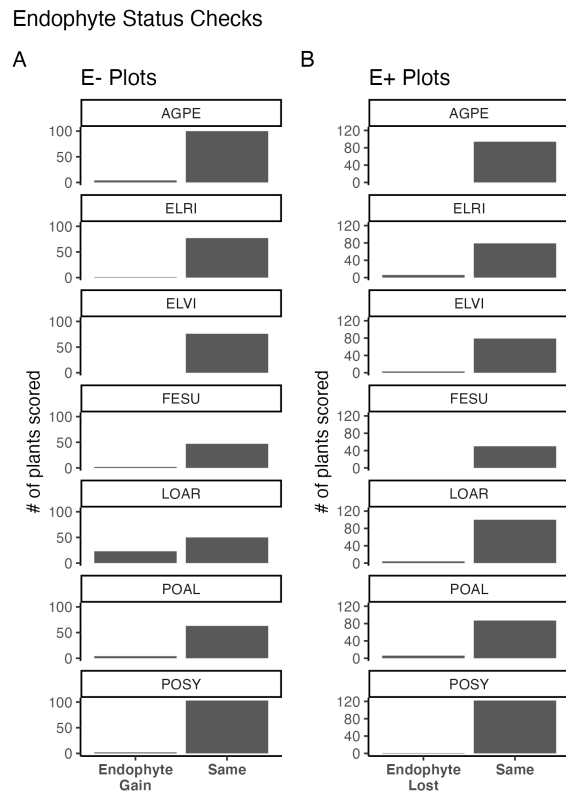


Figure S86: Posterior distributions of the life history trait regressions. Panels show parameter estimates from phylogenetic models incorporating host phylogenetic covariance (A-G) and for symbiont phylogenetic covariance (H-N). Density curves show 80% credible interval along with the posterior mean.

5291  
5292  
5293  
5294  
5295  
5296  
5297  
5298  
5299  
5300  
5301  
5302  
5303  
5304  
5305  
5306  
5307  
5308  
5309  
5310  
5311  
5312  
5313  
5314  
5315  
5316



5317 Figure S87: Faithfulness of experimental plots to assigned endophyte status. Counts  
5318 of plants scored with leaf peels or seed squashes to check the faithfulness of recruits  
5319 to the assigned plot-level endophyte status. (A) Endophytic plants may be gained in  
5320 initially S- plots, or (B) lost in initially S+ plots.

5321  
5322  
5323  
5324  
5325  
5326  
5327  
5328  
5329  
5330  
5331  
5332  
5333  
5334  
5335  
5336

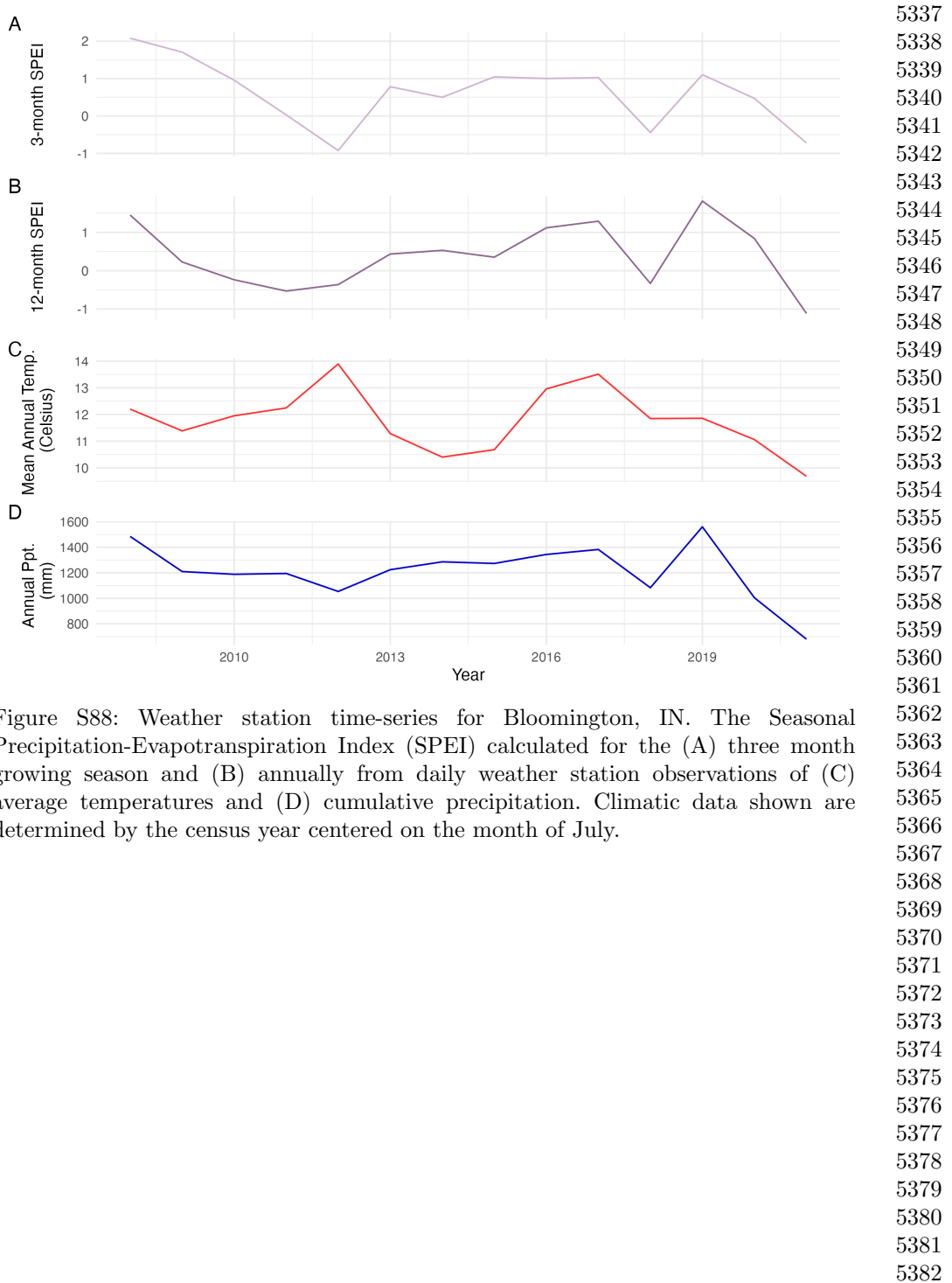
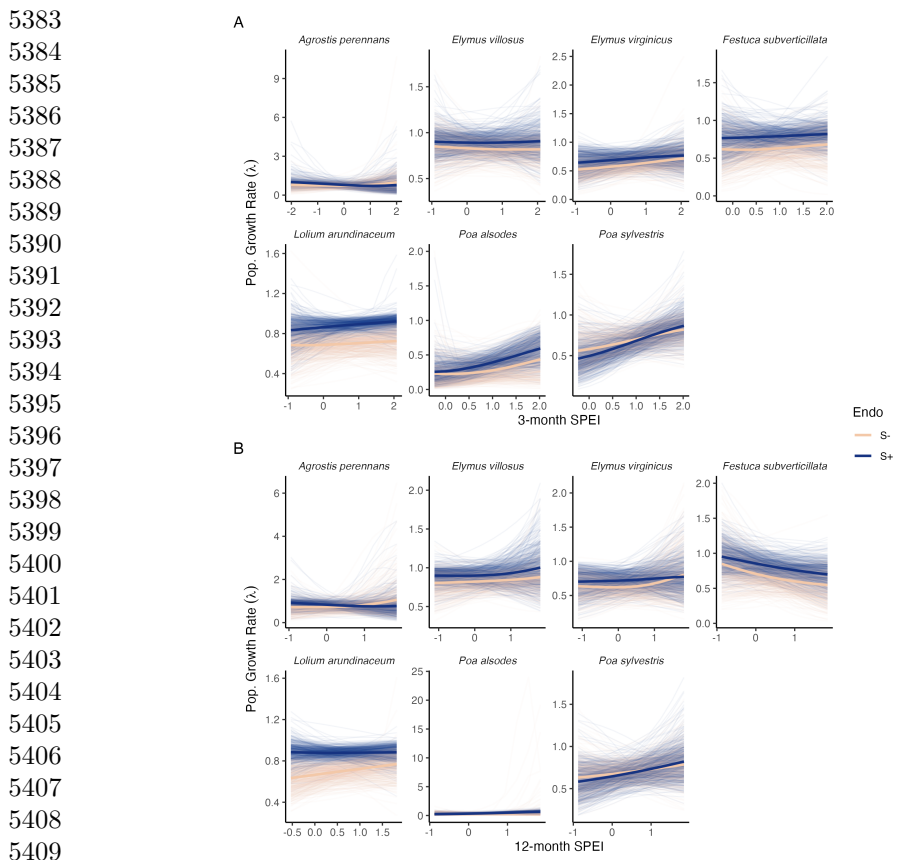


Figure S88: Weather station time-series for Bloomington, IN. The Seasonal Precipitation-Evapotranspiration Index (SPEI) calculated for the (A) three month growing season and (B) annually from daily weather station observations of (C) average temperatures and (D) cumulative precipitation. Climatic data shown are determined by the census year centered on the month of July.



5410 Figure S89: Predicted population growth rates across drought indices. Symbiotic (S+;  
 5411 blue) and symbiont-free (S-; tan) populations respond differently to climate as mea-  
 5412 sured by the (A) 3-month SPEI and (B) 12-month SPEI. Thick lines represent the  
 5413 predicted mean growth rate and thin lines show 500 posterior draws.

5414  
 5415  
 5416  
 5417  
 5418  
 5419  
 5420  
 5421  
 5422  
 5423  
 5424  
 5425  
 5426  
 5427  
 5428

<b>Supplemental Tables S1-S3</b>	
	5429
	5430
	5431
	5432
	5433
	5434
	5435
	5436
	5437
	5438
	5439
	5440
	5441
	5442
	5443
	5444
	5445
	5446
	5447
	5448
	5449
	5450
	5451
	5452
	5453
	5454
	5455
	5456
	5457
	5458
	5459
	5460
	5461
	5462
	5463
	5464
	5465
	5466
	5467
	5468
	5469
	5470
	5471
	5472
	5473
	5474

5475  
 5476  
 5477  
 5478  
 5479  
 5480  
 5481  
 5482  
 5483  
 5484  
 5485  
 5486  
 5487  
 5488  
 5489  
 5490  
 5491  
 5492  
 5493  
 5494  
 5495  
 5496  
 5497  
 5498  
 5499  
 5500  
 5501  
 5502  
 5503  
 5504  
 5505  
 5506  
 5507  
 5508  
 5509  
 5510  
 5511  
 5512  
 5513  
 5514  
 5515  
 5516  
 5517  
 5518  
 5519  
 5520

**Table S1:** Summary of host-endophyte prorogation and transplant methods

Host Species	Symbiont Species	Heat treatment duration (Temp.)	Transplant date
<i>Agrostis perennans</i>	<i>E. amarillans</i>	12 min. hot water bath (60 °C)	April 2008 (10 plots)
<i>Elymus villosus</i>	<i>E. elymi</i>	6 days drying oven (60 °C)	April 2008 (10 plots)
<i>Elymus virginicus</i>	<i>E. elymi</i> or <i>EviTG-1</i>	6 days drying oven (60 °C)	April 2008 (10 plots)
<i>Festuca subverticillata</i>	<i>E. starrii</i>	6 days drying oven (60 °C)	April 2008 (10 plots)
<i>Lolium arundinaceum</i>	<i>E. coenophiala</i>	6 days drying oven (60 °C)	Sept. 2007 (10 plots)
<i>Poa alsodes</i>	<i>E. alsodes</i>	7 days drying oven (60 °C)	Sept. 2007 (8 plots)/April 2008 (10 plots)
<i>Poa sylvestris</i>	<i>E. PsyTG-1</i>	7 days drying oven (60 °C)	Sept. 2007 (8 plots)/April 2008 (10 plots)

Host Species	Observed max age (years)	99th percentile max age (years)	Generation time (years)	$R_0$	Longevity (years)	Seed Length (mm.)	Keyfitz Entropy	Demetrius Entropy	Imperfect transmission rate (%)	Stromata Observed (% of indiv. per species)
<i>Agrostis perennans</i>	11	7	7.6	0.58	6.4	1.75	0.9	2.1	69.8	0.0
<i>Elymus villosus</i>	14	14	20.7	0.35	9.8	7.25	1.3	2.9	100	4.6
<i>Elymus virginicus</i>	14	14	13.4	0.25	12.5	8	1.1	2.6	100	0.6
<i>Festuca subverticillata</i>	9	6	6.6	0.28	4.3	3.75	0.8	1.8	42.7	0.0
<i>Lolium arundinaceum</i>	12*	12*	27.4	0.08	21.3	7	1.1	3.1	100	0.0
<i>Poa alsodes</i>	8	6	9.2	0.003	2.6	3.45	0.5	1.2	99.9	0.0
<i>Poa sylvestris</i>	12	6	8.0	0.14	3.2	2.6	0.7	1.8	16.6	0.1
<b>Page's <math>\lambda</math>-host</b>	—	0.23	0.22	0.19	0.23	0.23	0.19	0.22	—	—
<b>Page's <math>\lambda</math>-host (90% CI)</b>	—	(0-0.8)	(0-0.8)	(0-0.7)	(0-0.8)	(0-0.8)	(0-0.8)	(0-0.8)	—	—
<b>Page's <math>\lambda</math>-symbiont</b>	—	0.57	0.56	0.56	0.56	0.56	0.55	0.58	—	—
<b>Page's <math>\lambda</math>-symbiont (90% CI)</b>	—	(0-0.9)	(0-0.9)	(0-0.9)	(0-0.9)	(0-0.9)	(0-0.9)	(0-0.9)	—	—

\*Censuses for *L. arundinaceum* plots stopped after year 12 of the experiment.

5521  
5522  
5523  
5524  
5525  
5526  
5527  
5528  
5529  
5530  
5531  
5532  
5533  
5534  
5535  
5536  
5537  
5538  
5539  
5540  
5541  
5542  
5543  
5544  
5545  
5546  
5547  
5548  
5549  
5550  
5551  
5552  
5553  
5554  
5555  
5556  
5557  
5558  
5559  
5560  
5561  
5562  
5563  
5564  
5565  
5566

5567  
 5568  
 5569  
 5570  
 5571  
 5572  
 5573  
 5574  
 5575  
 5576  
 5577  
 5578  
 5579  
 5580  
 5581  
 5582  
 5583  
 5584  
 5585  
 5586  
 5587  
 5588  
 5589  
 5590  
 5591  
 5592  
 5593  
 5594  
 5595  
 5596  
 5597  
 5598  
 5599  
 5600  
 5601  
 5602  
 5603  
 5604  
 5605  
 5606  
 5607  
 5608  
 5609  
 5610  
 5611  
 5612

**Table S3:** Summary of host-endophyte drought sensitivities

Host Species	Effect on CV( $\lambda$ )	Effect on Mean( $\lambda$ )	$\frac{\Delta\lambda^-}{\Delta SPEI_3}$	$\frac{\Delta\lambda^+}{\Delta SPEI_3}$	3 month S- to S+ ratio	$\frac{\Delta\lambda^-}{\Delta SPEI_{12}}$	$\frac{\Delta\lambda^+}{\Delta SPEI_{12}}$	12 month S- to S+ ratio
<i>Agrostis perennans</i>	0.0475	0.0513	-0.06	0.05	0.83	-0.05	0.119	2.34
<i>Elymus villosus</i>	0.0105	0.0710	0.00	-0.01	5.89	0.05	0.03	0.74
<i>Elymus virginicus</i>	0.031	0.0913	0.04	0.06	1.56	0.02	0.06	2.41
<i>Festuca subverticillata</i>	-0.1524	0.1386	0.02	0.03	1.15	-0.09	-0.11	1.20
<i>Lolium arundinaceum</i>	-0.0799	0.1872	0.02	0.01	0.47	-0.00	0.05	11.1.
<i>Poa alsodes</i>	-0.6859	0.1079	0.10	0.09	0.62	0.14	0.11	0.79
<i>Poa sylvestris</i>	-0.0164	-0.0211	0.18	0.12	0.64	0.09	0.06	0.64

5613  
5614  
5615  
5616  
5617  
5618  
5619  
5620  
5621  
5622  
5623  
5624  
5625  
5626  
5627  
5628  
5629  
5630  
5631  
5632  
5633  
5634  
5635  
5636  
5637  
5638  
5639  
5640  
5641  
5642  
5643  
5644  
5645  
5646  
5647  
5648  
5649  
5650  
5651  
5652  
5653  
5654  
5655  
5656  
5657  
5658